UNIVERSITY OF OKLAHOMA

GRADUATE COLLEGE

THERMOCATALYTIC AND PLASMONIC CATALYTIC HYDROGENATION REACTIONS FROM FIRST PRINCIPLES

A DISSERTATION

SUBMITTED TO THE GRADUATE FACULTY

in partial fulfillment of the requirements for the

Degree of

DOCTOR OF PHILOSOPHY

By

TONG MOU
Norman, Oklahoma
2020

THERMOCATALYTIC AND PLASMONIC CATALYTIC
HYDROGENATION REACTIONS FROM FIRST PRINCIPLES

A DISSERTATION APPROVED FOR THE
SCHOOL OF CHEMICAL, BIOLOGICAL AND MATERIALS ENGINEERING

BY THE COMMITTEE CONSISTING OF

Dr. Bin Wang, Chair

Dr. Ian R. Sellers

Dr. Daniel E. Resasco

Dr. Liangliang Huang

Dr. Keisha B. Walters

Acknowledgements

First and foremost, I would like to express my sincere and deepest gratitude to my advisor, Professor Bin Wang. My work in this dissertation would not have been possible without his guidance, mentorship, and encouragement. I am grateful for his tremendous support and pivotal role in my research and career development throughout my PhD.

I am very fortunate to have worked with Prof. Daniel Resasco. He introduced me to the world of catalysis and showed me his great passion and patience in conducting research.

I would also like to acknowledge my committee members Prof. Ian Sellers, Prof. Liangliang Huang and Prof. Keisha Walters for their insightful inputs in this dissertation. My sincere thank also goes to Prof. Steven Crossley and Prof. Lance Lobban for their enlightening comments and suggestions during the weekly group meetings.

I have greatly enjoyed and benefited from fruitful collaborations at various research areas with Prof. Pedro Camargo at the University of Helsinki, Prof. Zhaoyang Fan at the Texas Tech University, Prof. Marimuthu Andiappan at the Oklahoma State University, and Prof. Bingjun Xu at the University of Delaware. I would like to acknowledge a group of experimentalists who helped me in different ways bridging experiments with computations, including Dr. Qiaohua Tan, Dr. Daniel Santhanaraj, Dr. Gengnan Li, Dr. Abhishek Gumidyala, Dr. Tuong Bui, Dr. Feifei Yang, Dr. Vincent Whiteside, and Dr. Collin Brown.

It has been a pleasure to share a big office with great people in Dr. Wang's group. I would like to thank past and present group members Dr. Reda Bababrik, Michael, Darius, Steve, Yu, Vy, Issac, and Tien. I wish to thank my friends Jack, Guobing, Zheng,

Xintong, Frank, Redwan, all of whom have left OU at different times, but never cease to send love and cheers along this journey. They made my graduate life at OU memorable and unforgettable.

Special thanks to Prof. Jing Wen, Prof. Jing Su, and Prof. Zhen Yang for their kindness and guidance, especially during the difficult times before my graduation.

Finally, I am extremely grateful to my parents for their tremendous support and unconditional love, for all the sacrifices, for always encouraging me to take on challenges with life and work. I would not have been where I am today without thousands video calls and messages across the Pacific Ocean.

This work was supported by the NASA EPSCoR grant. The research used computational resources at the OU Supercomputing Center for Education & Research (OSCER) at the University of Oklahoma.

This dissertation is dedicated to my parents

献给我的父亲母亲，牟小平，徐捷

Table of Contents

List of Figures

List of Tables

List of Publications

1. De Freitas, I., Parreira, L., Barbosa, E., Novaes, B., **Mou, T.**, Alves, T., Quiroz, J., Wang, Y., Slater, T., Thomas, A., Wang, B., Haigh, S., Camargo, P., Design-controlled synthesis of IrO2 sub-monolayers on Au nanoflowers: marrying plasmonic and electrocatalytic properties. *Nanoscale*, 2020. DOI: 10.1039/d0nr01875a
2. Su, J., **Mou, T.**, Wen, J., Wang, B., Nondestructive functionalization of monolayer black phosphorous using Lewis acids: A first-principles study. *Appl. Surf. Sci.*, 2020, 518, 146210.
3. Su, J., **Mou, T.**, Wen, J., Wang, B., First-principles study on the structure, electronic and optical properties of $Cs_2AgBiBr_{6-x}Cl_x$ mixed-halide double perovskites. *J. Phys. Chem. C*, 2020, 124 (9), 5371-5377.
4. Resasco, J.,[#] Yang, F.,[#] **Mou, T.**, Wang, B., Christopher, P., Resasco, D. E., Hydrodeoxygenation of m-cresol over isolated Pt cations and clusters. *ACS Catal.,* 2020, 10 (1), 595-603.
5. **Mou, T.**, Li, S., Brown, C. R., Whiteside, V. R., Hossain, K., Khalfioui, M., Leroux, M., Sellers, I. R., Wang, B., Role of In in hydrogenation of N-related complexes in GaInNAs. *ACS Appl. Electron. Mater.*, 2019, 1 (4), 461-466.
6. Tirumala, R., Dadgar, A., Mohammadparast, F., Ramakrishnan, S., **Mou, T.**, Wang, B., Andiappan, M., Homogeneous versus heterogeneous catalysis in Cu2O-nanoparticle-catalyzed C–C coupling reactions. *Green Chem.*, 2019, 21 (19), 5284-5290.
7. Quiroz, J., Barbosa, E., Araujo, T., Fiorio, J., Wang, Y., Zou, Y. **Mou, T.**, Alves, T., de Oliveira, D., Wang, B., Haigh, S., Rossi, L., Camargo, P. H. C., Controlling reaction selectivity over hybrid plasmonic nanocatalysts, *Nano Lett.*, 2018, 18 (11), 7289-7297.

8. Barbosa, E., Fiorio, J., **Mou, T.**, Wang, B., Rossi, L., Camargo, P. H. C., Reaction pathway dependence in plasmonic catalysis: hydrogenation as a model molecular transformation. *Chem. Eur. J.*, 2018, 24 (47), 12330-12339.
9. Murphy, B. M., **Mou, T.**, Wang, B., Xu, B., The effect of cofed species on the kinetics of catalytic methyl lactate dehydration on NaY. *ACS Catal.,* 2018, 8 (10), 9066-9078.
10. **Mou, T.**, Wang, B., Rational surface modification of two-dimensional layered black phosphorus: insights from first-principles calculations. *ACS Omega,* 2018, 3 (2), 2445-2451.
11. Ray, K., Yore, A. E., **Mou, T.**, Jha, S., Smithe, K. K. H., Wang, B., Pop, E., Newaz, A. K. M., Photoresponse of natural van der waals heterostructures. *ACS Nano*, 2017, 11 (6), 6024-6030.
12. Li, S., **Mou, T.**, Ren, G., Warzywoda, J., Wei, Z., Wang, B., Fan, Z., Gel based sulfur cathodes with a high sulfur content and large mass loading for high-performance lithium–sulfur batteries. *J. Mater. Chem. A*, 2017, 5 (4), 1650-1657.
13. Li, S., **Mou, T.**, Ren, G., Warzywoda, J., Wang, B., Fan, Z., Confining sulfur species in cathodes of lithium-sulfur batteries: insight into nonpolar and polar matrix surfaces. *ACS Energy Lett.,* 2016*,* 1 (2), 481-489.
14. **Mou, T.**, Quiroz, J., Camargo, P. H. C., Wang, B., Localized orbital excitation drives bond formation in plasmonic catalysis. *(Ready to be submitted)*

List of Presentations

1. “Localized orbital excitation drives bond formation in plasmonic catalysis”. *Laurance Reid Gas Conditioning Conference*, Norman, OK, 2020 poster
2. “Localized orbital excitation drives bond formation in plasmonic catalysis”. *AIChE Meeting*, Orlando, FL, 2019 oral
3. “First-principles modeling of hot-carrier-assisted hydrogenation”. *GPCS Annual Meeting*, Phillips 66 Research Center, Bartlesville, OK, 2019 oral
4. “Role of In in hydrogenation of N-related complexes in GaInNAs”. *OKPVRI Symposium*, Tulsa, OK, 2019 poster
5. “Atomic simulation of nanomaterials for energy applications”. *AIChE Meeting*, Pittsburgh, PA, 2018 oral
6. “Hydrogenation of Indium-related defects in GaInNAs”. *GCoE Grad Student Poster Fair*, Norman, OK, 2018 poster
7. “Computational study of nitrogen-related defects in GaInNAs”. *OKPVRI Symposium*, Stillwater, OK, 2018 oral
8. “Rational design of the cathode materials in the lithium-sulfur batteries”. *AIChE Meeting*, Minneapolis, MN, 2017 oral
9. “Rational design of the cathode materials in the lithium-sulfur batteries”. *ACS Pentasectional Regional Meeting*, Lawton, OK, 2017 oral
10. “DFT study of chemical functionalization of two-dimensional materials”. *76th Annual Physical Electronic Conference (PEC)*, Fayetteville, AR, 2016 oral
11. “DFT study of chemical functionalization of two-dimensional materials”. *ACS Pentasectional Regional Meeting*, Bartlesville, OK, 2016 oral

Abstract

As the world is facing post-climate change situation and the escalating demand of energy, a gradual energy transition from fossil fuels (oil, coal, natural gas) to renewable energy technologies (natural resources such as biomass, solar, wind) is inevitable and essential. Solar energy, as the most abundant, safe and clean energy source among all available renewable energy technologies, has prospective potentials as future power generators. However, although significant progress has been made, the electricity generation from sunlight in commercial photovoltaic (PV) solar cells still suffer from low energy conversion efficiency and high cost. In addition, due to technological difficulties associated with the rapid electron-hole recombination in photocatalysis systems, realizing commercial implementations of photocatalytic systems remains a challenge.

In this dissertation, a thorough first-principles analysis was performed on three hydrogen-involving processes, including solar to electricity, catalytic hydrotreating and solar to chemical conversion processes. By investigating their thermodynamic and kinetics properties, we aim to bridge solar energy utilization with chemical energy production under ambient conditions.

We begin with the discussion of nitrogen-related defects in a dilute nitride material GaInNAs, which shows promising candidacy as the fourth junction in multijunction solar cells. While the photoluminescence spectra presented remaining defects in the hydrogenated alloy, first-principles calculations revealed the thermodynamic limitation of hydrogen addition on the In-N complexes. Next, a comprehensive kinetic study on cyclohexene hydrogenation reaction on palladium and palladium hydride surfaces were conducted, through a combination of experimental and

theoretical work, which laid foundations for later study of plasmonic hydrogenation reactions. In light of thermodynamic and kinetic studies addressed earlier, we undertake investigations on plasmonic catalytic hydrogenation of 4-nitrophenol on gold surfaces. We measured the catalytic activity with and without light irradiation and observed higher reaction rates under light. A theoretical correlation between rate enhancements and reaction energy barrier reduction was constructed via density functional theory calculations. Moreover, we propose that the reaction can be further enhanced over a hexagonal boron nitride (*h*-BN) layer supported on Au in an Au@*h*-BN core-shell structure. In this dissertation, we attempt to understand the electron behavior at atomic level, through the investigation of hydrogen-involved processes. Moreover, by discussing efficiency improvement options, we attempt to guide the future design of plasmonic catalysts.

Chapter 1. Introduction

1.1 Metal Catalysts in Heterogeneous Catalysis

Catalysis plays a pivotal role in human lives, as it is the heart of chemical technologies in the industrialized world. Heterogeneous catalysis,[1] compared to homogeneous catalysis and enzyme catalysis, having catalysts in different phases from reactant molecules, provides a relatively easier process for subsequent product separation and catalyst recovery.[2] The applications of heterogenous catalysis on metal catalysts can be found in numerous large-scale industrial catalytic processes,[3, 4] including but not limited to the production of fertilizers,[5] pharmaceuticals,[6] hydrocarbon refining,[7] treatment of automotive exhausts,[8] and fuel cells.[9] With the growing research efforts on nano-size metal species, the group has been subdivided into three types based on particle size: single atoms, nanoclusters, and nanoparticles. Singly dispersed catalysts are typically on the size of 0.1 nm with discrete atomic orbitals.[10, 11] It consists of a metal atom supported on metal oxides or zeolites framework, showing similar characteristics as homogeneous catalysts, but different from homogeneous catalysts, the confinement effects of metal oxides and zeolites retain single atoms in a stable form. Importantly, single-atom-supported catalysts offer 100% efficient metal utilization and high selectivity. On the other hand, subnanometric metal clusters, having atomicity equal or fewer than 40 atoms, exhibit discrete HOMO (highest occupied molecular orbital) and LUMO (lowest unoccupied molecular orbital) molecular orbitals that are accessible by substrate molecular orbitals. From a geometric point of view, metal atoms in a cluster can have different local chemical environments, and even clusters with the same number of atoms may have distinct structures, and subsequently, different molecular adsorption

conformations and catalytic performances. When the atomicity exceeds 40, electronic orbitals start to overlap with each other and form a continuous energy level, implying a nonmetallic to metallic transition.[12]

Late transition metal nanoparticles show excellent activities, selectivities, and stabilities in a variety of catalytic reactions,[13] such as selective hydrogenation of alkynes and olefins,[14] CO oxidation in pollution control,[15] water-gas shift reaction,[16] Fischer-Tropsch synthesis,[17] ammonia synthesis,[18] etc. The catalytic performances are strongly influenced by the geometric configurations of exposed surface atoms (facet, edge, corner, metal-support interfaces) of nanoparticles, as well as electronic properties that are associated with metal d-band center.[19, 20] The d-band theory was proposed by Noskorv regarding the oxygen reduction reaction activity on the platinum surface, primarily on the relationships between oxygen atom binding strength and platinum d band center. This theory is based on the hybridization between localized d orbitals in transition metals and s or p orbitals in substrate molecules that generates bonding and anti-bonding orbitals.[21] The increasing filling of anti-bonding states demonstrate a weaker bond, while a decreasing filling means a stronger bond. Furthermore, reactivity trend of transition metals in terms of the binding energy of intermediates follows the well-known Sabatier-principle-based "volcano shaped relationship",[22] that is, the interactions between the catalyst and surface intermediates should be just right for them to propagate/desorb.[23]

Among late transition metals, platinum-group metals (Group 10 elements Ni, Pd, Pt) are highly active for hydrogenation reactions,[24, 25] which is one of the most important type of reactions in industrial areas, including the hydrogenation of C=C, C≡C functional groups and polar groups like -NO_2 and C=O.[26-29] For most hydrogenation

reactions on metal surface, H_2 dissociation is considered a key step. It is known that H-H bond breaking on PGM surfaces is exothermic and has negligible energy barrier.[30] For example, hydrogen molecule dissociation to two adsorbed hydrogen atoms on Pd is facile, as proposed by Horiuti and Polanyi in 1893,[31] the subsequent hydrogenation steps proceed via sequential single hydrogen atom addition. Notebly, when the catalyst is highly active for hydrogenation, the selectivity towards semihydrogenated product can be low, since overhydrogenation to completely hydrogenated molecules is inevitable. Examples can be found in the reduction of acrolein,[32] crotonaldehyde, 1,3-butadiene, phenylacetylene, and ethene, where products such as unsaturated alcohols and partially hydrogenated hydrocarbons are desirable and invaluable as building blocks in chemical industry. On the other hand, in more complex reaction systems, namely, furfural hydrogenation or the reduction of nitroarene with different functional groups, the selectivity can be influenced by different operating conditions. On the contrary to PGM surfaces, H_2 dissociation on Group 11 metals (Cu, Ag, Au) catalysts are highly unfavorable with a high activation barrier.[33, 34] For example, a previous study by Sykes[35] has demonstrated that H_2 adsorption on close-packed Au (111) surface has a large activation energy of 1.04 eV, and the adsorption energy of dissociated H (per H atom) on fcc hollow site is positive as 0.14 eV (positive adsorption energy means the substrate does not favor adsorption). Conversely, similar calculations on Pd (111) surface showed a barrierless process with adsorption energy per H atom being -0.58 eV. Regarding H_2 uptake on Pt surface, the microcalorimetric experiments established by Dumesic showed that the adsorption of H over Pt powders is -45 kJ/mol.[36] In a separate study, the authors identified hydrogen molecule adsorption on Cu (111) being endothermic (0.16 eV) and is

hindered by a large barrier of 0.83 eV.[37] Also, temperature-programmed desorption (TPD) experiments of H_2 dissociation on Cu (111) under ultrahigh vacuum condition (UHV) required 0.4 eV molecular beam to dissociate H_2.

This section of Chapter 1 discusses a number of mechanistic studies in the literatures on hydrogenation catalysis on supported Pd, Pt and Au and bimetallic nanoparticles. One thing to notice is that the reactions that take place on support or metal-support interfaces are beyond the scope of the discussion here. This section mainly focuses on the nature of these metal catalysts to provide insights into the reaction mechanisms.

1.1.1 Palladium Nanoparticle

As mentioned in the introduction of Section 2, Pd surface facilitates the dissociation of molecular hydrogen. In hydrogenation catalysis, not only the dissociation of H_2 is the essential factor that contributes to the overall hydrogenation activity, the surface diffusion of hydrogen also determines its activity to participate in the reaction. Hutchings and coauthors[38] studied systemically the adsorption and diffusion at various sites on the (111) surfaces of three metals, Pd, Pt, and Ni. Their density functional theory calculations showed that hydrogen atom diffuses with 13 kJ/mol barrier on Pd and Ni, whereas the diffusion barrier on Pt is 2-3 kJ/mol since there are no significant bonding differences when H adorbs on different Pt sites.

Pd catalysts have superior activity for the hydrogenation of acetylenes and olefins. Efforts have been made on the structure of supported Pd catalysts for even better performance. For instance, it was reported that cyclohexene hydrogenation to

cyclohexane exhibits excellent activity on multipods Pd nanocrystals.[35, 39] Another study compared acetylene hydrogenation on Pd nanoparticles of different shapes,[40] while the selectivity towards ethylene remains high (~65%) among all the catalyst shapes, the authors found octahedral particles possess the greatest activity due to exposed (111) surfaces that adsorb acetylene less strongly for it to propagate than low index facet (100).

Commercially, Pd catalysts are used as catalysts to remove trace amounts of acetylene/phenylacetylene from crude ethylene/styrene feedstocks to avoid poisoning the downstream Ziegler-Natta catalyst for large-scale production of polymers and copolymers.[41] As mentioned earlier, high reactivity of Pd catalysts can lead to serious overhydrogenation to ethane/ethylbenzene, and these hydrocarbons can coke the catalyst and decrease the catalyst lifetime. Therefore, to reach higher selectivity towards semihydrogenated hydrocarbons, a second metal atom has been introduced as a promotor to fine tune the catalyst's properties, namely, Ag,[42, 43] Au, and In,[44] Ni,[45] Cu,[46] and Pb.[47] For instance, Pd L3 X-ray near-edge absorption peaks indicated charge transfer of d electrons from Ag to Pd when Ag was added as a promoter, resulting in weaker adsorption of ethylene,[48] so it can desorb prior to complete hydrogenation. In addition, first-principles calculations conducted by Neurock elucidated weaker adsorption of ethylene over ordered PdAg surfaces compared to its pure counterpart.[49] The authors attributed the change in adsorption strength to two effects: geometric and electronic effects; they found the intermediates tend to change their adsorption sites to avoid direct interaction with Ag atoms, and the computed d band center of surface Pd atoms shifts further away from the fermi level with more Ag added, consistent with the previously mentioned XANES study.

It is well known that high H_2 pressures causes surface reconstruction of a Pd lattice, in which bulk Pd absorbs hydrogen and forms hydride phases. Palladium hydrides not only show potential technological application in hydrogen storage in fuel cells,[50] but are of particular scientific interest to researchers in catalysis community due to their distinct performance compared to pure palladium. Figure 1. 1 plots the absorption relationship in the palladium-hydrogen system in terms of H/Pd atomic ratio as a function of temperature and pressure. Each isotherm curve represents phase transition from pure α- to β-hydride phase of palladium. Temperature programmed desorption experiments and H-D exchange reactions are common tools to detect subsurface hydrogen in palladium. In temperature programmed desorption plots, there are two distinct signals. One with a sharp low-temperature signal indicating the desorption of surface hydrogen, followed by a broad desorption between 500 and 600 K, indicating H atoms that have passed through the bulk to the surface. In the H-D exchange reactions an order of magnitude more HD evolves from the surface than can be chemisorbed on the outer layer, hence indicating that most of the H_2 or D_2 is absorbed rather than adsorbed. α-Hydride phase of Pd shows a negligible promotion effect on selective hydrogenation. Neurock and coworkers examined elementary steps of this reaction over both Pd and α-hydride phase of Pd using periodic DFT calculations. In spite of weaker adsorption of acetylene and intermediates on the hydride phase, the change in activation energy and overall reaction energy is trivial.[51] Additionally, their computed barrier for subsurface H diffusion to Pd surface is similar to the barrier of hydrogenation reactions, indicating subsurface H may diffuse to the surface under real catalytic conditions. On the other hand, β-hydride phases of Pd promote complete hydrogenation.[52] Therefore, in order to

avoid the formation of hydride, alloying Ag with Pd was found to prevent H absorption to bulk Pd, thus enhancing the hydrogenation selectivity.[44, 53] Chapter 5 presents detailed first-principles DFT calculations of cyclohexene hydrogenation to cyclohexane over Pd and PdH surfaces, together with experimental kinetics study, provide a comprehensive mechanistic study of surface reaction.

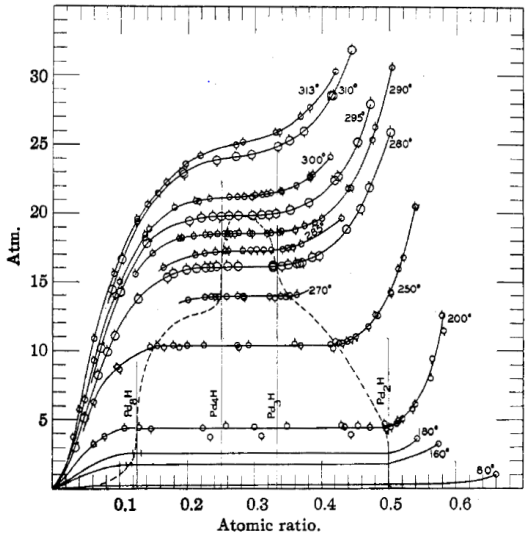

Figure 1. 1 Pressure-concentration diagram of palladium hydrogen system. (Reproduced from reference[54])

1.1.2 Platinum Nanoparticle

While palladium catalyst is very selective to ethylenic bond, platinum is capable of promoting the hydrogenation of polar functional groups at relatively mild conditions. For instance, furfural conversion achieved 96% selectivity to furfuryl alcohol at 58% conversion, 423 K and 2 bar hydrogen pressure on Pd/C.[55] The selectivity of cinnamyl alcohol reached 81.5% by hydrogenating cinnamaldehyde at 298 K, 11 bar hydrogen pressure over a commercial Pt/graphite catalyst.[56] Theoretically, Loffreda and coauthors

compared reactions pathways of acrolein conversion to propanal and propenol on Pt (111) catalyst.[57] Their calculations showed lower activation energies towards unsaturated alcohol (C=O hydrogenation) but its desorption limits the reaction towards propenol. Contrary to Pt, hydrogenating polar functional groups on Pd generally happens at more rigorous conditions (higher temperature and pressure). It is interesting to compare the hydrogenation chemistry these two catalysts possess since they belong to the same group in the periodic table. Electronically, d-orbital in Pd is filled however Pt has a partially filled d-orbital (Electron configuration: Pd [Kr] $4d^{10}$; Pt [Xe] $4f^{14}$ $5d^{9}$ $6s^{1}$). A report consisting of experimental and theoretical work on MgO supported Pt nanoparticles showed higher activity of ethylene hydrogenation to ethane than on supported Pd nanoparticles. The reason for higher activity on Pt than on Pd was stated to be the lower d band center of Pt nanoparticles (ε_c^{Pt}= -2.40 eV, ε_c^{Pd}= -1.86 eV).[24] In a separate effort, the authors stated that the selectivity to hydrogenate ethylenic bond on Pd originates from the smaller d band width of Pd than Pt that induces more repulsion between metals with large d bandwidth and C=C group.[58] The universal relation between the two catalysts on different reactions requires further investigation and debate.

Comparing to palladium, H solubility in platinum is very low at ambient pressure so that platinum does not form hydrides at ambient conditions. In literature, platinum hydride was synthesized under at a pressure of 27 GPa at 300 K in synchrotron x-ray diffraction experiment.[59]

1.1.3 Gold Nanoparticle

Gold is usually recognized a poorly active catalyst due to its completely filled d-orbital (Electron configuration: Au [Xe] $4f^{14}$ $5d^{10}$ $6s^{1}$). There are no valence electrons at the outer shell eager to make bonds with substrate molecules. A theoretical paper in 1995 explained the two reasons gold as the least active metal among all metals.[60] Regardless, there has been significant advances in recent decades in realizing catalytic performance of gold-based materials.[61] Although the selectivity towards desired products can be high on classical gold catalysts (Au has larger d band width than Pt or Pd that induces repulsion between C=C and Au surface), activity remains too low for potential industrial applications compared to traditional PGM metals.[62] Higher catalytic activity on gold-based catalyst is generally achieved in two ways: (1) when the reaction happens on gold nanoparticles with defect sites, e.g. edges, corners; (2) when the reaction takes place at the perimeter interface between gold nanoparticles and the support. H diffusion energetics on Au (111) surface was studied by Mullins and coauthors. This study demonstrated that H favors adsorption on the fcc hollow site and the migration from fcc to hcp, hcp to top site for participating in reactions has an energy barrier within 0.30 eV, indicative of a facile process.[63] A nice review from the same group suggested that a single H atom is likely one of the more active species on gold surfaces since it is very weakly bound. They thus proposed that as long as hydrogen atoms are supplied to the surface (in different ways), they can greatly contribute to reactions on gold surfacesa.[64] Study in Chapter 6 presents hydrogenation of nitro-unsaturated molecule on the (111) facet of the gold nanoparticle, where surface-bound H atoms come from $NaBH_4$ dissociation in the solution.

Clean gold particles (without support) is historically considered catalytically inert. However, gold nanoparticles have been acknowledged as superior visible-light absorbers under low-intensity light illumination to generate intense surface plasmons. Silver, and some earth abundant metals such as copper and aluminum exhibit similar optical behavior under resonance conditions. Chapter 6 demonstrates catalytic behavior of gold nanoparticle in the manner that it serves as both light absorber and catalyst in plasmonic catalysis.

1.2 Plasmonic Catalysis

Commercial heterogeneous catalysis utilizes thermal energy to drive a chemical transformation; however, as we are facing severe weather conditions associated with the use of fossil fuels, solar energy has received significant attention in recent years as a promising nonrenewable energy source. Photocatalysis, along with photovoltaic-generated electricity in electrocatalysis become the center of scientific research nowadays, providing more inputs in addition to thermal energy to produce fuels and chemicals.

Conventionally, thermal energy is supplied to activate a rate-limiting step in a chemical reaction; however, increasing reaction temperature triggers every available reaction coordinate in the system, therefore enhances simultaneously desired and competing undesired elementary steps and reduces selectivity to desired products. In addition, high operating temperature greatly affects thermal stability of catalyst and reduces catalyst lifetime. Plasmonic catalysis, in principle, opens an avenue to a low-temperature, highly selective and environmentally benign process to accelerate and

control chemical transformations.[65, 66] Because of this unique potential, plasmonic catalysis has received extensive attention in recent years.[67-69]

Unlike traditional photocatalysts made of semiconductors, metal nanoparticles like Ag, Au, Cu can serve as light absorbers without the involvement of semiconductor materials. In plasmonic catalysis, plasmons are collective oscillations produced from the couplings between the metal valence electrons and the incident photons through the excitation of localized surface plasmon resonances (LSPRs) in the metal nanoparticles (NPs) upon visible-light absorption, as long as the size of the metal nanoparticles is equal or smaller than the light wavelength. The small imaginary dielectric function of these noble metals (Ag, Au, Cu) brings large optical extinction cross-section of a nanoparticle at LSPR frequencies.[70, 71] Their relationship follows the Mie approximation (sphere nanoparticles) below:

$$\sigma_{ext} \sim \frac{\varepsilon_2}{[\varepsilon_1 + 2\varepsilon_m]^2 + \varepsilon_2^2}$$

Where ε_1 and ε_2 are the real and imaginary dielectric function of the metal, respectively, ε_m is the dielectric constant of the medium (usually air).

A few mechanisms have been proposed in the literature related to the nature of charge transfer across the interface between plasmonic materials and their local environment after plasmon-mediated electronic excitation. For example, excited surface plasmons may decay non-radiatively upon photon absorption to form highly energetic electrons and holes,[72] forming hot Fermi-Dirac distribution;[73] these so-called "hot" carriers, while having enough energy, can be transferred to the adjacent substrate molecules[74-78] or semiconductors.[79, 80] This hot-carrier-driven process has been used to explain the catalytic enhancements of various photodissociation reactions, such as N_2

dissociation,[81, 82] H_2 dissociation,[75, 83] NH_3 decomposition,[84] and nitrite reduction.[85-87] This mechanism does not allow targeted charge transfer to specific molecular orbitals in the adsorbate. Alternatively, in plasmonic metal NPs, direct charge excitation to the interfacial electronic states through chemical interface damping (CID) is possible within the metal-adsorbate complex such as in methylene blue desorption on Ag NPs.[67] This direct charge transfer, which does not necessarily go through the charge carrier excitation process, can be manipulated by changing the photon energy, and controlling the size, shape and composition[88, 89]of the metal NPs and lead to targeted occupation of specific molecular orbitals towards desired selectivity by breaking or forming a chemical bond. Indeed, many previous works have shown that electron-induced plasmonic catalysis can influence reaction selectivity.[86, 90, 91]

Despite the significant progress in light-induced rate enhancements, the efficiency of plasmon-mediated photocatalytic process is still much lower than that on traditional semiconductor-based photocatalysts. There are two factors that might be responsible for the low efficiency: short lifetime of hot electrons (fast recombination rate in femtosecond range[92]); hot electrons with energy lower than required energy to populate the desired molecular orbital are wasted in the form of phonons (heat). Furthermore, previous reported experimental or theoretical studies have been focused on bond dissociation events; it is not clear if these direct and indirect energy transfer can also assist bond formation events, such as hydrogenation reactions. In many practical industrial chemical processes, such as hydrotreating in refineries and ammonia synthesis, bond association is a key elementary step. Finally, orbital hybridization between the plasmonic metal and the adsorbate frontier orbitals significantly broaden the latter,

making it very challenging for selective energy transfer to targeted orbitals for specific bond formation and breaking, which limits the overall photon-to-chemical conversion efficiency and reaction selectivity.

Here in Chapter 6, we present experimental and theoretical investigation on the visible-light-driven reduction of a nitroaromatic molecule on a gold surface, through which we show that plasmon excitation can stimulate bond formation in a hydrogenation reaction and that this effect can be further enhanced if the excited electrons can be localized at the molecular orbital that is electronically decoupled from the plasmonic metal. This work aims to provide new insights on the plasmonic bond formation and a valuable strategy to accelerate chemical reactions.

1.3 Light Absorbing Materials

Despite noble metals in nanoscale exhibit superior optical properties under visible light irradiation, traditional semiconductor materials such as silicon, germanium, gallium arsenide can absorb light and are widely used in laser diodes, microwave-frequency integrated circuits, and solar cells, among others.

Solar cells are promising technologies that convert sunlight to electrical current without external heat supply.[93-97] The technology is based on photovoltaic effect, which was discovered by Alexandre-Edmond Becquerel in 1893 in which he created electrical current by shining light on an electrode in a conductive solution. This finding, also known as the “Becquerel effect”, is a phenomenon when light in the form of photons strike a light absorbing material, generates electron (negatively charged carrier)-hole (positively charged carrier) pairs with exact energy provided by photons upon absorption,

resulting in the flow of energy carriers (current) and subsequently a built-in potential barrier (voltage) across the cell.

Current state-of-the-art solar cells can be found in applications in consumer goods, home lighting,[98] space and satellites,[99] desalination plants,[100, 101] and water pumping systems.[102-104] However, solar-powered PV technologies are barely replacing conventional fossil fuel power plants at this stage due to two major setbacks: high cost and less efficiency. Therefore, more efforts have been made to seek developments in the device fabrication (reduce cost, reduce scarce materials like In/Ga), the discovery of new materials, and methods to increase the overall cell efficiency.

Solar absorber materials play a central role in the fabrications of solar cells. To date, various types of materials were employed in the production of PV solar cells, ranging from different forms of silicon (single crystal,[105, 106] multi-crystalline,[107] amorphous), III-V compounds (gallium arsenide,[108] indium phosphide) to organic materials (dyes,[109] polymers[110, 111]) to perovskite.[112] Silicon was the first-generation material used in solar cells, owing to its abundance and low toxicity. However, major setbacks of silicon solar cells are high manufacturing cost from using pure silicon in the manufacturing process and low optical absorption coefficients since silicon has an indirect band gaps. The light-to-electrical efficiency of single junction Si solar cell with a band gap E_g = 1.1 eV has an upper limit calculated to be 30%,[113] due to fundamental spectra loss. Compared to the conventional silicon wafer solar cells, multijunction cells made from III-V compounds[114] have gained significant attention in the space power generation since 1950 due to their great radiation resistances,[115] improved power/weight ratios as well as higher total conversion efficiency[116] because they can convert a wider

range of the light spectrum to electricity. The standard III-V triple-junction cell design is shown in Figure 1. 1, which consists of GaInP (E_g = 1.9 eV), GaInAs (E_g = 1.40 eV) layers on a Ge (E_g = 0.67 eV) substrate grown monolithically on top of one another. Each layer has a specific band gap value that is designed to match a specific region on the solar spectrum. Photons that are not absorbed by one cell must be available to the next cell (sub-cells have decreasing band gap values from top to substrate). Introducing a fourth junction to the triple-junction cell is a promising design approach for creating a narrower wavelength window to capture a large range of photon energies,[117] for this purpose GaInNAs (E_g = 1 eV) is most commonly added, immediately above the Ge, since it has a correct band gap value as well as a matching lattice constant. However, the disadvantage of adding GaInNAs in the cell is the substitutional and interstitial N impurities present in the crystal lattice that narrow the optical band gap and greatly reduces device efficiency. The illustration of localized states in the band structure of a host substrate can be found in Figure 1. 2, where impurities act as donors/acceptors in semiconductor materials. It has been reported in the previous theoretical and experimental works that hydrogenation is important to passivate Ga-N bonding-induced defects; however, detailed understanding of other forms of defects is still lacking. Here in Chapter 3 first-principles calculations are employed to model potential N impurities at atomic level, along with the thermodynamic behavior of hydrogenation in the crystal lattice. The understanding of the electronic and optical property of GaInNAs and the defect passivation in this material is critical to improve the overall efficiency.

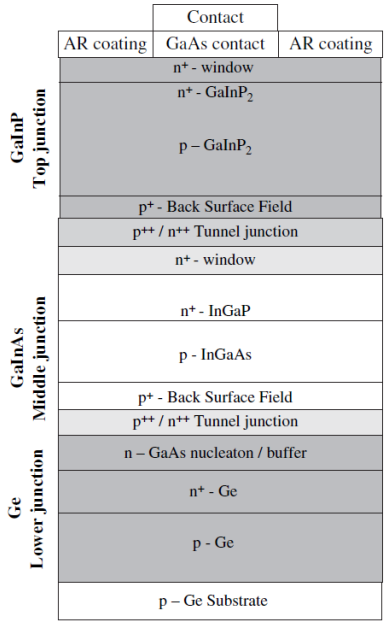

Figure 1. 2 Schematic cross-sectional view of a monolithically grown $GaInP_2$/InGaAs/Ge triple-junction space cell. (Reproduced from reference[118])

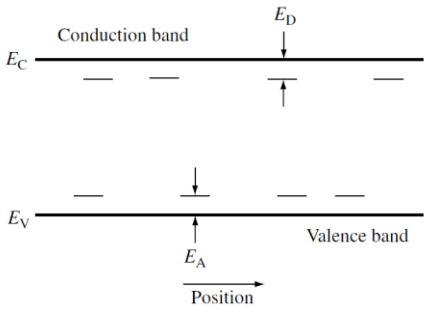

Figure 1. 3 Donor and acceptor levels in a semiconductor. The nonuniform spatial distribution of these states reinforces the concept that these are localized states. (Reproduced from reference[119])

1.4 Scope and Outline

Solar energy utilization is the main driving force of this dissertation. The aim is to provide a molecular level understanding of energy conversion in environmental and energy sectors through a series of computational and experimental studies. The topics fall in three energy conversion processes: (1) solar energy to electrical energy (photovoltaics); (2) thermally activated chemical reaction; (3) solar energy to chemical energy (plasmonic catalytic reaction). First-principles calculations, along with detailed kinetic study, give information about how hydrogenation proceeds via several surface reaction steps, like adsorption, reaction and desorption. We aim to provide insights to structural, electronic and optical properties of metal and semiconductor materials and aid materials design, as well as unravel mechanistic understanding of thermodynamic and kinetic details in hydrotreating processes.

The main body of the dissertation starts with a general introduction of density functional theory method in Chapter 2, including the exchange correlation functionals, algorithms for transition state search, as well as the possibility and limitations associated with density functional theory method.

Chapter 3 investigates residual defects of the N-related isoelectronic centers in dilute nitrides for their applications in photovoltaics. Using density functional total energy calculations, it is shown that the N-In complex may cause some of the residual defect levels evident in these materials. Moreover, these N−In effects can be neutralized through hydrogenation in a similar manner to that of the N−Ga complex. The calculated formation energies suggest the inherent stability of the N−In defect complexes and In-rich alloy fluctuations in dilute nitrides.

Chapter 4 consists of the exploration of two two-dimensional light absorbing materials: phosphorene and franckeite, that show potential in the applications of optoelectronic devices. This chapter begins with the surface modification of atomically thin semiconducting phosphorene, which allows it to be processed in solutions. A series of examination of chemical functionalization of black phosphorus using phenyl, phenolate, and nitrene species, which were widely investigated for carbon-based material were conducted. It was found that covalent functionalization using nitrene-derived species introduces a strong P−N dative bond at the interface without perturbing its intrinsic electronic structure. These results suggest valuable tunability of the electronic properties of two-dimensional layered black phosphorus by covalent functionalization for future device applications. Furthermore, density functional theory study was performed on franckeite, a naturally occurring Van der Waals heterostructures consisting of layers of two-dimensional materials to obtain their optical absorption properties. The study provides a fundamental understanding of the optoelectronic behavior in a complex naturally occurring vdWH, and may pave an avenue toward developing nanoscale optoelectronic devices with tailored properties.

From this point, the dissertation is switched from materials property investigation to gaining insights in catalytic reactions that take place on noble metal surface. In Chapter 5, cyclohexene hydrogenation over Pd (111) and PdH (111) surfaces in H_2 atmosphere was carried out using DFT calculations along with experiments in a liquid phase. The reaction kinetic revealed that the hydrogen dissociatively adsorbs on different sites that don't compete with reactant cyclohexene and solvents. The rate determining step was determined in both cases, agreeing with experimental findings. First-principles calculations, together

with kinetic modeling, provide a comprehensive fundamental work on catalytic hydrogenation of a simple aromatic compound.

Chemical transformations on plasmonic metals can be enhanced under visible-light irradiation. Previous works explained this enhancement as energetic carriers being populated at the molecular orbitals of the reactants leading to bond dissociation. It remains unclear whether such energetic carriers can also assist with bond formation, which is a critical elementary step in reactions. In Chapter 6, we use the reduction of nitrophenol as a prototype reaction, and show that, when borohydride is used as a reducing agent, the reaction rate is greatly enhanced under plasmonic excitation. Density functional theory calculations suggest that an energetic electron positioned at the reactant frontier orbital lowers the barrier for nitrophenol activation. We find that the rate can be further enhanced if this molecular orbital can be decoupled electronically from the extended d states in the plasmonic metal using a thin film of insulator. This work thus provides significant new insights on the plasmonic bond formation and a valuable strategy to accelerate chemical reactions.

Finally, Chapter 7 concludes the main findings from contributions in the previous chapters and gives perspectives on the future directions towards better understanding of studied topics.

Chapter 2. Computation Methods

Modern theoretical method based on density functional theory (DFT) has evolved in last decade as a useful tool to describe surface reactions at atomic level by providing geometric and electronic insights of chemical reaction systems through the comparison of reasonable geometric configurations as well as their electronic properties. These reaction systems include but not limited to semiconductor processing, electrochemistry, and heterogenous catalysis. An essential characteristic of DFT modeling resides in detailed evaluation of a series of elementary processes of competing catalytic cycles, including the adsorption, diffusion, dissociation, recombination, and desorption at catalyst surface and interface, through which the stability of intermediates and kinetic parameters of every step are generated and compared. These thermokinetic data can then be introduced in kinetic models to predict macroscopic data (such as turnover frequencies, selectivity) where kinetic fitting is no longer needed. In addition to kinetic data, DFT modeling can also be employed to interpret experimental spectroscopy data, e.g. IR, XPS, NMR, etc leading to guidance and verification of active sites and important intermediates on the catalyst surface. Moreover, experiments on well-defined model systems benchmark theoretical calculations so that the built models can be more reasonable and accurate. All in all, experiment and theory go hand in hand in the understanding and prediction of more efficient energy storage and conversion systems.

Here in this Chapter, an overview of density functional theory method is presented. It consists of details of fundamental background of the method, the exchange-correlation functional, the transition state search, the density of states and band structure, as well as the delta self-consistent field method.

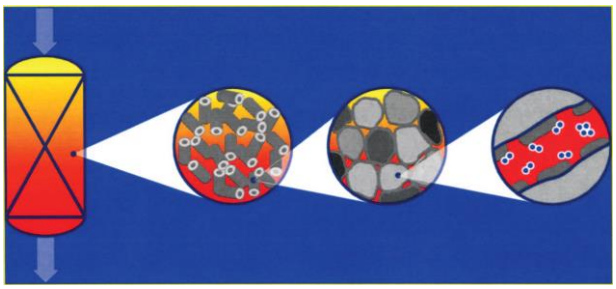

Figure 2. 1 Heterogeneous catalysis at different length scales: from reactor design to molecular level insight. (reproduced from reference[120])

2.1 Density Functional Theory Method

The fundamental of electronic structure calculations is the many-body time-independent Schrödinger equation:

$$\widehat{H}\psi = E\psi$$

where $\widehat{H}$ is the Hamiltonian, ψ is the many-electron wavefunction of the system, and E is the total energy.

For many-body N electrons systems, such as reaction surfaces in reaction systems and electron-electron interaction in solid physics, solving the Schrödinger equation is challenging. Therefore, following the Born-Oppenheimer approximation, electronic energy E in the Schrödinger equation can be described as a function of the electron density $\rho(r)$:

$$E[\rho(r)] = T_{ni}[\rho(r)] + V_{nuc-e}[\rho(r)] + U_{e-e}[\rho(r)] + \Delta T[\rho(r)] + \Delta U_{e-e}[\rho(r)]$$

where $T_{ni}[\rho(r)]$ represents the non-interacting kinetic energy of electrons, $V_{nuc-e}[\rho(r)]$ is the nuclear-electron Columbic attraction, $U_{e-e}[\rho(r)]$ is the classical repulsion between electrons, $\Delta T[\rho(r)]$ is the corrections to the kinetic energy that account for electron-

electron interactions, and $\Delta U_{e-e}[\rho(r)]$ is the non-classical electron-electron interactions, respectively.

While the first three terms can be computed following the equations below,

$$T_{ni}[\rho(r)] = -\frac{1}{2}\sum_{i=1}^{n}\int \phi_i^*(r)\nabla^2\phi_i(r)dr$$

$$V_{nuc-e}[\rho(r)] = -\sum_{A=1}^{M}\int \frac{Z_A}{|r-R_A|}\rho(r)dr$$

$$U_{e-e}[\rho(r)] = \frac{1}{2}\iint \frac{\rho(r_1)\rho(r_2)}{r_{12}}dr_1dr_2$$

The expression of the last two terms remain unknown. The objective of density functional theory approach is to describe the last two terms accurately. To this end, Walter Kohn and Lu Jeu Sham developed Kohn-Sham density functional theory (KS-DFT)[121] in the framework of the two Hohenberg-Kohn theorems[122] that treats the intractable many-body problem as a tractable problem of noninteracting electrons moving in an effective potential. They stated that the total energy is composed of kinetic, Columbic and exchange-correlation functional $E_{xc}[\rho(r)]$,

$$E_{xc}[\rho(r)] = \Delta T[\rho(r)] + \Delta U_{e-e}[\rho(r)] = \int dr\rho(r)\varepsilon_{xc}[\rho(r)]$$

among which ε_{xc} is the exchange and correlation energy per particle of a homogeneous electron gas with density ρ, and the XC functional contains all the many-body effects and is the only unknown term. The exact expression of exchange-correlation energy must be approximated and is an ongoing discussion in DFT.

2.2 The Exchange-correlation Functional

As mentioned in the first section, hundreds of non-empirical and semi-empirical density functionals have been developed in the last 30 years for achieving better accuracy and increased efficiency in calculations. The well-known Jacob's ladder[123] shown in Figure 2.2 summarizes the hierarchy of the most popular XC functionals with increasing accuracy and computational cost. The simplest approximation is the non-empirical local-density approximation (LDA), which is solely based on the electron density as a function of coordinates:

$$E_{xc}^{LDA} = \int \varepsilon_{xc}(\rho)\ \rho(r) d^3r$$

Such functional treats the system as homogeneous electron distributed gas, which describes homogeneous bulk systems well but results in systematic errors in describing surface science and molecule bindings. In order to include non-homogeneity of the real system, generalized gradient approximation (GGA) was built upon LDA by taking into account the gradient of local electron density $\nabla\rho$. GGA functional is assigned to be the second rung in Jacob's ladder. Commonly used GGA functionals include PBE,[124] PW91,[125] revPBE,[126] RPBE,[127] etc. To further improve the accuracy, meta-generalized gradient approximation (MetaGGA) functional was developed that mainly depends on the second derivative of electron density $\nabla^2\rho$; however, improving accuracy comes with higher computational cost. While both factors are equally critical, there's always a tradeoff between the two, meaning that regardless of what accuracy level is chosen, one can never find the most accurate and least computationally expensive methodology.

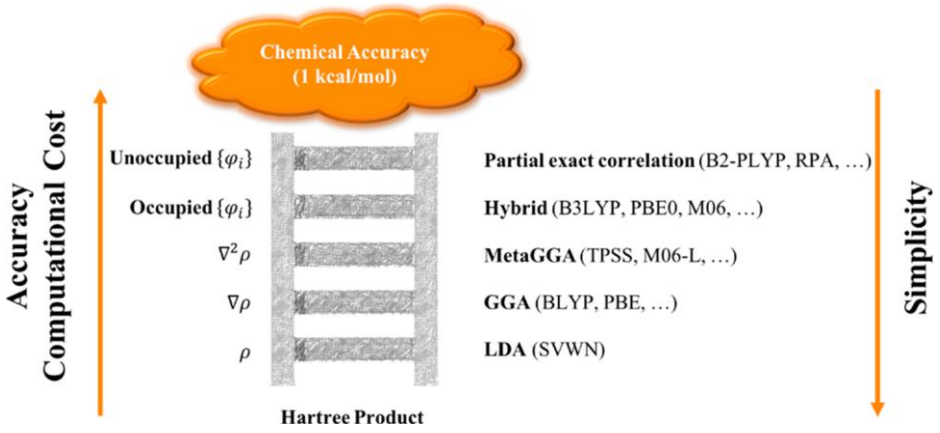

Figure 2. 2 Schematic representation of the various DFT approximations by increasing accuracy and computational cost and decreasing simplicity. Some representative and popular functionals are given for each rung. (reproduced from reference[128])

In materials physics, it is common to make some changes on the exchange part of the DFT functional by mixing regular XC functional with 20%-30% of exact exchange energy obtained from Hartree-Fock theory, known as the hybrid functional. Most widely used hybrid functionals include B3LYP[129, 130] (Becke 88 exchange functional and correlation functional from Lee, Yang, Parr), HSE,[131] PBE0,[132] and meta hybrid GGA.[133] They can be built upon regular LDA or GGA functionals by following the outlined equation:

$$E_{xc}[\rho(r)] = (1-a)E_{xc}^{DFT} + aE_x^{HF}$$

Notably, hybrid density functionals are extremely expensive in terms of computation time. Therefore, being able to employ it wisely and flexibly in chemical applications is crucial. For instance, one could utilize LDA or GGA functionals to obtain geometric structures, the resulting geometries can then be analyzed with hybrid functional to obtain

more accurate electronic band gaps or molecular properties (e.g. transition states). On the other hand, LDA and GGA approximations do not account properly for correlation effects in transition metal oxides and lead to self-interaction errors (SIE). The DFT+U method instead takes account the on-site Coulombic repulsion among localized d or f electrons by incorporating a Hubbard correction for delocalization and is relatively computationally affordable.[134, 135]

Another issue worth mentioning is the dispersion force in standard DFT calculations, typically the van der Waals (vdW) interaction that is not properly described in surface science and catalysis. The dispersion error is trivial for covalent bonding but is not negligible when it comes to non-local, long-range correlations between molecules and surface. Several dispersion corrections at a range of theory levels exist for the consideration of dispersion energy, namely, the Grimme DFT+D approaches,[136, 137] the vdw density functionals (vdw-DF).[138-141] In this dissertation, the effect of dispersion corrections was incorporated through the semi-empirical Grimme's DFT-D3 in PBE-GGA approximation, and the total energy composes of "standard" KS-DFT energy and dispersion correction energy.

$$E_{DFT-D3} = E_{KS-DFT} + E_{disp}$$

2.3 Transition State Search

Transition state in a chemical elementary step is shown schematically in Figure 2.3. it represents the potential energy maximum (saddle point) from reactant to product along a minimum energy path (MEP). It is of crucial importance for estimating the activation energy barrier within harmonic transition state theory.

$$A + B \overset{K_{AB^{\ddagger}}}{\Longleftrightarrow} AB^{\ddagger} \overset{k_{TST}}{\Longrightarrow} AB$$

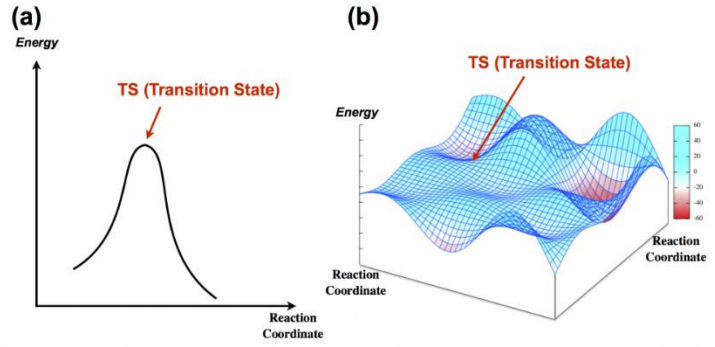

Figure 2. 3 Illustration of transition states in a (a) 2-D and (b) 3-D potential energy surface. (reproduced from https://computational-chemistry.com/en/blog/transition-state/)

In this work, a potential transition state is found by optimizing a few intermediates between pre-converged initial and final states following the nudged elastic band (NEB[142]) method, that is, each image maintains equal distance between one another via spring force (does not allow intermediates slide to initial or final states) and finds its lowest energy possible simultaneously. This is the method for finding the minimum energy path connecting reactants and products. However, the highest energy image is still only a guess. Later, the dimer method[143] is used to optimize this potential transition state towards a saddle point, until it reaches the convergence (the force falls below pre-set threshold). Finally, the transition state is confirmed by performing a vibrational frequency test for all the atoms in the system and there should be one single imaginary frequency present (the second derivative of energy with respect to displacement $\frac{d^2E}{dx^2} < 0$).

2.4 Density of States and Band Structure

The density of states (DOS) is an important function that qualitatively describes the electron distribution in a system, and can be written as:

$$g(E) = \frac{1}{V}\sum_{i=1}^{N} \delta(E - E(\overrightarrow{k_i}))$$

Where V is the volume of a matter, N is the number of energy levels, $\vec{k}$ is the wave vector, and i is the coordinate.

The DOS reflects the number of states at each energy interval. For atoms and molecules, their DOS should show discrete energy levels, while in the case of matters, their atomic orbitals overlap and form a continuous DOS distribution. Mathematically, the integration of DOS with respect to all possible energy should be equal to the number of states in the concerned system. By multiplying such value with the probability of occupation, which is essentially the fermi function $f(E)$, one can retrieve the number of charge carriers in a system, which is an essential concept in semiconductor physics.

$$n = \int_{-\infty}^{\infty} g(E)f(E)dE$$

In which the fermi function $f(E)$ is

$$f(E) = \frac{1}{1 + e^{(E-E_F)/kT}}$$

n denotes the number of charge carriers, E_F is the fermi level, k is the Boltzmann's constant, and T is the temperature. Importantly, the probability of occupation changes as a function of temperature (Figure 2.4), indicating the dynamics of electrons is influenced by the thermal energy.

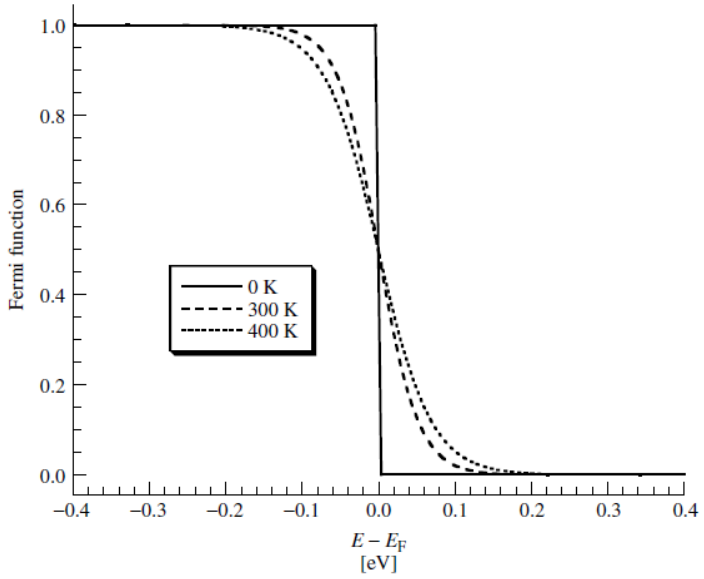

Figure 2. 4 Fermi function versus energy at various temperature. (reproduced from reference[119])

The band structure represents the energy of bands along high symmetry points in the Brillion zone (reciprocal space). Importantly, energy range that has crowded bands correspond to a higher density of states, as is shown in Figure 2.5. Band gap, also called forbidden gap, is a range of energy with no band covered. The most concerned band gaps in a solid is the band gaps near the fermi level. According to band gaps surrounding the fermi level, materials are categorized into metals, semiconductors and insulators.

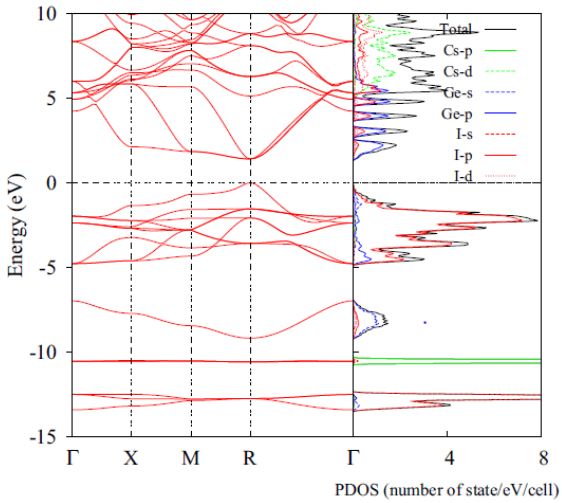

Figure 2. 5 The relationship between the density of states (DOS) and band structure in the cubic $CsGeI_3$. Different orbitals are shown for each element in the DOS plot. (reproduced from reference[144])

2.5 Excited State Calculations

Kohn-Sham-based ground-state DFT calculations are employed for simulating reaction kinetics in thermal-activated catalytic reactions, mainly due to electrons having shorter lifetime than nuclear motions so that the electrons can be seen as relaxed at ground state at all times. However, for photocatalytic reactions on metallic surface, it is essential to recognize the role of charge carriers in bringing chemical system onto excited potential energy surface. A number of methods can be used to describe excited states on metallic surface, including time dependent DFT (TDDFT[145]), constrained DFT,[146, 147] ΔSCF,[148, 149] linear-expansion ΔSCF,[150, 151] and the embedding theory approaches.[152] High accuracy is desirable in determining resonance energy as well as excited state PES in photocatalysis, however the computational cost of most methods are the major

drawbacks. Thus, in this study, the ordinary ΔSCF method (based on the energy difference between two self-consistent-field calculations), which has similar computation cost to the standard DFT method, was used for estimating the resonance energy at ground state minimum in the system. It is achieved by placing an electron into an identified high-lying single KS orbital with the largest overlap over the molecular orbital, and the resonance energy is obtained by subtracting the total energy with electron input at the ground state minimum with the ground state total energy at the same vertical point (vertical excitation energy). To simplify the calculation, the targeted KS state is identified at the gamma point and is kept consistent throughout the entire excited PES calculations in order to avoid the discontinuity with *k*-point sampling.

Chapter 3. Role of In in Hydrogenation of N-Related Complexes in the light-absorbing material GaInNAs

3.1 Introduction

Multi-junction solar cells (MJSCs) have emerged as one of the most promising technologies in achieving high efficiency sunlight to electricity conversion.[153-155] These solar cells boost the cell efficiency by combining mechanically stacked semiconductors with different band gaps to absorb a much wider range of wavelengths.[156, 157] The dilute nitride semiconductor compounds are great candidates of the third junction material in a four-junction MJSCs.[158] GaInNAs quaternary alloys have long been investigated for this purpose, since they can perfectly match the lattice of GaAs or Ge substrates for MJSCs through metal-organic chemical vapor deposition[159] or molecular beam epitaxy.[160] In addition, $Ga_xIn_{1-x}N_yAs_{1-y}$ has a direct band gap around 1 eV,[161] which is ideal for the third junction of the next-generation ultra high-efficiency MJSCs.[162]

However, GaInNAs quaternary alloys suffer from defect-induced short minority-carrier diffusion lengths, which has impeded their use in high-efficiency photovoltaics.[163, 164] One major issue is that, due to the smaller ionic radii and larger electronegativity of N than As, the substitutional N atoms attract a high charge density locally.[165] These isoelectronic centers act as the localized states inside the band gap thus, inducing a strong bowing of alloy band gap even in the high-quality nitrides.[166] In addition, alloy and compositional fluctuations and deep N-N centers further impact the optoelectronic performance of these systems. These trap states greatly shorten the carrier diffusion length, which in turn lowers the photocurrent of GaInNAs layer.

Hydrogen may play a key role in the restoration of the material band gap while

preserving the substitutional nitrogen.[167-169] For example, it was reported that N radiative recombination centers in $GaAs_{1-y}N_y$/GaAs heterostructures were fully quenched by H irradiation in photoluminescence measurements.[170] After hydrogenation, a strong and reversible blue shift in the photoluminescence (PL) spectroscopy of partially hydrogenated $In_xGa_{1-x}As_{1-y}N_y$ heterostructures has been observed.[171] Both experimental findings have been attributed to the formation of N-H bonds;[170, 171] passivation of N isoelectronic centers may also lead to the higher solar cell performance observed in the hydrogenated samples.[169] First-principles calculations revealed that H acts as a donor and that the formation of N-H_2* leads to the neutralization of nitrogen effects; the dangling bond at Ga as a result of N-H bond formation can be fully passivated upon incorporation of the second H.[167, 168]

Our previous experimental PL spectra showed the reduction of peak intensity of the localized states after hydrogenation using an UV-activated process, indicating reduction of the N-related isoelectronic centers.[172] DFT calculations showed that the hydrogenation helps mitigate defect levels within the bandgap by the formation of Ga-N-H_2* complexes. However, the "s-shape" – initial blue shift of the PL spectra maximum followed by a red shift when increasing temperature – remained even after the highest hydrogen dosage, indicating some residual defects remain in the samples which are difficult to remove.[169, 172] The exact nature of these residual defects remains relatively unknown, but it typically attributed to unintentional alloy fluctuations associated with indium segregation and decomposition. One possible defect is the In-N complex. Previous experiments showed that introducing N into GaInAs caused alloy fluctuations – spatial inhomogeneity of the In/Ga ratio[173] while, the formation of N-In bonds and

clusters may be responsible for the carrier localization.[174, 175] It remains unclear if the N-In complex is susceptible to hydrogenation.

Here, density functional theory (DFT) calculations are reported, through which the stability of N-In complex is shown; as well as, comparing its hydrogenation process to the N-Ga complex in GaInAsN. It is shown that the N-In effects can be neutralized through hydrogenation, similar to the N-Ga defects. Furthermore, it is shown that hydrogenation of N-In bonds is thermodynamically less favorable than the N-Ga bonds. The N-In defects may persist under hydrogenation and localize charge carriers manifested by the experimentally observed residual defect levels in the PL spectra. Revealing the nature of the N-related defects may help improve the performance of GaInAsN in MJSCs.

3.2 Computational and Experimental Methods

3.2.1 Experimental methods

Two 1 μm-thick $Ga_{0.91}In_{0.09}N_{0.028}As_{0.972}$ layers grown by molecular beam epitaxy are studied. Each GaInNAs sample was grown at 420 °C on a GaAs substrate and capped by a 75 nm GaAs layer. To improve materials quality and reduce strain in the bulk dilute nitride, a 550 nm GaAs buffer was also deposited at 580 °C prior to growth of the GaInNAs film. The samples were first annealed post-growth in nitrogen-rich conditions at 800°C for 30 seconds. The sample was then cleaved into two pieces one hydrogenated using a UV-activated process at a dose of 1.1 x 10^{15} atoms/cm^{-2}. Analysis of the hydrogen penetration indicated penetration throughout the full nitride active layer. For photoluminescence (PL) analysis, the samples were placed in close-cycle cryostat and

excited with a diode pumped solid state laser at 532 nm and detected using a LN_2-cooled InGaAs array.

3.2.2 Computational methods

The plane-wave DFT calculations were carried out using Vienna Ab initio simulation package (VASP[176]). The Perdew-Burke-Ernzerhof generalized gradient approximation exchange-correlation potential (PBE-GGA[177]) was used. The electron-core interactions were treated in the projector augmented wave (PAW[178]) method. The van der Waals interaction has been taken into account through Grimme's DFT-D3 semi-empirical method.[137, 179] A 2×2×2 supercell of 64 atoms consisting 29 Ga atoms, 3 In atoms, 1 N (substitutional N) and 31 As atoms was generated to model the sample compositions in the experiment ($Ga_{0.91}In_{0.09}N_{0.028}As_{0.972}$). Structures were optimized using a k-point mesh of 3×3×3 for structural optimizations with a kinetic cutoff energy of 400 eV. The structures were relaxed until the force acting on each atom was smaller than 0.02 eV $Å^{-1}$. The electronic energies were converged until the maximum energy change between two steps is smaller than 10^{-6} eV.

The Density of States (DOS) calculations in this study were calculated by applying HSE06 (Heyd-Scuseria-Ernzerhof) functional[180] to accurately predict band gaps of semiconductors, since the band gaps calculated with pure GGA potential are underestimated.[181] The same k-point grid was employed for DOS calculations.
The formation energy of hydrogen was evaluated by the following the equation:

$$E_{Hydrogenation} = E_{GaInNAs\text{-}nH} - (E_{GaInNAs} + n \times 1/2E_{H2})$$

Where n, $E_{GaInNAs-H}$, $E_{GaInNAs}$ and E_{H2} are the number of hydrogen atoms involved in the hydrogenation, the total energies of hydrogenated GaInNAs, pristine GaInNAs, and an isolated H atom (half H_2 in the gas phase), respectively.

3.3 Results and Discussion

Two samples with the composition of $Ga_{0.91}In_{0.09}N_{0.028}As_{0.972}$ were studied in the UV-activated hydrogenation processes. One was kept unhydrogenated as the reference sample and the other sample hydrogenated at 1.1×10^{15} atoms/cm^2. PL was then performed on both samples at a range of temperatures.

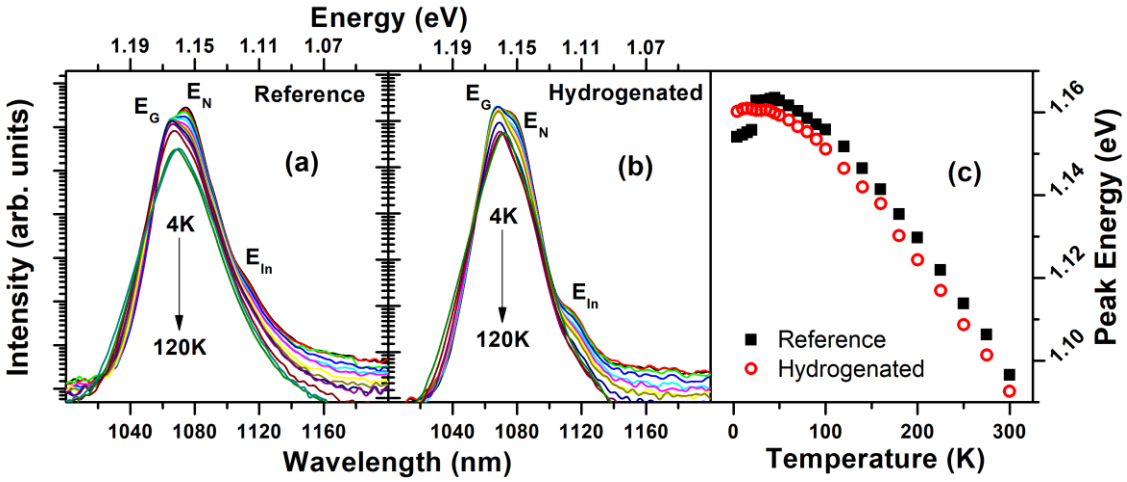

Figure 3. 1 Temperature-dependent photoluminescence from 4 K to 120 K for (a) an unhydrogenated GaInNAs layer, (b) a hydrogenated GaInNAs layer from the same sample, and (c) the peak PL energy as a function of temperature. E_G denotes the fundamental band gap energy, E_N denotes the defect bands, and E_{In} involves In rich clusters.

The PL spectrum of the reference sample is shown in Figure 3.1(a). At low temperatures, the luminescence is dominated by carriers localized at lower energy (longer

wavelength), $E_{N,}$ than the fundamental band gap energy, E_G. The origin of E_N has been attributed to alloy fluctuations,[182-184] while the effective band gap of the GaInNAs results from the interaction of the conduction band states and N-related isoelectronic centers. This results in a significant reduction of the bandgap due to the band-anticrossing effect.[185] As the temperature increases, there is a switch of the dominant peak from E_N to E_G showing that recombination of carriers occupying the conduction and valence bands start to dominate the PL. This transition occurs around 40 K when carriers trapped at localized states gain the required thermal energy to deionize and redistribute into unoccupied conduction band states. The peak PL energy at each temperature is summarized by plotting the peak PL energy as a function of temperature, as shown as closed (black) squares in Figure 3.1(c). Here, it is observed that the spectra present an "s-shape" dependence as the temperature increases, which is attributed the redistribution of photogenerated carriers from E_N to $E_{G.}$ Followed by, the decrease of the energy gap as a function of temperature.[186]

Let us now turn to the PL spectra for the hydrogenated sample. From Figure 3.1(b) it is evident that there is a reduction in the intensity of the low-energy shoulder, associated with localized states, E_N, and the PL is dominated by the free carrier emission at E_G even at very low temperatures. This arises from the fact that hydrogen atoms have partially passivated the effect of the localized states. As expected, E_G continues to dominate and blue shifts to a lower energy as the temperature increases. This is reflected in Figure 1(c), where the peak PL associated with the bandgap (E_G open red circles) follows a typical Varshni-type dependence.[186] However, the contribution of emission from carrier localized at E_N remains even after this relatively high hydrogenation

process,[172] see Figure 3.1(b). Since these localized states are extremely hard to remove, it is postulated that this provides further evidence for the picture that these centers arise due to alloy fluctuations that originate from indium segregation during growth of the GaInNAs.[183, 184] If that is the case, they may require a higher excitation power or an even higher hydrogen dosage for a complete removal.

Finally, it is also evident in Figure(s) 3.1(a) and (b) that a third feature is evident at lower energy (longer wavelength), E_{In} at ~ 1.1 eV. Particularly at low temperatures, the narrowed width of E_{In} leads to a more pronounced feature in the PL spectra, though its overall contribution is similar at the various temperatures. Previously, lower energy transitions have been attributed to N-N clusters and defects.[169] However, such large nitrogen-derived clusters could be selectively passivated by the hydrogenation process, and almost completely removed from PL spectra at the levels of hydrogenation used here, see Ref [169]. In Figure 3.1(b), it appears that the hydrogenation process has little *direct* effect on the complexes that constituent this transition, such that its overall contribution to the PL does not appear to significantly decrease. Since the homogeneity of the system is improved and the contribution of defects and impurities is reduced, the resolution of E_{In} is improves and its contribution to the emission is more clearly resolved. As such, it is not believed that that E_{In} is associated with nitrogen related defects, but rather tentatively attributed to the formation small inclusions or phases of InAs, which are known to form in these systems.[187] While the emission energy of InAs QD-like centers is consistent with the peak observed, the effect of hydrogen (or not) on such centers remains relatively unknown and is now currently under investigation.

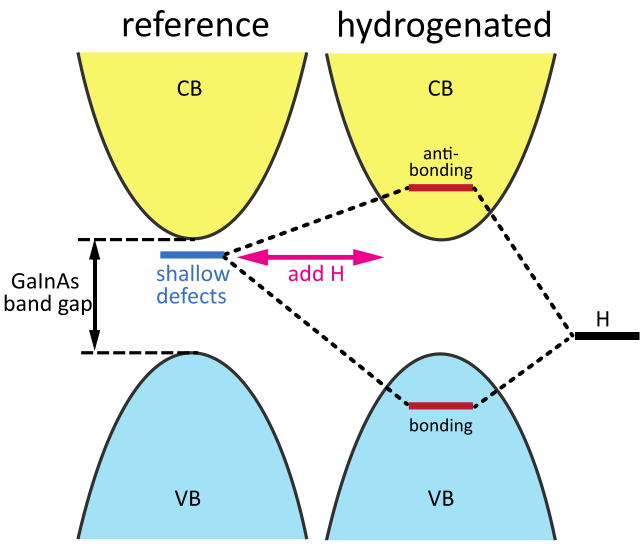

Figure 3. 2 A schematic plot of the effect of H on the restoration of the GaInAs bandgap. Hydrogenation pushes the N-related localized levels (blue line) into the band continuum.

Here, the nature of the N-related defects in GaInNAs using the plane-wave DFT method is investigated. Previously, the role of hydrogen in selectively passivating the N effect by forming a Ga-N-H_2* complex and the resulting restoration of the host material band gap has been reported.[172] As shown in Figure 3.2, hydrogenation of both N and Ga removed the defect levels in the band gap and push these states into the continuum. In the present work, the same supercell of 64 atoms is used with the same nitrogen content added to the host as our earlier work to take into consideration the In-N effect. Several GaInNAs structures were modeled, as summarized in Figure 2 and discussed below.

Figure 3.3(b) presents the atomic geometric arrangement of 64 atoms, which includes 29 Ga atoms, 3 In atoms, 1 N atom, and 31 As atoms corresponding to the experimental sample. Three In atoms are evenly distributed between planes. The N is bonded to an In on the second (111) plane to generate an In-N bond. This single In-N bond brings total energy of the system down by 0.2 eV; this stabilization can be caused

by either a stronger bond of In-N with respect to Ga-N or by minimizing the local mechanical strain caused by different atomic sizes of In and Ga. In the optimized structure of GaInNAs, the In-As bond is about 0.13 Å longer than Ga-As (Figure 3.3(a)); indeed, this induces a local tensile stain which may be compensated by a substitutional N with a smaller atomic radius.

After breaking the In-N bond, it is found that the first hydrogen prefers to form a bond at the bond-center site between N and In (Figure 3.3(c)) since N is more electronegative than In. While, the second H saturates the In dangling bond and forms a stable In-H_2-N complex. Another possible bonding configuration is considered in which the second H adsorbs on the opposite site of In (Figure 3.4(a)). Notably, both configurations exhibit similar total energies and electronic structures. Therefore, only In-H_2*-N is reported in this study. The In-N bond broken upon ligation of H pushes the N downward to the first neighboring Ga_3 plane, which lifts In toward the first neighbor As_3 plane; the corresponding N-H and In-H bond length is 1.04 Å and 1.92 Å, respectively (see Figure 3.3(c)).

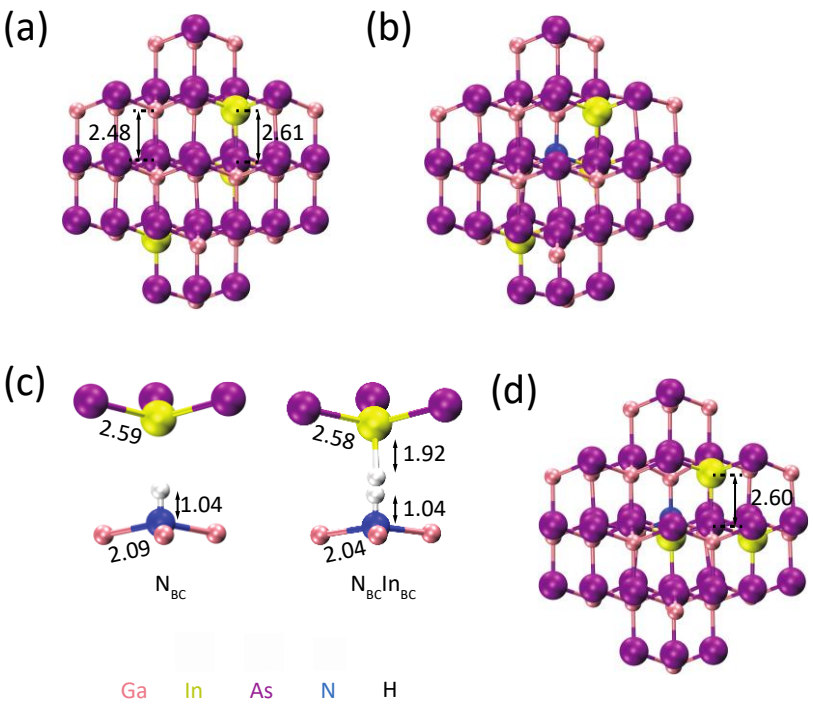

Figure 3. 3 The structures of (a) GaInAs, (b) GaInNAs with the single N attaching an In on the second plane. (c) Structures of H adsorbed on the bond-center sites of N and In, (d) GaInNAs with the single N attaching an In cluster. All the bond lengths are in Å. Pink, purple, yellow, blue and white balls represent the Ga, In, As, N, and H atoms, respectively.

Next, to further demonstrate the effect of In-N bonds, a structure was created with an InAs cluster right next to the N, where the three In atoms and one of the Ga atoms form a tetrahedron as shown in the inset of Figure 3.3(b). The N is bonded to In in a similar manner as in the previous structure (Figure 3.3(d)), giving a similar total energy regardless of whether the InAs cluster is present. This is probably due to the reduced mechanical strain caused by the N incorporation being a very localized effect; thus, only influencing the first and second nearest neighbors, while In atoms further away from N are not affected.

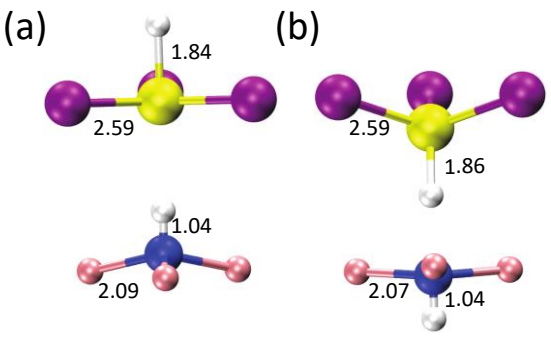

Figure 3. 4 Structures of H adsorption (the configuration shown in Figure 3.3b) (a) on the bond-center sites of N and the opposite site of In, (b) on the opposite site of N and In.

The final proposed geometry has the single N replacing the As in the center of the tetrahedron shown in Figure 3.3(d) to generate three In-N bonds (Figure 3.5(a)). In the presence of three In-N bonds, the total energy drops by 0.5 eV, which results from two more generated In-N bonds. Similarly, hydrogenation of the N at the bond-center site pushes N down, and the displacement of the In atom that was initially bonded to the N is significant. The calculated bond length is 1.04 Å for N-H, which is in agreement with the first structure. However, we observed the bond length of In-H decreases from 1.92 to 1.89 Å (Figure 3.5(b)). This reduced bond length is further supported by the calculated hydrogen formation energies summarized in Table 1, where a clear comparison of all the structures is shown. The more positive hydrogen formation energies are attributed to higher stability of InN complex likely caused by the mechanical strain induced by clustered In atoms. Furthermore, by having three In-N bonds, the formation energies to achieve the first hydrogenation of N, as well as, the second hydrogen addition to In are much more positive. This indicates that hydrogenation becomes less favorable with more In-N bonds.

Table 1 Total energy and formation energy (per H) values of all the configurations reported in this work. All the energy values are in eV.

Property	Previous reported Ga-N defect	In-N[b]			In_3-N[c]	$In_3 \equiv N$[d]
Total energy[a]	0	-0.2			-0.2	-0.7
$E_{Hydrogenation}$ (1^{st} H on N)	0.2	N(H)-In		(H)N-In	0.4	0.5
		0.4		0.6		
$E_{Hydrogenation}$ (2^{nd} H on Ga/In)	0.1	N(H)-(H)In	N(H)-In(H)	(H)N-(H)In	0.6	0.9
		0.6	0.9	0.6		

[a] Total energy of GaInNAs using the Ga-N bonding configuration (N with all four neighbors as Ga atoms) as the reference. The structure is shown in Appendix Figure A. 6

[b] The structure shown in Figure 3.3b, one N bonded with one In atom.

[c] The structure shown in Figure 3.3d, one N bonded with one In atom in an InAs cluster.

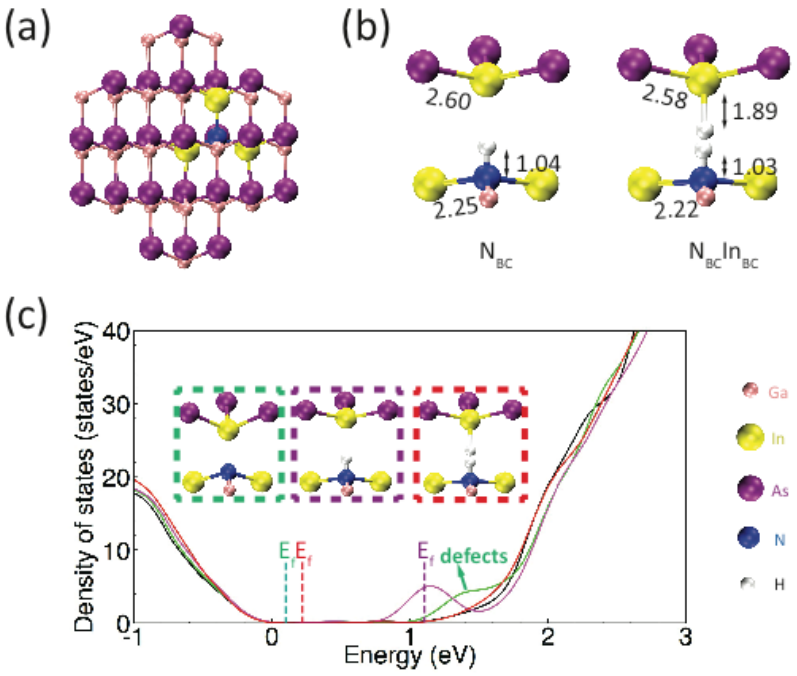

Figure 3. 5 The structures of (a) GaInNAs with the single N sitting on the top triangular pyramid of In cluster to generate three In-N bonds, (b) the adsorption of H on N and In by breaking the In-N bond. (c) Total density of states plots for the GaInNAs structure in (a) (green curve), H adsorption on bond-center site next to N (purple curve), and N-H-H-In complex (red curve). The DOS for original GaInAs (black curve) is plotted as reference. The zero-energy level is set at the valence band edge. All the bond lengths are in Å.

All the total energies of N-substituted GaInAs shown in Table 1 are close to each other (-0.2 to -0.7 eV), indicating that all geometries could occur in samples. This similarity of energies indicates that the structure of the N-related defects may be determined by the growth and annealing kinetics in the experiments. To gain deep insights into the interaction between the host material and H, the total density of states (DOS) was computed on various (above mentioned) GaInNAs geometries. From the DOS

plot in Figure 3.5(c), the presence of N gives rise to electronic levels at the conduction band edge (green curve). These energy levels are shown to produce a reduction in the fundamental bandgap, E_G, associated with the interaction of nitrogen isoelectronic impurities and the conduction band states in dilute nitride compounds.[185] The material remains p-type. Electronically, the formation of the N-H bond pushes these localized energy levels into the band gap and the material tends to be slightly n-type. This is in agreement to the experimental[160] and theoretical studies[168] in the literature that suggested this monoatomic H acts as a donor in the band gap. More importantly, with hydrogen addition at the In site, there is an overlap between the original GaInAs (black curve) and In-H_2*-N DOS (red curve), which suggests that the In-H_2*-N complex plays a crucial role in pushing the localized states into the conduction and valence bands.

3.4 Conclusions

In this work, significant In-N-related defects in GaInNAs compound have been investigated by performing density functional theory calculations on various In-N bonding configurations. Calculations show that all three configurations containing In-N-related defects could be hydrogenated in a similar manner. As more In-N bonds are brought in, a significant enhancement of the system stability is observed. Electronically, the introduction of H_2 is seen to be beneficial to In-N centers, restoring the band energy of the host material GaInAs by forming N-In dihydrogen complexes. However, the hydrogenation of N-In complex is thermodynamically less favorable than those of the N-Ga complex (N with all four neighbors as Ga atoms), indicating that the In-N-bonding defects might be left unhydrogenated under real circumstances. Ultimately, the present

work gives a meaningful explanation for the stability of scattering centers that continue to contribute to the PL even after hydrogenation, which motivates further research on the passivation of dilute nitride semiconductor compounds.

Appendix A contains details of structures and formation energies of H, and density of states plots.

Chapter 4. Potential Two-dimensional Light Absorbing Materials

4.1 Rational surface modification of two-dimensional layered black phosphorus

4.1.1 Introduction

Two-dimensional black phosphorus (BP),[188-191] known as single layer phosphorene, is a member of layered-material family consisting of graphene, 2D hexagonal boron nitride, and transition metal dichalcogenides ranging from semi-metals to semiconductors and to insulators. Semiconducting BP shows a tunable direct band gap, anisotropic optical absorption, and large carrier mobility, all of which may lead to potential applications in field-effect transistors and photodetectors.[191-195] However, its fast degradation upon exposure to ambient conditions, resulting from reaction with oxygen,[196, 197] necessitates surface functionalization and encapsulation to prepare devices with long-term stability and reliability.[198-200]

Chemical functionalization of atomically thin two-dimensional materials enables tunable electronic and chemical properties and also allows solution-based techniques for processing these materials. Covalent functionalization of pristine graphene and carbon nanotubes has been widely studied. The rich chemistry of carbon enables various strategies for introducing foreign groups through covalent bonds, such as using aryl radicals, cycloaddition, and nitrene addition or mediated by surface atomic defects or impurities.[201-205] By introducing these radicals onto the surface, the band gap, electronic conductivity and solubility of graphene can be controlled.[206-209] Because of the varied chemical properties resulting from different atoms exposed to the environment, surface

modification through covalent bonds for BP has been challenging as compared to graphene. That is, the P atoms exposed at the surface of BP have distinct chemistries with respect to C in graphene.

Covalent functionalization of exfoliated BP remains being less explored although it may be more crucial because of its fast degradation upon exposure to ambient conditions.[196-199] Within the context of introducing a protective layer on BP surfaces against ambient degradation, several encapsulation techniques have been proposed including the encapsulation of BP with transparent polymethyl methacrylate (PMMA)[210] and insulating hexagonal boron nitride (h-BN).[211, 212] For the same purpose, by using trimethylaluminum (TMA) and H_2O as precursors, a thin AlO_x film can be deposited onto BP flakes by atomic layer deposition (ALD).[213] Very recently, aryl diazonium chemistry - a widely studied chemistry for graphene - has been applied to BP, and the functionalized samples showed enhanced semiconductor performance and improved chemical stability resulting from the surface passivation.[214] However, the aryl group may also introduce a flat energy band within the band gap of BP leading to reduced hole mobility as shown recently in first-principles calculations.[215] Therefore, stable covalent functionalization of BP to modify its chemical stability and solubility without diminishing its desirable electronic properties still remains to be developed.

In this study, we report first-principles density functional theory (DFT) calculations, through which we propose alternate strategies to modify the BP surface. We apply the radical chemistry using three different radicals including phenyl, phenolate, and nitrene, all of which have been widely explored previously for surface modification of graphene and carbon nanotubes, to functionalize BP and examine their adsorption

properties and binding strength. In particular, we show that all three radicals can adsorb on the BP surface. Different adsorption modes, resulting from the varied electronic structure of the radicals, affect the electronic properties of BP in a significantly different way. We show that the nitrene chemistry may be a valuable strategy for BP functionalization since the interfacial binding is stable without perturbing the electronic structure of BP, resulting from a strong P-N dative bond at the interface. Meanwhile, we find the formation of dangling bonds is the main cause for defect levels at the Fermi level in BP when using phenyl and phenolate. We further compare the results with other nitrene-derived functional groups on BP, including N-methylbenzene, N-aminobenzene, and N-nitrobenzene. We show that, by tuning the polarity of the molecules, the work function of BP can be tuned with a 2-eV energy window. These results thus suggest valuable tunability of electronic and chemical properties of layered black phosphorus by covalent functionalization.

4.1.2 Computational Methods

DFT computations were performed using Vienna ab initio simulation package (VASP)[176]. The ion–electron interaction was described through the projector-augmented wave (PAW) approach[178]. For the structural optimization, the exchange and correlation energy was represented using the Perdew-Burke-Ernzerhof (PBE) functional of the generalized gradient approximation (GGA)[177]. The van der Waals (vdW) interaction has been taken into account through the Grimme's DFT-D3 semi-empirical method.[216, 217] To model the monolayer, we used a supercell contains 36 P atoms. The Brillouin zone was sampled using a k-point mesh of 3×3×1 for structural optimizations. A vacuum space of

at least 10 Å was included in the supercell to minimize the interaction between the system and its replicas resulting from the periodic boundary condition. A 400 eV cutoff for the plane-wave basis set was adopted in all computations. The structures were relaxed until the atomic force is smaller than 0.01 eV/Å.

The optimized structures were then used for the electronic density of states calculations using the HSE06 hybrid functional.[218] All the calculations were performed using a Gaussian smearing with a width of 0.2 eV. We have tried to increase the cutoff energy to 500 and 600 eV for the DOS calculations with a smaller smearing width of 0.02 eV and observed no significant difference (see Fig. B6). For comparison, DFT-PBE calculated electronic structure is shown in the supplementary materials (Figure B. 1). The calculated electronic structures using HSE and PBE functionals give the same trend and support the conclusion. The band gap is calculated based on the eigenstates at the Γ point in the Brillouin zone of BP. The work function of pristine and functionalized BP was calculated based on the difference between the Fermi Level and the vacuum level.
The adsorption energy of each configuration between the molecule and the 2D BP is defined by $E_{ads} = E_{total} - (E_{BP} + E_{adsorbate})$, where E_{total}, E_{BP}, and $E_{adsorbate}$, are the energies of functionalized 2D materials, pristine 2D materials, and the isolated functional group, respectively.

4.1.3 Results and Discussion

4.1.3.1 Organic Lewis Acids

Figure 4. 1 shows the projected density of states (PDOS) of BP with three different functional groups, namely phenyl, phenolate and nitrene species.[203] Calculations

using HSE06 hybrid functional show that the pristine BP monolayer has a band gap of 1.34 eV (Fig. 4. 1a), which agrees with reported values.[219-221] The adsorption of phenyl (Fig. 4. 1b) and phenolate (Fig. 4. 1c) introduce energy levels within the band gap of pristine BP. This localized states within the band gap is also found in a recent computational work and may lead to reduced hole mobility of BP.[215] Partial charge density calculations within an energy window around the Fermi level have been performed to illustrate the charge distribution (insets in Figure 4. 1). The green shaded area in Fig. 4. 1b and 4. 1c shows the energy window used for integration.

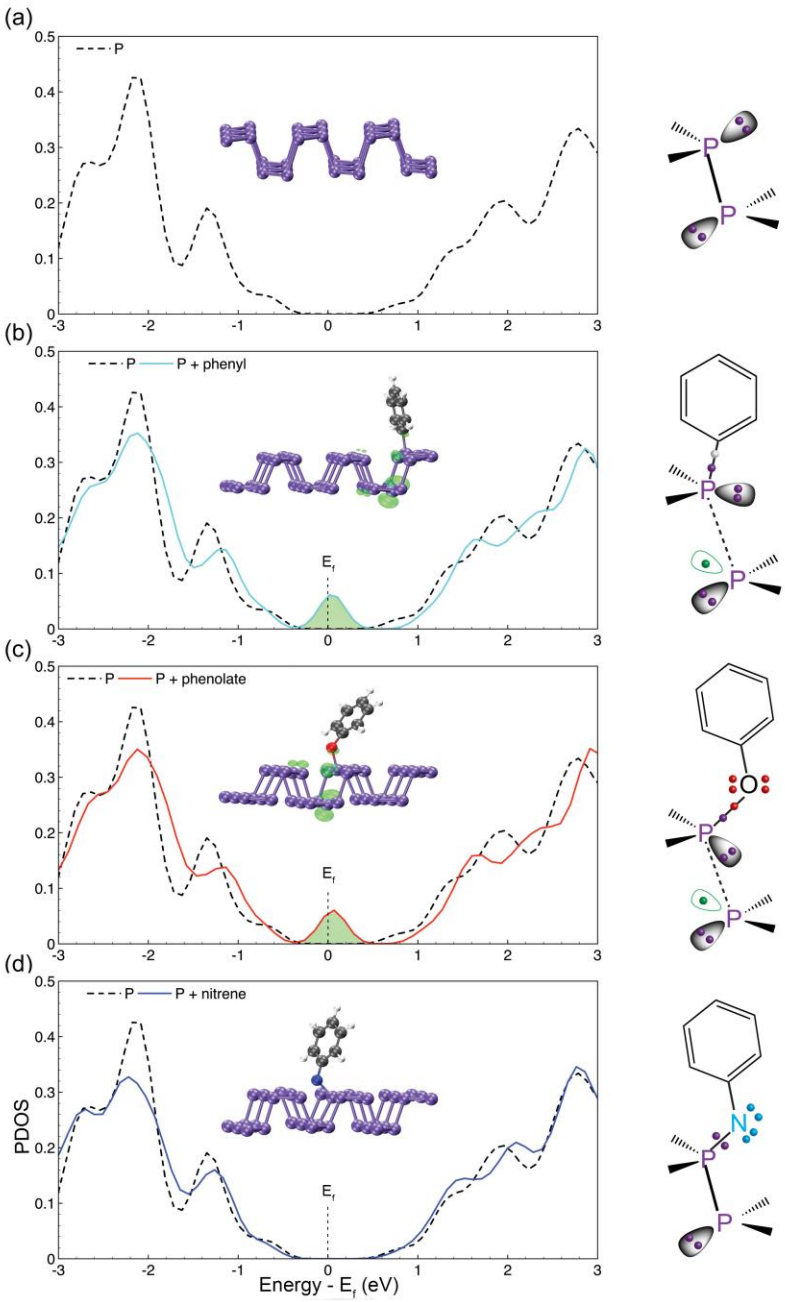

Figure 4. 1 Electronic structure of BP with different functional groups (a) pristine BP, (b) phenyl, (c) phenolate, and (d) nitrene as well as the optimized structures (insets). Density of states (DOS) of pristine BP (dashed curve) and projected DOS onto P atoms (solid curves) are shown to compare. The black, white, red, blue, purple balls denote C, H, O,

N, and P atoms, respectively. The shaded areas indicate the energy window used for charge integration for the whole system. In (b,c), the isosurface of the charge density plot is 0.06 eV $Å^{-3}$. Configurations of interfacial bonds formed between functional groups and BP are schematically shown next to each optimized structure.

We find that the charge around Fermi level is localized at the phosphorus at the opposite site of BP with respect to the surface being functionalized. As discussed later, this charge localization is caused by the broken P-P bond upon ligation of the phenyl (Fig. 4. 1b). Because of the same reason, that is, the newly formed P-O replaces previously existed P-P bond, functionalization using phenolate creates a very similar electronic structure (Fig. 4. 1c). Distinctly, when nitrene was introduced, the electronic structure of BP, particularly the band gap and band edge energies remain unperturbed as compared to the pristine BP. Note DFT-PBE calculations show the same phenomena. The projected DOS of the C, O, and N in the phenyl, phenolate and nitrene in the adsorbed configurations are shown in Fig. B2. The overlapping states between C (O) and P in phenyl (phenolate) at the Fermi level clearly show the orbital hybridization. We also calculated the band structure of pristine monolayer and nitrene-functionalized BP using the PBE-D3 method, as shown in Fig. B3. The band structure calculations show that adsorption of nitrene on the BP surface does not perturb the intrinsic electronic structure of BP. The direct band gap at the Γ point persists. Note the band gap is underestimated using PBE calculations as compared to the HSE calculations. All the discussion here is thus focused on the results calculated using the hybrid functional.

Table 2 Adsorption energy, bond length (Å) and other parameters of phenyl, phenolate and nitrene groups on monolayer BP. The positive and negative sign of the atomic displacement indicate the position change away from (stretching) and toward BP (compression), respectively.

Functional Groups	**Phenyl**	**Phenolate**	**Nitrene**
Adsorption Energy (eV)	-2.1	-1.0	-3.2
Bond Length (Å)	1.86	1.70	1.59
Top P displacement (Å)	0.165	0.101	–0.108
Bottom P displacement (Å)	0.292	0.181	0.003
P-P distance (Å)	2.96	2.64	2.21

Table 2 shows the adsorption energies of these radicals on BP. All the adsorbates are strongly bonded to BP, with the adsorption energy increasing from -1.0 eV for phenolate, -2.1 eV for phenyl to -3.2 eV for nitrene. Among the functional groups examined, phenyl and phenolate show similar adsorption configurations, in which the adsorption of phenyl (phenolate) lift the first layer P atom by 0.165 Å (0.101 Å), push the second layer P atom away by 0.292 Å (0.181 Å), and the corresponding (broken) P-P distance is 2.96Å (2.64 Å), which was 2.23 Å in pristine BP. By contrast, nitrene is more tightly bonded to the P atoms. The addition of nitrene pushes down the surface P atom 0.108 Å instead of pulling it outwards the sheet. Displacement of the bottom-side P atom is insignificant, and at the same time phosphorene possesses a much shorter P-P bond length (2.21 Å) as compared to the other two cases.

In the following we show the physical reason for the varied perturbation of the electronic structure caused by the different radicals. Figure 4. 2 shows schematically the three functional groups - phenyl, phenolate, and nitrene. The varied frontier orbitals, manifested by the charge density shown in Figure 4. 2, display the difference between electronic structures of the three radicals. The phenyl and phenolate has one unpaired electron in the p orbital, which is also evidenced by the calculated density of states in Figure B. 4, while the nitrene group has two valence electrons forming a free electron pair and two remaining electrons occupying two degenerate p orbitals. This different electron distribution leads to varied adsorption configurations and energies on black phosphrous as discussed later in the text. The density of states of these ligands is shown in the supplementary materials.

The varied perturbation can thus be explained based on the different electronic structure of the radicals and distinct interfacial chemical bonds. Each phosphorus atom is covalently bonded to three adjacent phosphorus atoms to form a puckered honeycomb structure[222, 223] in pristine BP. By forming three bonds with each neighbouring P atoms, each phosphorus atom also has a lone pair of electrons. The strong interaction between surface P and the unpaired electron in phenyl groups (P-C bond) leads to the broken P-P bond and localization of an unpaired p electron on the P atom at the bottom (Fig. 4. 1bc). This unsaturated P atom at the bottom dominates the charge localized at the Fermi level. The strength of interfacial interaction doesn't correlate with the amplitude of perturbation of the electronic structure. Although it has the strongest interaction with the BP surface, nitrene group has two valence electrons forming a free electron pair and two remaining electrons occupying two degenerate p orbitals. When introducing nitrene to BP, the

surface P atom shared its lone pair electrons with N in nitrene (Fig. 4. 1d) forming a dative covalent bond. In other words, the Lewis basic and nucleophilic P atom at the surface attacks, through the lone pair of electrons, the Lewis acidic nitrene species. This bond is very strong and doesn't need to break the P-P bond leading to very stable adsorption of nitrene (Table 2).

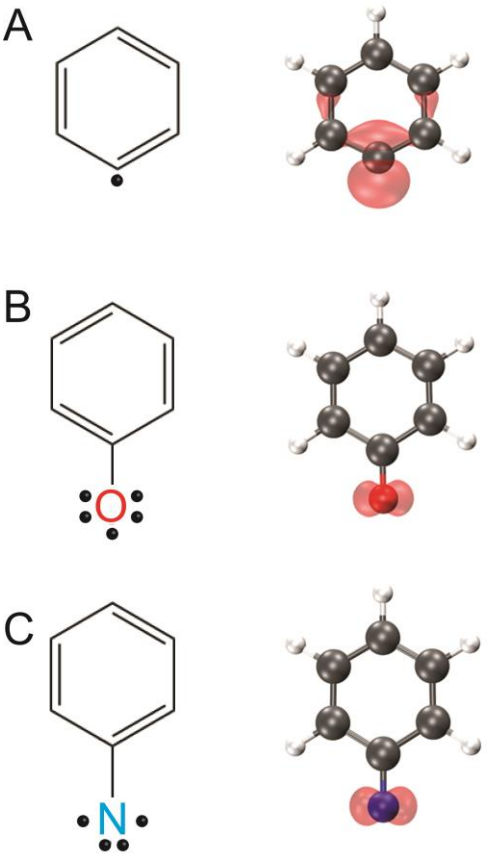

Figure 4. 2 The structure and partial charge densities of (a) phenyl, (b) phenolate, and (c) nitrene. Black, white, red, blue balls denote C, H, O and N atoms, respectively. The SOMO (singly occupied molecule orbital) of phenyl, phenolate and HOMO (highly occupied molecule orbital) are shown on the right panel.

The nature of the dative bond is further supported by analysing the charge transfer at the interface. Fig. 4. 3 shows the calculated charge transfer between nitrene and BP. The lone-paired electrons of P are shared between P and N, leading to charge redistribution at the P-N-C atoms at the interface. The unperturbed band structure of BP upon adsorption of nitrene may suggest that nitrene-derived species could be a desirable functional group to functionalize the BP layers. This hydrophobic functionalization at the surface may help BP to resist fast degradation upon exposure to mainly water, oxygen and light.[196, 197, 213]

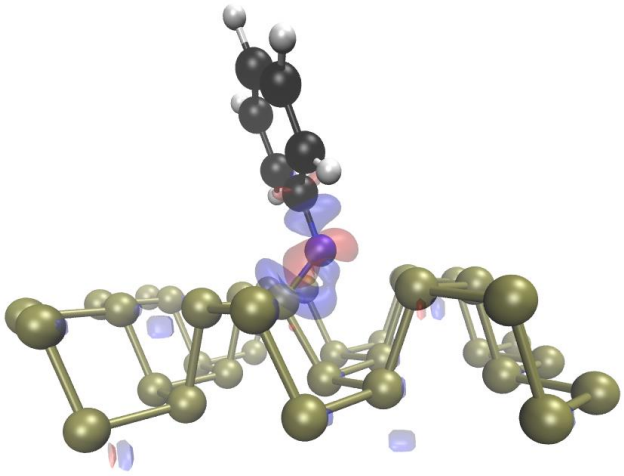

Figure 4. 3 Charge transfer between the nitrene and BP. The red and blue colors indicate electron accumulation and depletion, respectively. The value of isosurface used for plotting the charged density difference is ±0.05 e $Å^{-3}$. The charge density difference Δρ is calculated as Δρ= ρ(nitrene/BP) - ρ(nitrene) - ρ(BP), where the ρ(nitrene/BP), ρ(nitrene), and ρ(BP) are the charge density of nitrene adsorption on BP, isolated nitrene, and isolated BP, respectively, with the atomic positions were also fixed at the optimized adsorption configuration.

Next, to further tune the electronic property of BP, we have modelled functionalization of other nitrene-derived groups on phosphorene substrate, including N-methylbenzene, N-aminobenzene as well as N-nitrobenzene, in which CH_3 and NH_2 are electron-donating groups, while NO_2 is known to be an electron-withdrawing group. Because N is more electronegative than C and than H, CH_3 and NH_2 substituted nitrene groups are able to release electrons to their adjacent parts while N tends to withdraw electrons from ring by inductive effects. Furthermore, N in NO_2-substituted nitrene possesses a positive charge by donating partially its lone pair electrons to one of the O atoms, so it tends to withdraw electrons inside to reduce its positive charge. This charge redistribution at the interface causes a change of the surface dipole[199] resulting in changes of the work function of the material.[224]

We calculated work function of BP functionalized at only one side of the pristine BP as well as at both sides, the latter of which is helpful to reduce dipole interaction resulting from the periodic boundary condition. The calculated electrostatic potential is shown in Fig. B5. Table 3 shows that among the functional groups examined, NO_2-substituted nitrene-BP shows the highest work function compared to either pristine or nitrene-BP. Instead, there is a moderate decrease in the value when nitrene-BP is decorated by NH_2, which is one of the electron-donating groups. The electrostatic potential profile in Fig. 4. 4 also shows a shift of vacuum level when Fermi level is aligned manually, indicating the strong electron-withdrawing power of NO_2. Addition of CH_3 and NH_2 substituted nitrene groups results in reduced work function as compared to nitrene-BP. Therefore, by introducing electron-donating and withdrawing groups into the nitrene groups, we can tune the work function by 2 eV with a rather low coverage of

functional groups (one group per 18 surface P atoms). We find that the work function of BP can be further modified by changing the density of the functional groups, in agreement with literature.[225] For example, double the coverage of the NO_2-substituted nitrene, the work function can be increased by an additional 0.7 eV (Table B. 1).

Table 3 Calculated work function (DFT-PBE) of pristine BP, double-sided functionalized BP and single-sided functionalized BP upon ligation of CH_3, NH_2 and NO_2-substituted nitrene groups, respectively. Work functions are in eV.

Pristine	Nitrene	CH_3	NH_2	NO_2
4.4	4.3	4.2[a]	3.8[a]	5.5[a]
		4.2[b]	3.8[b]	5.8[b]

[a] Calculations with both sides of BP functionalization.

[b] Calculations with functionalization on one side of the BP surface.

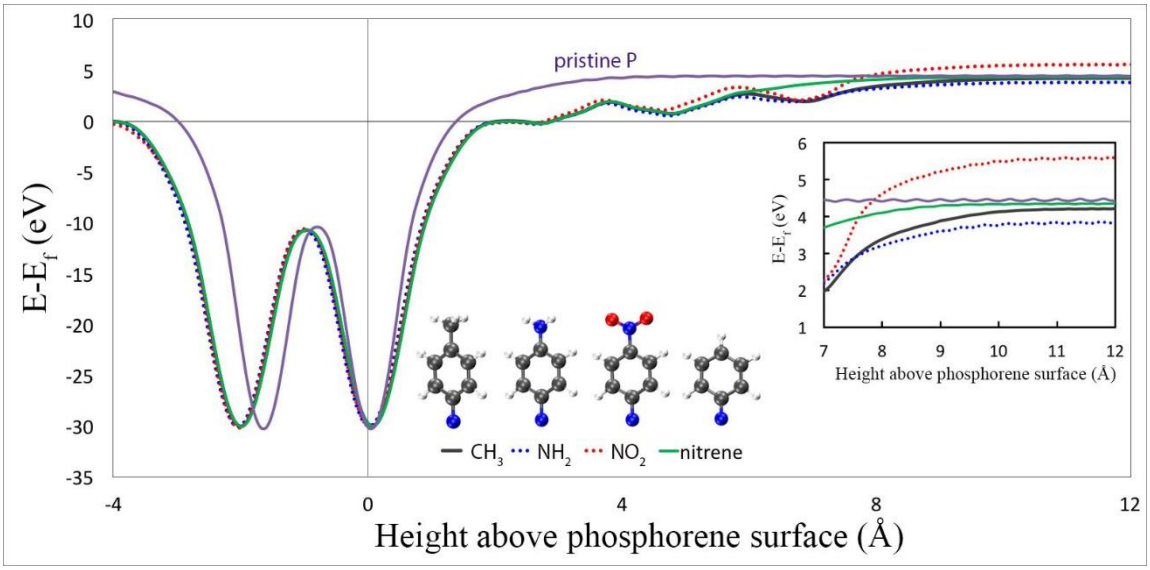

Figure 4. 4 Electrostatic potentials of BP with different functional groups at both sides, including N-methylbenzene-BP (black solid curve), N-aminobenzene-BP (blue dotted), N-nitrobenzene-BP (red dotted). Electrostatic potentials of pristine monolayer BP (purple solid) and nitrene functionalized BP (green solid) are shown to compare. The black, white, red, blue balls denote C, H, O, and N atoms, respectively.

In addition, we calculated charge transfer occurs between the functional group and monolayer black phosphorous by performing Bader change analysis[226] as revealed in Table 4. We find that all functional groups we have covered behave as an accepter, which withdrawals electrons from BP sheet (negative sign denotes the number of electrons that transfer from monolayer to functional groups). And the changes in charge transfer upon functionalization are linearly correlated with the changes in work function.

Table 4 Calculated charge transfer (DFT-PBE) from BP sheet to each ligand. The negative sign indicates donation of electrons from P to the ligands.

	Phenyl	Phenolate	Nitrene	$-CH_3$	$-NH_2$	$-NO_2$
Charge transfer (e^-)	-1.22	-1.13	-1.85	-1.83	-1.81	-1.90

4.1.3.2 Inorganic Lewis Acids

In a separate effort, a few inorganic Lewis acids were introduced on two-dimensional black phosphorus, namely BH_3, $ZnCl_2$, $ZnBr_2$, $AlCl_3$, $AlBr_3$, and $FeCl_3$. These functional groups all present stable interfacial binding with BP through P-M dative

bonds, yet change the semiconducting property of pristine BP. Similarly, the work function of BP can be tuned based on the chemisorption systems (Figure 4. 5). Furthermore, functionalization of BP by $FeCl_3$ introduced magnetic moment into the hybrid system, which could be valuable for single-atom memory. In the case of introducing the acylation ion (CH_3CO^+), which is the key species in the Friedel-Crafts acylation reaction. The acylium ion can in principle be introduced using acetyl chloride (CH_3COCl) as the agent and $AlCl_3$ as a catalyst in an organic solvent.[227] Note $AlCl_3$ can form stable Lewis acid-base pairs on the BP surface as discussed above. The pre-adsorbed $AlCl_3$ can thus react with acetyl chloride producing $AlCl_4^-$ and the acylium ion, the latter of which readily adsorbs on the surface of BP forming an acetyl group, replacing $AlCl_3$ from the surface, due to its large adsorption energy. The acetyl group can also be removed by aromatics such as benzene and methyl furan,[228] which can react with the surface acetyl group by forming carbon–carbon bond. In other words, the surface functionalization using acetyl moieties can be reversed and controlled by reactions. We do notice that this surface functionalization using acetyl groups will be very sensitive to moisture, because water can react with acetyl groups forming acetic acid. Similarly, we can use $ZnCl_2$ as the catalyst for the Friedel-Crafts acylation reaction.[227]

Importantly, the tunable work function and band edge energies are valuable for building heterostructures between BP and other two-dimensional materials[229] as well as metal oxides[230]. It is also desirable to tune the band edges for applications in electrocatalysis,[231] in which the energy of the conduction and valence band edges should be aligned with the electrochemical potentials of the redox reactions. In addition, functionalization of the BP using the hydrophobic nitrene groups may also help to reduce

contact between BP and water, since it has shown that O_2 dissolved in water may cause decomposition of the BP layers.[196]

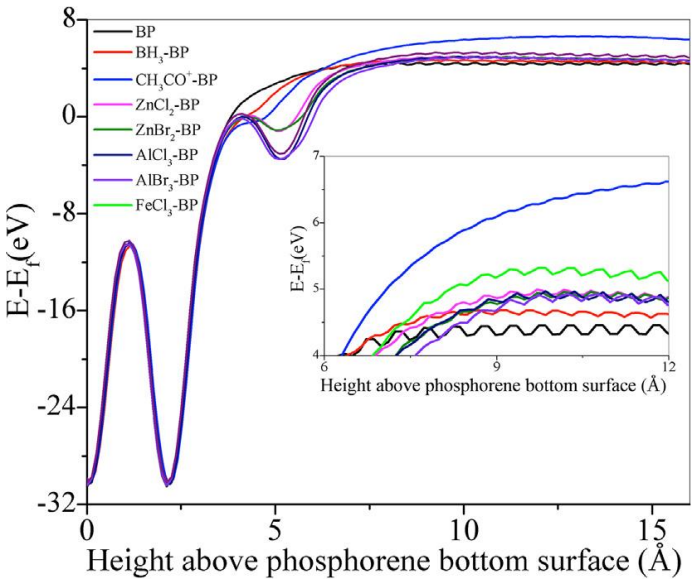

Figure 4. 5 Calculated electrostatic potentials (E) of monolayer BP modified by different Lewis acids. The inset shows the electrostatic potentials in the vacuum to compare. The Fermi level is set to zero.

4.1.4 Conclusions

We have systematically investigated the adsorption of phenyl, phenolate, nitrene, and a few inorganic Lewis acids on the basal plane of black phosphorus by means of DFT computations. We find that nitrene, BH_3, $ZnCl_2$, $ZnBr_2$, $AlCl_3$, $AlBr_3$, and $FeCl_3$ are desirable functional groups for surface modification of black phosphorus because they show very strong thermo stability and do not perturb the electronic structures due to the interfacial dative bonds. In addition, functionalization of black phosphorus via Lewis acids can be further used to tune the work function. The results reported here indicate that one can tune the substituent groups in the phenyl, phenolate and nitrene moieties to tune

the charge transfer at the interface, through which a tunable electronic structure of black phosphorus may be achieved. The great tunability of the electronic properties of black phosphorus by covalent functionalization suggests an effective way to realize its full potential in nanoelectronic and optoelectronic applications.

Appendix B contains PDOS of the functional groups using the DFT-PBE functional, band structure of pristine and nitrene-functionalized BP, electrostatic potentials of BP functionalized with nitrene-derived moieties, calculated work function change at different coverage of the functional moieties.

4.2 Photoresponse of Natural van der Waals Heterostructures

4.2.1 Introduction

Van der Waals (vdW) heterostructures consisting of two-dimensional (2D) materials such as graphene, transition metal dichalcogenides, and hexagonal boron nitride have gained tremendous attention recently owing to novel electronic states and applications that may be realized in these vertical heterostructures.[232-234] Research on 2D van der Waals heterostructures (vdWH) has so far been focused on layer by layer stacking of these 2D materials in the laboratory, forming synthetic heterostructure.[232, 235] This artificial fabrication of vdWH also has major limitations: first, there is little control over crystal orientation while stacking on top of each other; and second, the sample can suffer damage by unwanted air bubbles or adsorbates between the stacked layers. Recently Molina-Mendoza et al. and Velický et al. independently pioneered an exfoliation of a naturally occurring mineral, franckeite, into few-layer-thick

heterostructures that are composed of alternating sequences of weakly bound stacked PbS and SnS_2 layers attached by van der Waals interactions.[236, 237] Hence, franckeite can be considered as a naturally occurring vdWH analogue of its synthetic cousin. Molina-Mendoza et al. have demonstrated photoresponse properties and p−n photodiode behavior of few-layer franckeite (405 nm < λ < 940 nm) at room temperature.[236] Velický et al. have demonstrated excellent electrochemical properties of franckeite that can be utilized in energy conversion and energy storage applications.[237, 238]

4.2.2 Sample Fabrication

The flakes of franckeite examined in this study were microexfoliated from a crust of franckeite crystals originating from San Jose, Bolivia. First, we fabricated the metal electrodes on a glass substrate using optical lithography followed by thermal evaporation of Cr/Au[239] (5 nm/100 nm). In parallel, we prepared a PDMS (poly (dimethylsiloxane)) stamp[240] structure on a microscope slide. The franckeite was exfoliated onto the PDMS stamp followed by characterization using optical microscopy, Raman spectroscopy, and atomic force microscopy to verify the franckeite deposition and determine the sample thickness. We found that the sample thickness varies from 60 to 100 nm. We aligned the exfoliated franckeite flake on the polymer stack with the prepatterned metal electrode target under a microscope and brought it into contact. The polymer layer was mechanically separated from the PDMS stacks.

4.2.3 Computational Methods

Density functional theory calculations were performed using the VASP package.[241] The PBE (Perdew-Burke-Ernzerhof) exchange-correlation potential[124] was used, and the electron−core interactions were treated with the projector augmented wave (PAW) method.[242, 243] The van der Waals interaction has been taken into account through the DFT-D3 semiempirical methods.[137, 179] The calculations have been performed using a franckeite unit cell taken from an experimental measurement with the lattice constants a = 5.805 Å, b = 5.856 Å, and c = 17.338 Å.[244] The Brillouin zone of the bulk franckeite was sampled using a (6 × 6 × 2) *k*-point with a kinetic cutoff energy of 400 eV. For the HQ and HQH layers, a (6 × 6 × 1) *k*-point was used for the calculations of optical absorption. The atomic structures were visualized using the VESTA software.[245] Calculations including spin−orbit interaction have been performed as well, which show only minor changes in the electronic structures (Figure B. 7 and Figure B. 8 in appendix B). Therefore, all the calculations reported here were performed without including spin−orbit interactions. It is known that misfit-induced corrugation may exist in franckeite materials.[236, 237] Such a long-range corrugation may cause inhomogeneous electronic structure at the interface[246, 247] and was not taken into account in the periodic calculations reported here.

4.2.4 Results and Discussion

We have presented schematically the crystal structure of the layered materials in Figure 4.5. The mixed-metal sulfide franckeite is a complex layered crystal that is composed of lead, tin, antimony, iron, and sulfur. Franckeite is formed by alternating

stacking of a pseudohexagonal (H) layer, e.g., tin disulfide (SnS_2), and pseudotetragonal (Q) layers, e.g., lead sulfide-based (PbS) layers.[244] The complex Q layers contain four atomic layers of sulfide compounds with the formula MX, where M = Sn^{2+}, Pb^{2+}, or Sb^{2+} and X = S. The H layer is a simple binary layer and consists of octahedra of disulfide compounds with the formula MX_2, where M = Sn^{4+} and Fe^{2+} and X = S.

Franckeite has interesting and complex electronic band structure.[236, 237] The band gap of the metal sulfides that are the basic ingredients of the franckeite layered structures ranges from 0.37 eV in PbS to 2.1 eV in SnS_2,[248] with franckeite itself having an effective infrared band gap of 0.65 eV.[236, 237, 249] Hence franckeite provides an ideal platform to study band gap engineering,[250] optoelectronics, phase engineering,[251] and thermoelectric properties[252] in a complex layered natural vdWH.

Here we present a detailed study of intrinsic optoelectronic behavior of the thin franckeite (60 nm < d <100 nm) by measuring the photoresponsivity of the thin film. Moreover, we have calculated the electronic band structure and the imaginary component of the dielectric constant via density functional theory (DFT) and obtained close agreement. Our study reveals fundamental optoelectronic properties of franckeite and may lead the way to develop nanoscale optoelectronic devices with tailored properties.

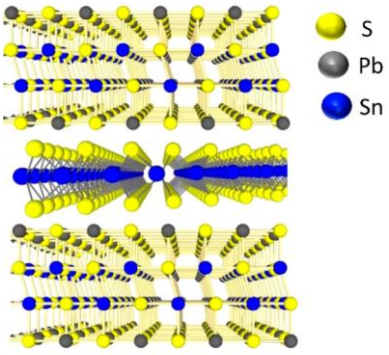

Figure 4. 6 Crystal structure of franckeite: the top and bottom layers are Q layers that includes MX compounds, where M = Sn^{2+} or Pb^{2+} (M can also be Sb^{3+} instead of Sn^{2+}) and X = S. The middle layer, or H layer, includes MX_2, where M = Sn^{4+} (M can also be Fe^{2+} instead of Sn^{4+}) and X = S.

We measured the photoresponsivity of the sample, which is defined as $R = I_{ph}/P_{light}$, where I_{ph} is the measured photocurrent and P_{light} is the power of the incident light. Photoresponsivity is an important figure of merit for a photodetector.[239] The photoresponsivity data recorded at 77 K are shown in Figure 4. 6. We have observed the maximum photoresponsivity of 0.3 mA/W at ~750 nm at 77 K. At room temperature the photoresponsivity is increased to 20 mA/W, corresponding to an external quantum efficiency EQE ≈ 3%, which is very promising for franckeite-based photonic device applications.

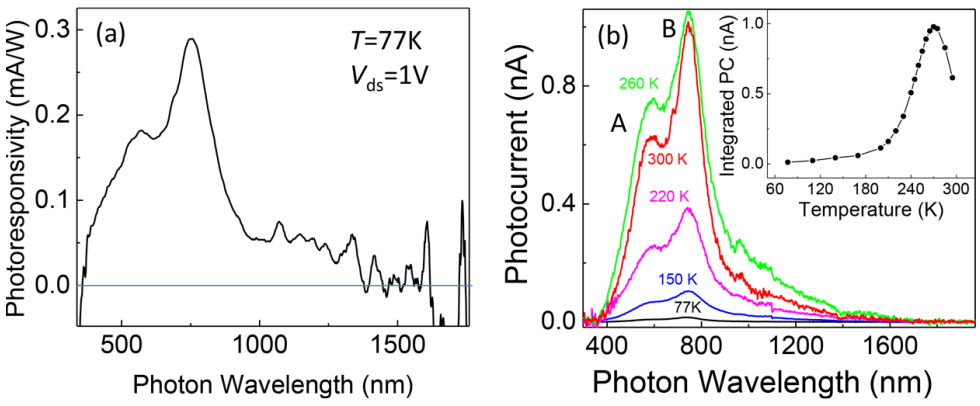

Figure 4. 7 Optoelectronic properties of a franckeite thin film. (a) Photoresponsivity spectrum of a franckeite device for a drain-source voltage (V_{ds}) of 1 V measured at 77 K. The photocurrent (PC) was normalized using a calibrated Si photodetector. The

photocurrent is diminishing at ~1450 nm, indicating an effective band gap of ~830 meV. (b) PC spectra for different temperatures. The PC magnitude increases as we increase the temperature until ~260 K and then decreases again. The inset presents the integrated PC data as a function of the temperature showing the transition temperature of ~260 K. The photocurrent integration was conducted between 400 and 800 nm. The overall shape of the PC spectrum remains the same.

The PC spectra for different temperatures are presented in Figure 4. 6(b). We note three important features: (i) there are two peaks at 600 and 750 nm; (ii) the PC signal diminishes around 1500 nm; and (iii) the PC spectra are very broad. The cutoff at 1500 nm originates from the band edge, which confirms the narrow band gap of franckeite (Eg ≈ 830 meV). The energy of the two peaks, ~590 nm (~2.1 eV) and ~740 nm (~1.66 eV), match the optical band gaps of SnS_2 and Sb_2S_3, respectively.[248] It is interesting to note that the photoresponse behavior of franckeite is dominated by Sb_2S_3.

To understand the origin of these peaks in the PC, we performed DFT calculations to determine the electronic structures of the franckeite material and to calculate the optical absorption properties. Figure 4. 7(a) shows the calculated band structure of the unit cell of bulk franckeite, which contains four Pb, six Sn, and twelve S atoms. The bulk franckeite shows a finite density of states at the Fermi energy, and there is a finite energy gap within the conduction band, which agrees with a recent calculation.[236] The frequency-dependent dielectric function is calculated by a summation over empty states and is plotted in Figure 4. 7(b) and (c). In addition, isolated H, Q, HQ, and HQH have been calculated for comparison. There is one major peak in Figure 4. 7(b) at short

wavelengths, which is very similar to the sum over the individual H and Q layers (dashed black line in Figure 4. 7(b). However, at the longer wavelengths (above 800 nm), the difference between the bulk franckeite and the sum over H and Q becomes more significant, indicating that optical transitions between these two materials at the interface may start to dominate. The long tail at the infrared wavelength in the calculated spectrum results from the excitation of electrons at the Fermi level to the empty states in the proximity of the Fermi level. It should be noted that the calculated main peak is blue-shifted as compared to the photocurrent measurement (Figure 4. 6). This difference may result from the complicated distribution of the Pb and Sn atoms in the Q layer. However, Figure 4 .8 shows the calculated imaginary part of the dielectric function with Pb and Sn distributed in the Q layer with varied stacking configurations, and these spectra look very similar. Another possibility is the impurities in the franckeite materials, as shown in the literature.[244] In addition, it remains to be studied how the Coulombic interaction between the excited electrons and holes will affect the optical spectrum calculations, since this interaction has not been included in the current calculations.

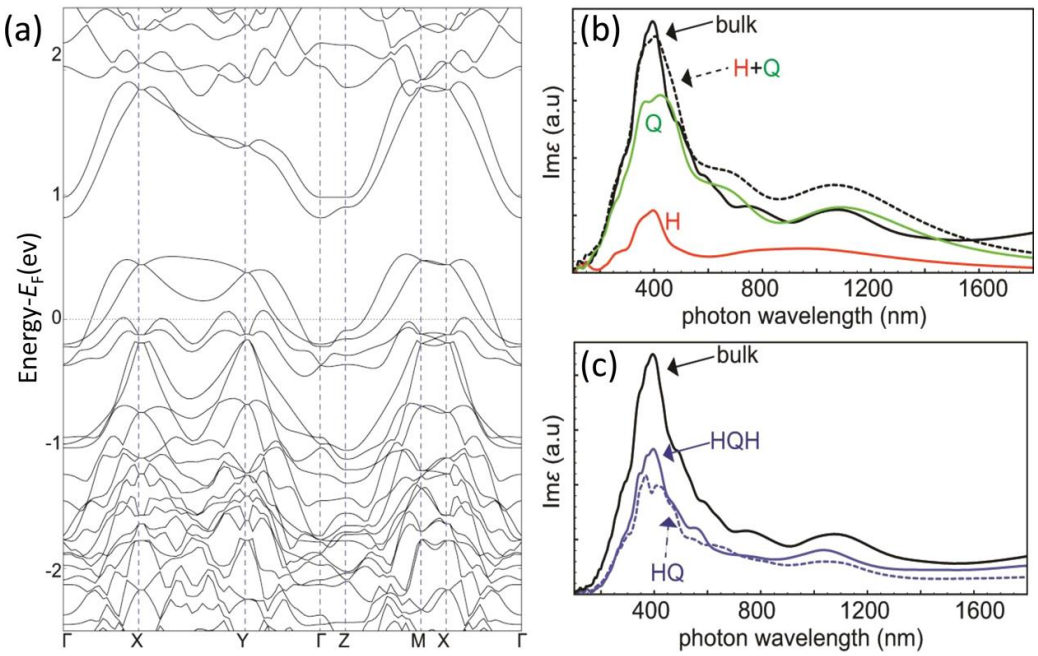

Figure 4. 8 Calculation of the optical absorption properties of franckeite. (a) DFT-calculated band structure of the franckeite bulk material. (b) Imaginary part of the dielectric function of an isolated H or Q layer as compared with the bulk franckeite. The dashed black line shows the sum over H and Q values. (c) Imaginary part of the dielectric function for the HQ bilayer (blue dashed) and HQH trilayer (blue solid) as compared with the bulk franckeite.

Our DFT calculation produces similar results to those published by Velický et al. and Molina-Mendoza et al.,[236, 237] particularly to the latter work. Although Velickýet al. employed supercell calculations, the key features of the electronic structure are very similar.

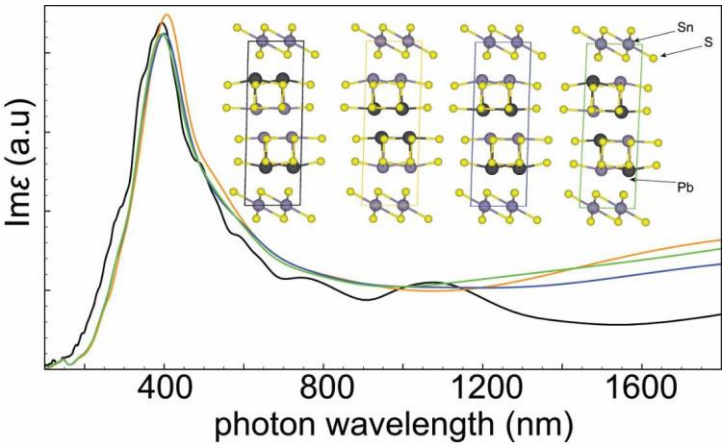

Figure 4. 9 DFT-PBE calculated imaginary part of the dielectric function of the franckeite bulk structure with varied stacking (insets) in the Q layer.

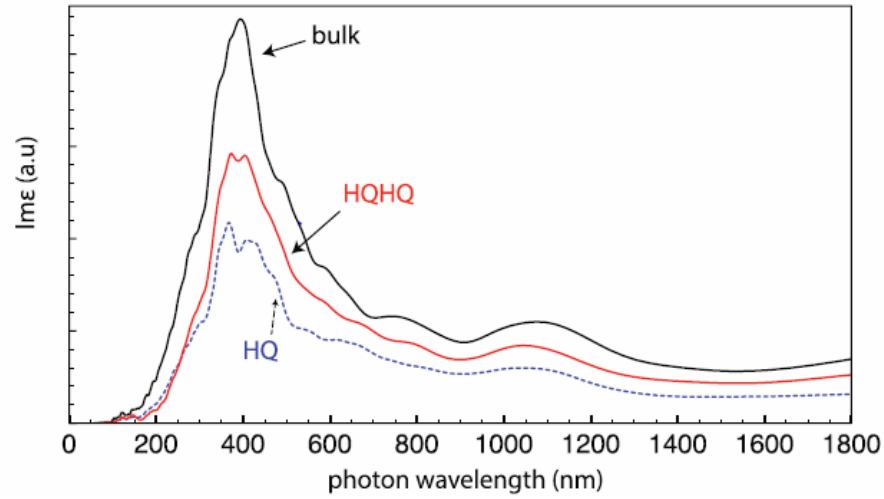

Figure 4. 10 Calculation of the optical absorption properties of franckeite. The imaginary part of the dielectric function of HQHQ layer (red solid) and HQ layer (blue dashed) as compared with the bulk franckeite (solid black).

To understand the effect of the number of layers on the physical properties of franckeite, we calculated optical absorption for monolayer (HQ), bilayer (HQHQ), and

bulk samples. We find that the position and shape of the main absorption peak do not vary when changing the numbers of layers (Figure 4. 9). On the basis of the Raman and DFT calculations, Velický et al. also suggested that the electronic and structural properties of franckeite do not depend on the number of layers.[237]

4.2.5 Conclusions

We present the optoelectronic behavior of thin natural vdWH franckeite, which demonstrates a narrow band gap semiconductor with a cutoff at ~1500 nm and a broad photoresponse from the UV to the infrared regime. By calculating the electronic band structure via DFT, we showed the optical absorption properties, which are in agreement with the measured PC spectrum qualitatively. The devices demonstrate efficient photoresponse with external quantum efficiency EQE ≈ 3%. Our study sheds light on the optoelectronic behavior of franckeite, a naturally occurring complex van der Waals heterostructure, advances the fundamental understanding of its optoelectronic behaviors, and can lead to the development of nanoscale optoelectronic devices with tailored properties.

Appendix B contains DFT calculations including spin-orbit coupling.

Chapter 5 Reaction Kinetics of Cyclohexene Hydrogenation over Pd/α-Al_2O_3

5.1 Introduction

Hydrogenation of cyclohexene serves as a model reaction in heterogenous catalysis for the determination of catalyst activity. Cyclohexene hydrogenation to cyclohexane has been studied in both gas and liquid phase over supported metal catalysts.[253-260] The effect of solvent over supported Pd[255] has been revealed, that is, the reaction rate is independent of inert solvents under reaction temperature of 264-308 K and 4-89 kPa hydrogen partial pressure with atmospheric total pressure. The reaction orders under these reaction conditions was found to be 0.5^{th} order with respect to hydrogen and 0^{th} order based on cyclohexene. However, the reaction kinetics and the possible solvent effects in much wider range of H_2 pressure at higher temperature has not been investigated.

Kinetic modeling, in combination with computational surface science based on density functional theory (DFT) calculations have evolved in recent decades to provide insights in surface chemical reactions. An accurate kinetic model not only describes experimental phenomena mathematically, fulfills predictions for wider range of process conditions, but also provides valuable information for theoretical calculations. On the other hand, theoretical calculations provide detailed atomic-level understanding of various reaction pathways and adsorption behavior of key intermediates, which to some extents provide experimental guidance and verification. Hereby, liquid phase cyclohexene hydrogenation has been carried out in three inert nonpolar solvents under

wide range of H_2 pressure over 0.25 wt.% Pd/α-Al_2O_3. The reaction kinetics revealed that hydrogen dissociatively adsorbs on different active sites with reactant or solvents. DFT calculations of cyclohexene hydrogenation were performed on the Pd (111) surface. It was demonstrated that the rate determining step is the first hydrogenation step, which agrees with the experimental kinetic study that the reaction is 0.5^{th} order with respect to H_2 pressure. The kinetic fittings were then conducted to obtain the equilibrium constants and rate constants in order to present a systematic picture of reaction kinetics including the reactant adsorption, surface reaction, and product desorption processes. Furthermore, thermodynamic and kinetic properties such as entropy change and enthalpy change during reaction and activation are interpreted. Theoretical calculations show that H prefers to stay on a three-fold fcc hollow site, while cyclohexene is found to be stable on the top site (by forming π bond) and bridge site (by forming di-σ bond). Also, DFT calculations predict that the heat of adsorption and reaction activation energy are coverage dependent. Also, reactions taking place on the β-phase PdH (111) surface presents the most comparable energy barrier of 80 kJ/mol to kinetic fittings, which demonstrates the fact that β-phase PdH could form under experimental conditions.

5.2 Experimental Methods

The liquid-phase cyclohexene hydrogenation was carried out in the 300 mL high temperature and high pressure Parr batch reactor equipped with IR probe (Mettler Toledo ReactIR iC 10) for in-situ spectroscopic investigations[261]. Aprotic inert solvents used in the study were heptane, (Sigma-Aldrich, anhydrous, 99%) methylcyclohexane (Sigma-Aldrich, anhydrous, ≥99%), and decalin (Sigma-Aldrich, anhydrous, ≥99%). The reactant

cyclohexene (Sigma-Aldrich, BHT as inhibitor, ≥99%) was first distillated in N_2 flow at 50°C to separate the inhibitor BHT. The distillated cyclohexene was then filtered through a column packed with γ-Al_2O_3 (Alfa Aesar) to remove the trace amount of other impurities that may cause serious catalyst deactivation during reaction. The purified cyclohexene was stored in a freezer when not being used. Certain amount of catalyst 0.25 wt.% Pd/α-Al_2O_3 and 100 mL solvent were initially charged into the reactor vessel. Catalyst was reduced in excess hydrogen at 100°C[262] for an hour. 20 mL of reactant feed containing cyclohexene was pressurized in the reactor vessel to the desired pressure at the reaction temperature ranging from 40°C to 100°C. The reaction pressure was varied widely from 35 psi to 600 psi. For co-solvent mixture, the second solvent was added along with the catalyst at the beginning of the reduction.

The IR probe allows the in-situ quantification of liquid phase cyclohexene hydrogenation. Before the reactant injection, the probe scanned and subtracted the background. When the reactant feed was purged in the vessel, the reaction started. The scan took place every minute. The characteristic IR absorption frequencies of 1139 cm^{-1} (ωCH_2 rock) and 719 cm^{-1} (C-H out-of-plane bending)[263] on the acquired IR spectrum were utilized for quantifications due to the uniqueness that they only appeared in cyclohexene. By plotting the cyclohexene concentration change as the function of time, hydrogenation reaction rate was achieved by measuring the slope of the reaction IR profile.

After reaction, the liquid phase was analyzed by 7890B Agilent GC-FID equipped with ZB-5 GC column. The conversion calculated from GC results were compared with

IR results for consistency. Meanwhile, the carbon balance was verified to validate the IR results.

Conversion is defined by the following equation:

$$Conversion\ x\% = \frac{mole\ of\ reactant\ reacted}{mole\ of\ reactant\ fed} \times 100\% \quad (1)$$

5.3 Computational Methods

The density functional theory calculations were carried out using the Vienna Ab initio simulation package (VASP)[176]. The Perdew-Burke-Ernzerhof generalized gradient approximation exchange-correlation potential (PBE-GGA)[177] was used, and the electron-core interactions were treated in the projector augmented wave (PAW)[178] method. The van der Waals interactions were included through the Grimme's DFT-D3 semiempirical method.[216, 217] Structures were optimized with a kinetic cutoff energy of 400 eV and relaxed until the force acts on each atom is smaller than 0.02 eV $Å^{-1}$.

The Pd metal surface was modeled with a 4 × 4 unit cell with four (111) atomic layers. Similarly, H-terminated PdH surface was also modeled using a four layer 4 × 4 surface slab. The bottom two layers of Pd and PdH surfaces were frozen to keep the bulk configurations. The computed bulk lattice constants are 3.885 Å for Pd and 4.075 Å for PdH. The vacuum between the slabs was set at 20 Å to minimize the effect of the interaction between adjacent supercells. The Brillouin zone was sampled with a 3 × 3 × 1 *k*−point grid throughout all the calculations.

Transition state searches were performed using the dimer method[143] with the initial guesses for the transition state structure obtained through the nudged elastic band

(NEB) method.[142] The transition states were confirmed with the presence of a unique imaginary frequency in the vibration frequency calculations.

The adsorption energy was calculated as $E_{ads} = (E_{ni/slab} - E_{slab} - nE_i) / n_i$, where $E_{ni/slab}$, E_{slab}, and E_i are the total electronic energy of the adsorbate/slab system, the clean metal slab, and the isolated adsorbate in the gas phase, respectively. n denotes the number of adsorbates on the metal slab. Stronger adsorption is quantified by more negative numerical adsorption energy values.

5.4 Results and Discussion

5.4.1 Pd particle distribution and surface structure

The TEM images of 0.25 wt.% Pd/α-Al_2O_3 is presented in Appendix C Figure C. 1. The HRTEM image on surface Pd clusters illustrates the crystal structure. The empirical Pd atomic radii is 1.40 Å[264], and therefore the spacing for (111), (110), (100), are theoretically 2.29 Å, 2.80 Å and 3.96 Å respectively. The average distance measured in TEM images is 2.35 Å, which is closer to 2.29 Å. Therefore, the surface Pd clusters of 0.25 wt.% Pd/α-Al_2O_3 is composed of mostly (111) facets and the theoretical calculations utilized the closed-packed Pd (111) to model the catalyst.

5.4.2 Catalyst deactivation and kinetic regime

The catalyst deactivation was evaluated first before the kinetic measurement. Reactions express slight deactivation after 20 min of reaction time (Appendix Figure C. 2). Therefore, the kinetic hydrogenation rate has been measured only by applying the first 20 min IR profile when the catalyst hasn't been deactivated.

In order to acquire the true kinetic rate, mass transfer tests were carried out to assure the reaction conditions were free of transfer limitations. The mass transfers in the liquid phase reaction can be categorized as gas to liquid, liquid bulk to catalyst surface and catalyst surface reactants diffusion to internal pores. The catalyst support chosen in the study is non-porous α-Al_2O_3 with only 0.012 cm^3/g pore volumes measured by N_2 physisorption. Pd metal particles only covers the support surface, therefore the internal mass transfer can be excluded. The external mass transfer tests are done by changing the stirring speed of the reaction. Additionally, H_2 transfer test from gas phase to liquid are carried out by changing the amount of catalysts. The mass transfer tests are concluded in the Appendix Figure C. 3. Under the conditions of 70°C 560 psi of H_2 and 500 rpm, cyclohexene hydrogenation is free from transfer limitations.

5.4.3 Kinetic models

The cyclohexene hydrogenation in three aprotic inert solvents were investigated. Under kinetic regime, the reaction rate differs when changing operating conditions. The Langmuir-Hinshelwood kinetic approach is employed to model the reaction kinetics. The approach describes cyclohexene hydrogenation in the sequence which includes the crucial steps as surface adsorption, surface reaction and surface desorption. The mechanism is presented as follow:

$$H_2^g \leftrightarrow H_2^l \tag{2}$$

$$H_2^l + 2S \overset{K_{H_2}}{\longleftrightarrow} 2HS \tag{3}$$

$$E + S \overset{K_E}{\leftrightarrow} ES \tag{4}$$

$$ES + HS \overset{k_3}{\rightarrow} EHS + S \quad (5)$$

$$EHS + HS \overset{k_4}{\rightarrow} AS + S \quad (6)$$

$$AS \overset{K_A}{\leftrightarrow} A + S \quad (7)$$

$$Solvent + S \overset{K_S}{\leftrightarrow} SolventS \quad (8)$$

The sites balance could be derived using surface coverage, θ. There are two types of site balance depending on the assumptions; one gives the site balance where all species adsorb on the same site as[265]

$$1 = \theta_v + \theta_{HS} + \theta_{ES} + \theta_{EHS} + \theta_{AS} + \theta_{SolventS} \quad (9)$$

The other separates the sites where reacting species and solvent adsorb on same site, yet H_2 adsorbs on different sites as,[266, 267]

$$1 = \theta_{v1} + \theta_{HS1} \quad (10)$$

$$1 = \theta_{v2} + \theta_{ES2} + \theta_{EHS2} + \theta_{AS2} + \theta_{SolventS2} \quad (11)$$

The surface reaction is the rate determining step (RDS) and other steps are in quasi-equilibrium. However, depending on whichever step rate-determing, one of the two surface hydrogenation steps becomes irreversible. Furthermore, much smaller H_2 atoms could alternatively be adsorbed on the high-coordinated three-fold fcc sites[268-271] without competing atop with other surface reacting species and solvents. Therefore, the possible kinetic models for the liquid-phase cyclohexene hydrogenation consist of four combinations (Table 5)

Table 5 Kinetic models and reaction orders

	H_2 adsorption site	RDS	Rate	Reaction order			
				Low P_{H2}	High P_{H2}	Low a_E	High a_E
1	Same site	1st H	$r = \frac{k_3 K_E a_E \sqrt{P_{H_2} K_{H_2}}}{(1 + \sqrt{P_{H_2} K_{H_2}} + K_s a_s + K_E a_E)^2}$	0.5	-0.5	1	-1
2	Same site	2nd H	$r = \frac{k_4 K_{E*} K_E a_E (P_{H_2} K_{H_2})}{(1 + K_E a_E + K_s a_s + \sqrt{P_{H_2} K_{H_2}} + K_{E*} K_E a_E \sqrt{P_{H_2} K_{H_2}})^2}$	1	0	1	-1
3	Different site	1st H	$r = \frac{k_3 K_E a_E \sqrt{P_{H_2} K_{H_2}}}{(1 + K_E a_E + K_s a_s)(1 + \sqrt{P_{H_2} K_{H_2}})}$	0.5	0	1	0
4	Different site	2nd H	$r = \frac{k_4 K_{E*2} K_E a_E (P_{H_2} K_{H_2})}{(1 + K_E a_E + K_s a_s + K_{E*2} K_E a_E \sqrt{P_{H_2} K_{H_2}})(1 + \sqrt{P_{H_2} K_{H_2}})}$	1	0	1	0

Among the four different scenarios, there is only one circumstance that reflects the true kinetic of the surface reaction. According to Figure 5. 1 and Figure 5. 2, the H_2 reaction order at low pressure which ranges from 0 psi to 5 psi is found to be the 0.4^{th} order. The reaction order decreases with H_2 pressure and reaches 0^{th} order in all solvents under high H_2 pressure. In the case of the reaction order on cyclohexene, under low concentration yet high H_2 pressure, the model illustrates the 0.7^{th}, 0.9^{th} and 1^{th} order based on reactions in heptane, methylcyclohexane, and decalin respectively. The reaction order approaches to the 0^{th} order as cyclohexene concentration increases in three solvents. The reaction orders acquired from kinetic model is consistent with Gonzo and Boudart's kinetic studies[255] on cyclohexene hydrogenation. The kinetic analysis unveils that the third scenario in Table 5 is the true kinetic on the Pd catalyst surface, that is, H_2 adsorbs on different sites with the reactant or solvents, and the first hydrogenation is the rate determining step. The results are consistent with liquid phase hydrogenation of benzene over Pd[272].

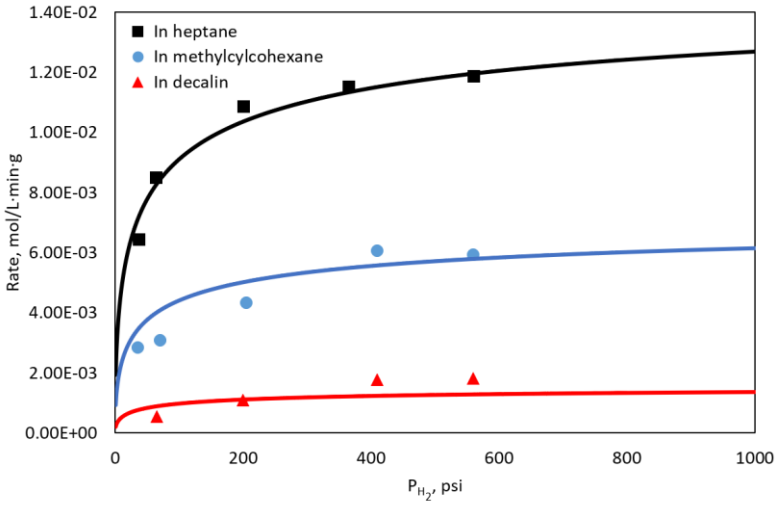

Figure 5. 1 Hydrogenation as a function of H_2 pressure in three solvents fitted with the third scenario where hydrogen and reactant adsorb on different sites and the RDS is the first hydrogenation. Reaction conditions: temperature 70°C, cyclohexene initial concentration 0.42M.

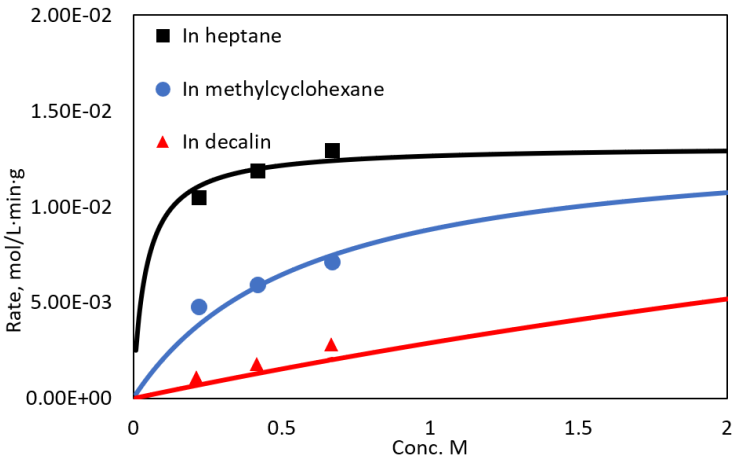

Figure 5. 2 Hydrogenation as a function of cyclohexene concentration in three solvents fitted with the third scenario where hydrogen and reactant adsorb on different sites and the RDS is the first hydrogenation. Reaction conditions: temperature 70°C, H_2 pressure 560 psi.

5.4.4 Kinetic and thermodynamic parameters from kinetic fittings

Thermodynamic parameters such as entropy and enthalpy change during adsorption and reaction are readily fitted with kinetic modelling. The experimental data of cyclohexene hydrogenation were collected under different temperatures ranging from 40 °C to 100 °C with the H_2 pressures of 600 psi and 100 psi in heptane. Therefore, the rate expression is simplified as:

$$r = k_3 \times \frac{K_E a_E}{1 + K_E a_E} \times \frac{\sqrt{P_{H_2} K_{H_2}}}{1 + \sqrt{P_{H_2} K_{H_2}}} \tag{12}$$

The rate constant k_3 and adsorption equilibrium constant K'_i can be derived from the transition state theory[273] and Van't Hoff equaion:

$$k_3 = N_s \frac{k_B T}{h} e^{\frac{\Delta S^{\ddagger}}{R}} e^{-\frac{\Delta H^{\ddagger}}{RT}} \tag{13}$$

$$K'_i = e^{\frac{\Delta S_{ads}}{R}} e^{-\frac{\Delta H_{ads}}{RT}} \tag{14}$$

Eight fitting parameters including ΔS of reaction/activation, and ΔH of reaction/activation are solved with experimental measurements under different temperatures, pressures and reactant concentrations. The data fits well with the kinetic model as shown in the Appendix Figure C. 4. As ΔS varies during mathematical fitting, the ΔH also produces corresponding values to match experimental data. The fitting parameters and their standard deviations are presented in the Table C. 2.

5.5 DFT Calculations of Hydrogenation on Pd (111) surface

Learning from a previous study from G. Watson et.al who found adsorption energies of H on Palladium (111) closely follow the coordination number of hydrogen atom with 3-fold sits the most stable and 1-fold (atop) the least stable,[271] We calculated H

adsorption energy on fcc hollow sites of Pd (111) surface. Later, DFT calculations for H adsorption energy on fcc hollow sites at various H coverages were performed. Considering 16 H atoms on metal slab as 1ML coverage, as shown in Figure 5. 3, H adsorption energy decreases as a function of surface coverage (the number of hydrogen atoms on the surface), showing a linear relationship. On clean Pd (111) surface, the adsorption energy varies from -60 kJ/mol to -53 kJ/mol with increasing H coverage. The fitting parameter α is 7 kJ/mol, which is consistent with the fitting from kinetic measurements. The adsorption of cyclohexene has been calculated on the clean Pd (111) surface with six adsorption conformations: 4 di-σ (bridge) and 2 π adsorption modes (atop). The results in Figure 5. 4 indicates that π-B mode is the most stable confirmation with an adsorption energy of 137 kJ/mol. Cyclohexene atop adsorption sites are different from hydrogen FCC hollow sites, because the latter involves three Pt atoms for binding. Therefore, both surface species don't compete sites with each other.

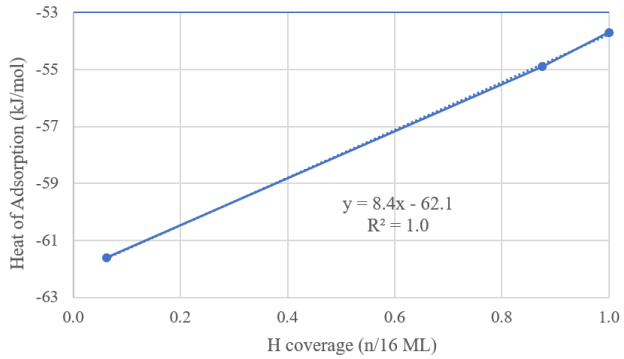

Figure 5. 3 H adsorption energy (kJ/mol) as a function of its own coverage. n represents the number of hydrogen atoms on Pd (111) surface. The maximum value of n is 16.

Moreover, the adsorption of cyclohexene is also influenced by surface coverage of H, as shown in Table 6. For cyclohexene adsorption energy, as shown in Figure 5. 4, the DFT calculations reveal -127 kJ/mol with a single cyclohexene on clean Pd (111). With increasing H coverage, a cyclohexene molecule adsorption strength drops significantly due to strong repulsive interactions between cyclohexene and surface hydrogen. Although π-B mode still remains to be the most stable conformation (Figure 5. 5). This trend can also be seen in the increase of H-Pd length, that more H atoms, especially the two adsorbed hydrogens that are very close to cyclohexene significantly lift the molecule away from surface, giving the fact that cyclohexene and H repel each other.

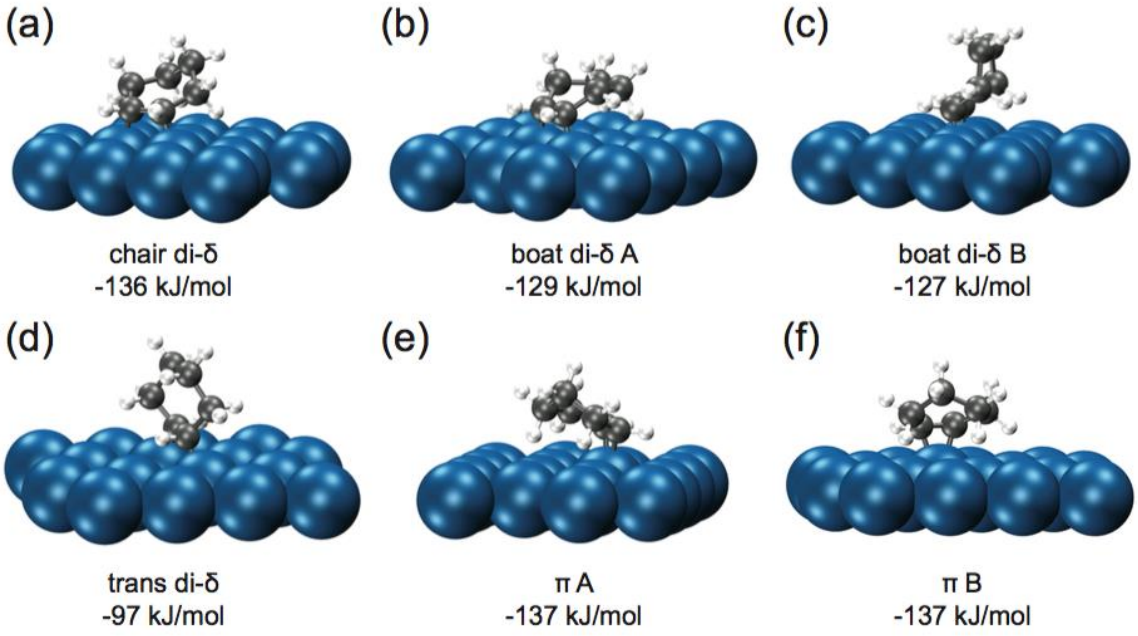

Figure 5. 4 Adsorption structure from side view and energy of cyclohexene on clean Pd (111) surface. The atom colors are Pd in blue, C in gray, and H in white.

Table 6 Adsorption energies of H and cyclohexene on different surfaces.

Property	clean Pd(111)	Pd(111) (θ_H=0.875)	PdH(111) (θ_H=0.875)
H adsorption energy (kJ/mol)	-62	-55	-37
CC (C adsorption mode) adsorption energy[a] (kJ/mol)	-127	-65	-12

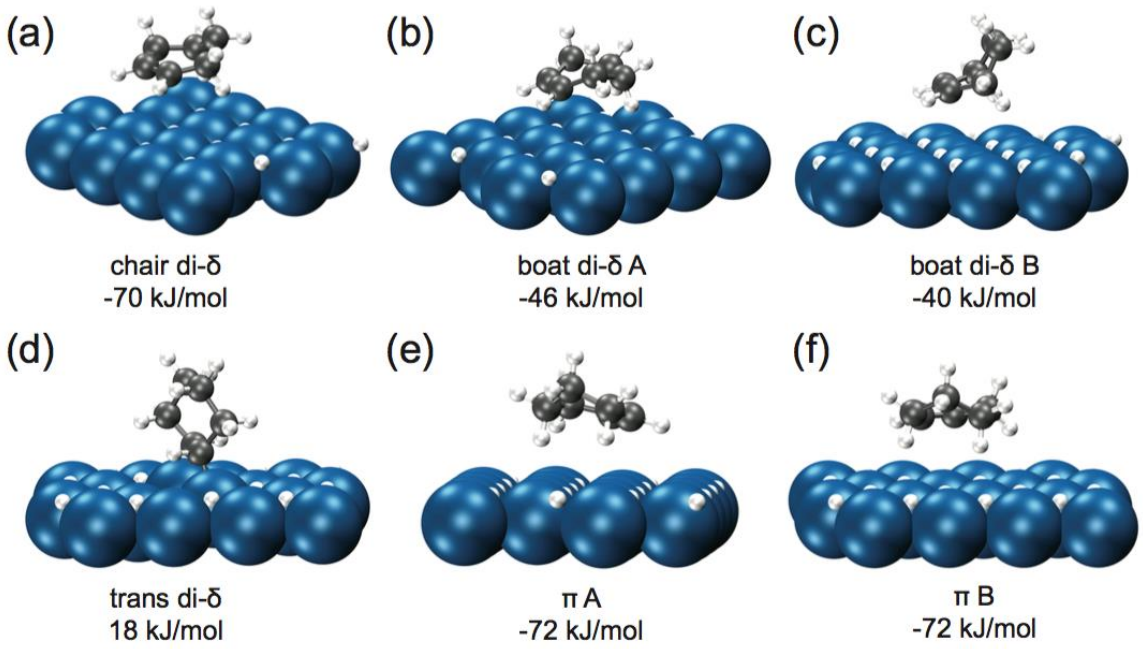

Figure 5. 5 Adsorption structure and energy of cyclohexene on 1ML H-covered Pd (111) surface. Trans di-σ adsorption mode is not stable on crowded surface. The atom colors are Pd in blue, C in gray, and H in white.

5.6 DFT Calculations of Hydrogenation on PdH (111) surface

The energy diagram of the hydrogenation of cyclohexene on Pd (111) is presented in Figure 5. 6. This reaction seems to be a simple reaction with only two consecutive hydrogenation steps. However, among six possible adsorption modes, the mode for the initial state, the most reactive surface species, varies from the most stable surface species

to relatively weakly bound species. In this study, the least stable adsorption mode has been applied as the initial state, because the thermodynamically less stable intermediate might be kinetically significant.[274] We used 1 H on the surface to simulate clean surface hydrogenation, with 14 H atoms co-adsorbed on Pd (111) surface to simulate relatively high coverage of H from kinetic fitting (two adsorbed hydrogens that are very close to cyclohexene were removed in order to generate 14 H on the surface co-adsorbed with cyclohexene). On the clean surface (black solid curve in Figure 5. 6), the first hydrogenation step has a reaction barrier of 221 kJ/mol, whereas the second hydrogenation to form cyclohexane is lower (205 kJ/mol). Comparison of the two indicates that the first hydrogenation step is the rate determining step (RDS). At 14 H-covered high coverage (orange dash line in Figure 5. 6), by adsorbing 1/2 H_2 (gas) at a time so that the population of surface H is kept constant in each hydrogenation step, the activation barrier of the first hydrogenation step drops to 166 kJ/mol because of weaker Pd-C and Pd-H bonds that allow a facile insertion of H in to metal-H bond. Regardless, the first H addition was found to be the rate determining step under high hydrogen coverage. This agrees with the experiments that the rate expression in scenario 3 in Table 5 that describes the kinetics of the hydrogenation of cyclohexene is in a wide range of hydrogen pressure of 30-560 psi.

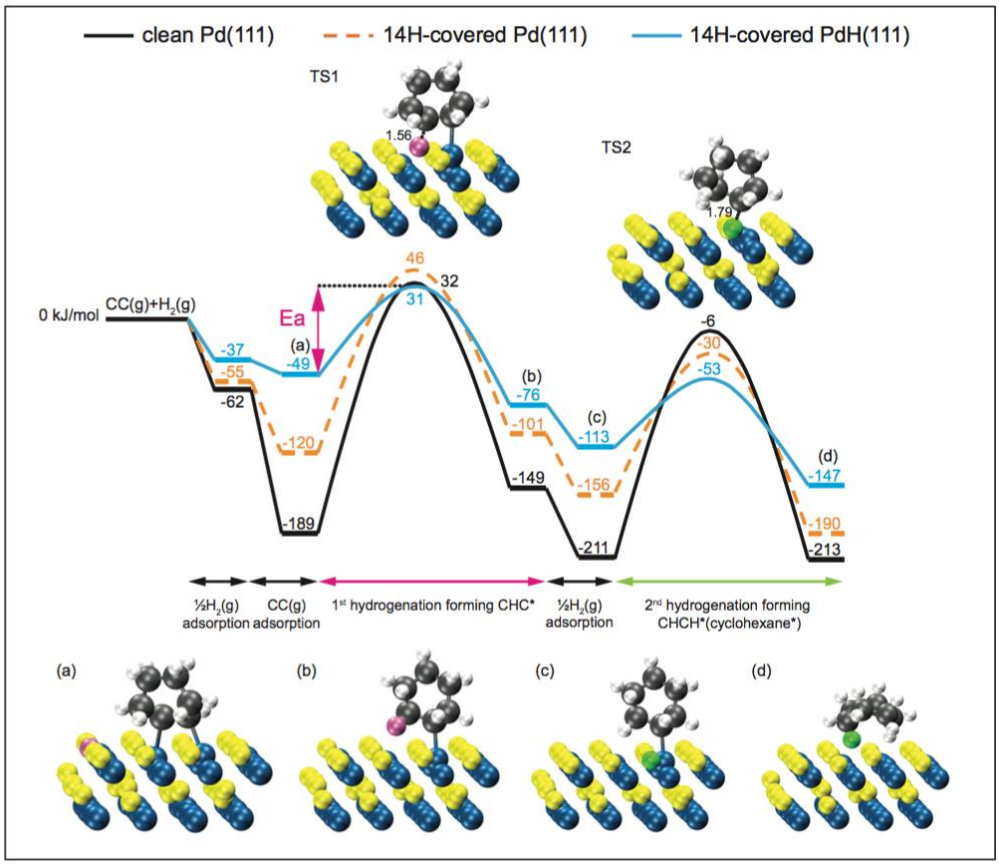

Figure 5. 6 Potential energy diagram of hydrogenation of cyclohexene to cyclohexane on clean Pd(111) surface (black solid curve), 14/16 ML H-covered Pd (111) surface (orange dashed curve), and 14/16 ML H-covered PdH (111) surface (blue sold curve). Insets are showing all the intermediates on PdH (111) surface. Two PdH (111) layers out of four are shown for simplicity. Blue, yellow, gray, and white balls represent Pd atoms, H atoms in PdH slabs, C atoms and H atoms in the molecule. Mauve and green balls indicate the H atom participates in the first and second hydrogenation steps, respectively.

The fitted enthalpy of activation is 81 ± 2 kJ/mol. The DFT calculations have constructed several surface conditions in Figure 5. 6 to explore all possible reaction activations. In addition to reactions on the clean and H-covered Pd (111) surface,

calculations have been carried out on PdH surface[275] because H tends to diffuse into the bulk of Pd crystal results from the highly exothermicity of hydrogen adsorption on Pd.[276] Chemisorbed hydrogen atom can migrate into the subsurface layer and diffuse into the interstitial sites. It can be postulated that on the Pressure-Composition-Isotherms (PCI) phase transition plot for a palladium hydride, Pd has transformed to Pd hydride under studied reaction temperature and hydrogen partial pressure.[277] In order to describe the real experimental conditions, a model system of β-phase hydride was generated. To gain further insight into the effect on PdH formation on cyclohexene hydrogenation activation energies, DFT calculation has been performed on 14H-terminated PdH (111) surface, since PdH also adopts a face centered cubic (FCC) crystal structure. H was found to favor hcp hollow adsorption, indicating a significant repulsion from the H-atom just below FCC-hollow site.[278] It is important to note that H adsorption energies on PdH (111) are less negative than their counterparts on Pd (111). This also applies to cyclohexene binding energy as -12.0 kJ/mol that is much lower than it on 14/16ML-covered Pd (111) surface (Table 6). Much lower adsorption energies on PdH (111) weakens metal-carbon bonds and metal-hydrogen bonds that allows an easier insertion of H, thus lowers the intrinsic activation barrier (marked in Figure 5. 6 E_a). It is suggested by the smaller potential energy drop in Figure 5. 6 (blue solid curve) due to H and cyclohexene adsorption. The intrinsic activation barrier on PdH (111) agrees with kinetic fitting (81 ± 2 kJ/mol) very well with a value of 80 kJ/mol.

It has been observed in Figure 5.6 that hydrogenation steps on Pd (111) are endothermic, along with high activation barriers. However, reactions on PdH become exothermic and activation barrier of the rate-determining step matches with the

experimental value. Analysis on potential energy diagram suggests that there may be hydride forming under real experiment conditions.

5.6 Conclusions

Cyclohexene hydrogenation in three inert nonpolar solvents, heptane, methylcyclohexane and decalin was investigated in a wide range of reaction operation conditions over 0.25% Pd/α-Al_2O_3. Langmuir-Hinshelwood kinetic models are applied for the reaction and four kinetic rate expressions can be derived depending on whether the H_2 adorbs on the same sites with cyclohexene and solvent and which hydrogenation step is the rate determining step.

The reaction order analysis indicates that H_2 dissociative adsorption happens on the different sites than cyclohexene and solvent adsorption, as well as the rate determining step is the first hydrogenation step. The reaction order based on H_2 changes from 0.5^{th} order to 0^{th} order in low H_2 pressure and high H_2 pressure respectively. Furthermore, the reaction order of cyclohexene starts at 1^{th} order and approaches 0^{th} order with cyclohexene concentration in all solvents eventually. Finally, the thermodynamic parameters such as entropy and enthalpy change during reaction and activation are retrieved from the kinetic modelling.

Various adsorption modes of cyclohexene on H-covered Pd (111) and PdH (111) surfaces were investigated using density functional theory calculations. Cyclohexene adsorption energies are affected by H coverage. The reaction activation barrier reduces as more hydrogen are co-adsorbed on the catalyst surface or diffused into catalyst interstitial sites. The activation energy can be reduced from 221 kJ/mol on a complete clean Pd

cluster to 80 kJ/mol on 14 H-covered PdH cluster. Calculations on PdH (111) surface gives a closer energy barrier as compared to kinetic fittings. Our first-principles DFT study, together with the kinetic fitting, provide a comprehensive fundamental work on catalytic hydrogenation of a simple aromatic compound.

Chapter 6. Unravelling How Charge Transfer Influences Plasmonic Catalytic Activity

6.1 Positive versus Negative Effects over Hydrogenation Reactions

6.1.1 Introduction

Photocatalytic conversions mediated or enhanced by surface plasmon resonance (SPR) excitation in plasmonic nanoparticles, the so-called plasmonic catalysis, have emerged as a relatively new frontier in heterogeneous catalysis.[89, 279-281] In this case, gold[282] and silver[283] nanoparticles (NPs), which support SPR excitation in the visible and near-infrared range, are usually employed as catalysts.[281, 284, 285] It is noteworthy that the utilization of copper and aluminum NPs as catalysts have also received attention.[286, 287] Plasmonic nanocatalysis has become attractive towards the development of more environmentally friendly processes, as it enables the utilization of visible/solar light as a green energy input to drive transformations.[281, 288-290] In fact, Ag and Au NPs as well as their hybrids with metal-oxides and graphene-based materials have been investigated as plasmonic catalysts, in which significant enhancements have been reported under SPR excitation.[291-295] It has been established that the SPR excitation can contribute to the enhancement of chemical transformations by a variety of mechanisms. These include local heating by plasmon decay and charge-transfer processes (through direct and indirect mechanisms) that occur as a result of the generation of SPR-excited hot electrons and holes.[89, 280, 281]

Using these principles, plasmonic catalysis has been employed towards the enhancements of several transformations that include: water splitting, CO_2 reduction, degradation of organic pollutants and molecules, oxidations (formaldehyde, alcohols,

amines, carbon monoxide, and propylene), epoxidation of ethylene, carbon–carbon, oxidative, and reductive couplings, hydroamination of alkynes, hydroxylation of benzene, oxidative aldehyde-amine condensation, and hydrogenations.[75, 83, 279, 281, 287, 295-299] Among these several classes of transformations, hydrogenation reactions are particularly important. They play a pivotal role in several petrochemical, chemical, and pharmaceutical processes and industries.[300, 301] Therefore, improvements in catalytic performances are expected to lead to huge economic and environmental impacts. For example, the proper choice of metal nanoparticles (control over their size, shape, and composition), supports, and surface ligands have been pursued in the field of heterogeneous catalysis in order to improve the performance towards hydrogenation reactions.[302] Regarding plasmonic catalysis, the effect of light on H_2-D_2 exchange over Au/TiO_2 and Au/SiO_2 catalysts has been reported.[303, 304] More specifically, it has been demonstrated that SPR-excited hot electrons are able to maximize $H_{2(g)}$ splitting rate on gold at room temperature when these materials are excited by green light. Interestingly, Pd concave nanocubes have also been investigated as plasmonic catalysts for the hydrogenation of styrene,[299] in which it was shown that SPR-excited hot electrons led to a decrease in catalytic activities. These results demonstrate that the precise identification of the mechanisms, by which SPR-excitation leads to improvements in performance, is imperative for the design of optimized plasmonic catalysts.

Even though several reports have focused on investigating the effect of SPR excitation over the enhancement of numerous transformations, several questions remain. For instance, for a specific type of transformation, such as hydrogenation, how sensitive

is the SPR-enhanced catalytic activity to the nature of the reducing agents, metal-substrate charge transfer processes, and reaction pathways?

In this paper, we report the effect of the SPR excitation in Au NPs over their catalytic activities towards hydrogenation reactions. We investigated the effect of two important variables over the plasmonic catalytic performances: *i*) the occurrence of charge transfer processes between the metal NPs and the support; and *ii*) the nature of the reducing agent that enable distinct reaction pathways. Specifically, we employed the hydrogenation of 4-nitrophenol as a model transformation, $BH_4^-{}_{(aq)}$ or $H_{2(g)}$ as the reducing agents, and Au-TiO_2 or Au-SiO_2 NPs as catalysts. Significant enhancements in activity were found under plasmonic excitation for Au/SiO_2 NPs. However, negative catalytic effects were detected on Au/TiO_2 in experiments when the hydrogenation took place in the presence of $BH_4^-{}_{(aq)}$. DFT calculations demonstrated that this is due to charge-transfer of SPR excited hot electrons from Au to TiO_2 when the hydrogenation took place in the presence of $BH_4^-{}_{(aq)}$.

6.1.2 Experimental Methods

6.1.2.1 4-nitrophenol hydrogenation using H_2

Catalytic hydrogenation reactions were performed in Fischer-Porter glass reactors connected to a H_2 reservoir with a pressure regulator which kept the pressure constant. In a typical procedure, 5 mg of catalyst were added to the reactor with 2 mL of ethanol, the volume of substrate added was calculated based on Au's mass on each sample with a molar ratio Au:substrate of 1:10. The reactor was filled with H_2 and the pressure was set at 6 bar. All experiments were performed at 100 °C. These experiments were performed

in triplicate to ensure the significance of their results. The products were quantified using a gas chromatograph with an adequate column for each compound, an internal standard was also used to determine the conversion and selectivity of the products.

6.1.2.2 4-nitrophenol hydrogenation using $NaBH_4$

Hydrogenation reactions were performed in a quartz cuvette and monitored using a UV-Visible Spectrophotometer ranging from 350 nm to 500 nm. Spectra were collected every 150 seconds. A solution containing 4.7×10^{-9} mol Au, 7.0×10^{-8} mol of 4-nitrophenol and 1 mL of distilled water was prepared for each material, and at last 1 mL of a freshly prepared sodium borohydride solution containing 2.5 mg was added. To calculate the conversion of 4-nitrophenol, the change in absorption of the band at 400 nm was monitored. When using TiO_2 colloidal spheres as catalyst, the same amount of catalyst used in the reaction with TiO_2-Au NPs was employed, 7.1 µg of TiO_2 or 5.7×10^{-4} mol, for reactions under visible light, a commercial a 4.5 W LED lamp (Golden – National Brand) was set 5 cm away from the reactor, the position and distance of the lamp onto the reaction were kept constant to minimize any oscillations of light potency. The potency impinging the reactor was measured using a power meter set at 532 nm (Optical Power Meter model 1830 C – Newport) and corresponded to 3.2 mW cm^{-2}.

6.1.3 Computational Methods

DFT computations were performed using the Vienna ab initio simulation package (VASP).[176] The ion–electron interaction were described through the projector-augmented wave (PAW) approach.[178] The exchange and correlation energy was represented using the Perdew-Burke-Ernzerhof (PBE) functional of the generalized gradient approximation

(GGA).[177] The van der Waals (vdW) interaction has been taken into account through the Grimme's DFT-D3 semi-empirical method.[179, 216] Since the standard DFT formulation usually fails to describe strongly correlated electrons, the DFT+U method was used by introducing a hubbard U correction[305] with a value of 3.23 eV[306] acting on 3d electrons of Ti. The model system is a supercell built based on four (4×4) repeated slabs of Au (111) adsorbed on five (5×5) repeated slabs (O-Ti-O trilayers) of TiO_2 anatase (101) with lattice parameters a = 10.36 Å, b = 11.44 Å taken from an optimized TiO_2 unit cell. The bottom three layers of TiO_2 slab were fixed to reflect the bulk. A vacuum space of at least 20 Å was included in the supercell to minimize the interaction between the system and its replicas resulting from the periodic boundary condition. The 4-nitrophenol or H_2 molecule was positioned above the Au surface. The Brillouin zone was sampled by a *k*-point mesh of (3×3×1) for geometry optimizations, and (6×6×2) for density of states (DOS) calculations. A cutoff energy of 300 eV was found to be sufficient to provide convergent results. The structures were relaxed until the atomic force became smaller than 0.01 eV/Å. All the calculations were performed using a Gaussian smearing with a width of 0.2 eV.

6.1.4 Results and discussion

We started with the synthesis of TiO_2 colloidal spheres decorated with Au NPs. It can be observed in the SEM that the Au NPs were monodisperse, uniformly deposited at the TiO_2 surface (no agglomeration), and measured with 9.7 ± 2.2 nm in diameter (Appendix D Figure D. 2 shows the histogram of size distribution). In Au-TiO_2 NPs, it has been demonstrated that charge transfer between Au and TiO_2 can take place under

SPR excitation, in which SPR excited hot electrons are transferred from Au to the TiO_2 conduction band.[307] Also, charge transfer of photo-excited electrons from TiO_2 to Au can take place under UV illumination.[308] Therefore, this system becomes very attractive as a model plasmonic catalyst in order to investigate the effect of charge transfer between the plasmonic nanoparticle and the support over catalytic activities. We also prepared Au/SiO_2 NPs and the resulting Au NPs are 13.6 ± 2.7 nm in diameter (Appendix Figure D. 3). This material was employed as a reference as no charge transfer occurs between the support (SiO_2) and the plasmonic NPs (Au) either under visible (SPR) or UV excitation. The UV-Vis extinction spectra for TiO_2, Au-TiO_2, and Au-SiO_2 NPs is shown in Figure 6. 1. In addition to the peak assigned to the TiO_2 band gap excitation (314 nm), the TiO_2 colloidal spheres (black trace) did not present any bands in the visible range. On the other hand, the Au-TiO_2 NPs (red trace) and Au-SiO_2 NPs (blue trace) displayed a band centered at 535 and 530 nm, respectively, assigned to the dipole modes of the LSPR excitation from Au NPs.[309]

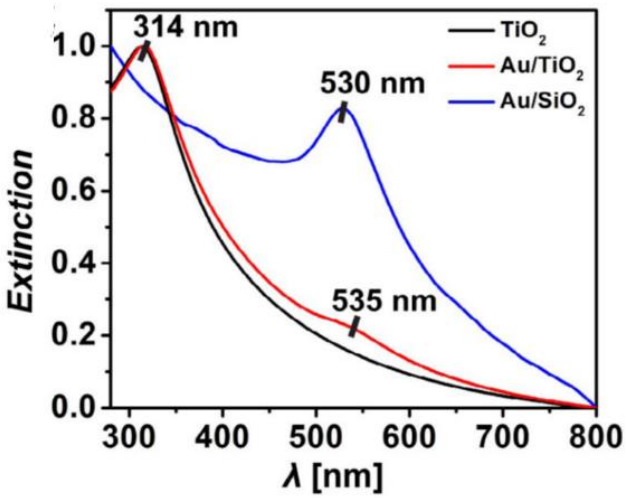

Figure 6. 1 Normalized UV/Vis extinction spectra recorded from aqueous suspensions containing TiO_2, Au/TiO_2 or Au/SiO_2 materials (black, red and blue traces, respectively).

After their synthesis, we aimed at studying how the SPR excitation affected the plasmonic catalytic activities as a function of the occurrence of charge transfer processes between the metal and support and the nature of the reducing agent. We focused on Au-TiO_2 (that enable metal-support charge transfer processes) and Au/SiO_2 NPs (that do not enable metal-support charge transfer processes) as catalysts. Moreover, we chose the hydrogenation of 4-nitrophenol as a model reaction and $BH_4^-{}_{(aq)}$ ions or $H_{2(g)}$ as the reducing agents. This is interesting as these two species have different reaction pathways in reduction reactions involving metal NPs as catalysts.[310, 311] When $BH_4^-{}_{(aq)}$ is employed as a reducing agent, $H^-{}_{(aq)}$ ions are transferred from the $BH_4^-{}_{(aq)}$ to the NPs surface (leading to the formation of M-H bonds), which contribute to the further reduction steps. Here, H^- is transferred to substrate molecules at the nanoparticle surface, which represents the rate-limiting step according to the Langmuir–Hinshelwood model.[310] In the case of $H_{2(g)}$, the rate-limiting step represents the cleavage of molecular hydrogen leading to the formation of two M-H bonds as they interact with the Au surface.[312]

The effect of the SPR-excitation over the conversion % for 4-nitrophenol hydrogenation by $BH_4^-{}_{(aq)}$ was investigated as shown in Figure 6. 2. The obtained conversion % in the absence of light is shown in Figure 6. 2A. A blank reaction (green trace) is also shown. While no significant conversion was detected for the blank reaction or in the presence of TiO_2, both Au-TiO_2 NPs and Au/SiO_2 NPs were effective towards catalyzing this transformation. In particular, the Au-TiO_2 NPs displayed higher

conversion % relative to Au/SiO_2 NPs. In our system, it is plausible that H^{d-} would be formed at the Au surface (metal hydride) and H^{d+} at TiO_2 (bound to an oxygen atom) from BH_4^- (aq). This resulting H^{d-} and H^{d+} pair could improve the rate of the H transfer to polar bonds (NO_2 group in 4-nitrophenol), thus leading to higher reaction rates relative to the Au/SiO_2 catalysts in the absence of light excitation, in which the formation of the H^{d-}/H^{d+} pair is not favored.

Unexpectedly, by employing visible-light excitation with a green LED, we detected a decrease in the catalytic activities for Au/TiO_2 NPs (red trace, Figure 6. 2B). On the other hand, in this case of Au/SiO_2 NPs, a significant enhancement in the conversion % was detected under visible-light illumination. These variations in catalytic activity can be further illustrated by the pseudo-first order rate constants (k) calculated from Figure 6. 2A and B and shown in Figure 6. 2C and D, respectively. It can be observed that k varied from 1.02×10^{-2} to 3.50×10^{-2} min^{-1} in Au/SiO_2 NPs and from 10.96×10^{-2} to 3.10×10^{-2} min^{-1} for Au/TiO_2 NPs after SPR excitation.

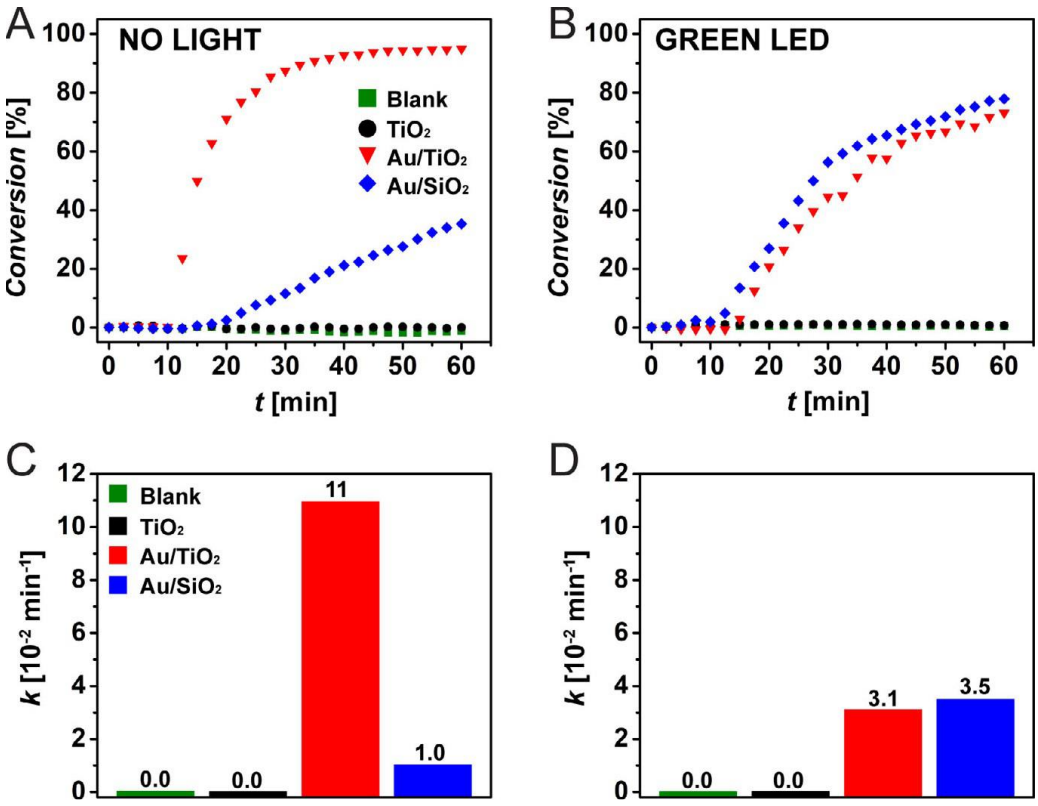

Figure 6. 2 A) and B) % conversion as a function of time for the 4-nitrophenol hydrogenation by BH_4^-(aq) catalyzed by TiO_2 colloidal spheres (black trace), Au/TiO_2 (red trace), and Au/SiO_2 (blue trace). A blank reaction (in the absence of any catalyst) is also shown (green trace). In (A) and (B), the reaction was performed in the absence and presence of visible-light excitation by a green LED, respectively. (C and D) show the pseudo-first-order rate constants (k) obtained from (A and B), respectively.

Figure 6. 3A and B show our proposed mechanism for the variations in activity under SPR excitation for both Au/SiO_2 and Au/TiO_2 NPs. It is well-established that the SPR excitation in plasmonic nanoparticles lead to the generation of hot-electrons and holes.[280, 281] It has been shown that these SPR-excited hot-electrons can be charge-transferred to adsorbed molecules.[77] In Au/SiO_2 NPs, no charge transfer of SPR-excited

hot electrons can take place from Au to SiO_2. Therefore, the SPR-excited hot electrons can be transferred to the lowest unoccupied adsorbate state (indirect charge transfer mechanism, Figure 6. 3A).[76] This leads to a formation of a transient adsorbate species which facilitates the transfer of H^- ions at the metal surface to the adsorbate and thus accelerates the reaction. Although this mechanism has been described for several plasmonically enhanced transformations, its observation in hydrogenation remains limited. Moreover, reports on the enhancement of the 4-nitrophenol reduction by BH_4^- under SPR excitation have been mainly assigned to local heating due to plasmon decay.[313] However, we believe that this is not the case, otherwise the same behavior would also be observed for Au/TiO_2 NPs.

In Au/TiO_2 NPs, it has been shown that SPR-excited hot electrons generated at Au NPs can be transferred to the conduction band of TiO_2.[314, 315] Therefore, we propose that hot electrons are transferred from Au to TiO_2 NPs following SPR excitation and thus do not become available for transfer to unoccupied adsorbate states (Figure 6. 3B). Figure 6. 3C shows the DFT-calculated electronic structure of 4-nitrophenol adsorbed on TiO_2-supported Au layers. The LUMO orbital of the 4-nitrophenol molecule is located within 2 eV above the Fermi Level. The conduction band of TiO_2 is located at a similar energy window. Charge analysis within this energy range show states at both TiO_2 and the NO_2 group of the 4-nitrophenol. These degenerate states suggest that electrons excited in Au particles may have two interfacial charge transfer directions. The built-in electronic field at the Au/TiO_2 interface (Figure 6. 3C) drives electron into TiO_2 and the Schottky barrier between Au and TiO_2 prevent electrons from getting back to Au. Whereas the weak interaction between the molecule and Au hinders the electron injection into the molecular

orbital. Because of this directional electron transfer, reduction of the NO_2 group is thus not facilitated by the hot electrons. Instead It is possible that the generated holes can oxidize H^- species bound at the Au NPs surface back to H_2. This would lead to a decrease in the rate of the reaction as the transfer of H^- species to adsorbed 4-nitrophenolate molecules represents the rate-limiting step for the 4-nitrophenol hydrogenation by BH_4^- catalyzed by metal NPs.

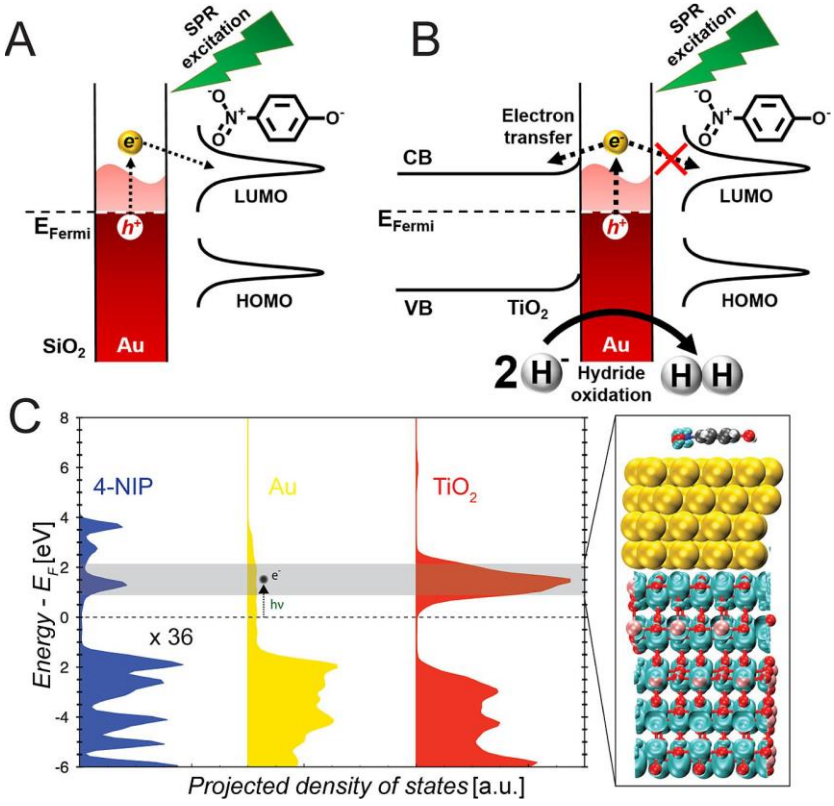

Figure 6. 3 Scheme for the detected increase in activity towards the 4-nitrophenol hydrogenation by BH_4^-(aq) catalyzed by Au/SiO_2 under LSPR excitation (A), and the detected decrease in activity when catalyzed by Au/TiO_2 under LSPR excitation (B). (C) DFT-calculated electronic structure of 4-nitrophenol adsorption on an Au/TiO_2 surface. Projected density of states of each component (4-nitrophenol, Au, TiO_2) is shown for

comparison. The charge-density plot shows the degenerate states of the conduction band of TiO_2 and the LUMO of 4-nitrophenol. The isosurface is set to 0.12 e A^{-3}.

We also performed this same transformation using $H_{2(g)}$ as the reducing agent. Even though Au NPs have displayed high activities towards a myriad of reactions, relatively low activities towards hydrogenations using $H_{2(g)}$ as the hydrogen source have been described.[316] Figure 6. 4 depicts the conversion % for the 4-nitrophenol hydrogenation by $H_{2(g)}$. In the absence of SPR-excitation (Figure 6. 4A), no significant conversion was detected for both blank reaction and TiO_2 colloidal spheres and the conversion on Au/TiO_2 NPs were higher relative to Au/SiO_2 NPs. The higher catalytic activity of the Au/TiO_2 NPs is assigned to the promotional effect of the TiO_2 support. This has been observed in other Au/TiO_2 NPs systems, in which the formation of low-coordinated Au atoms at the interface can induce the H_2 cleavage and thus favor the reaction.[301]

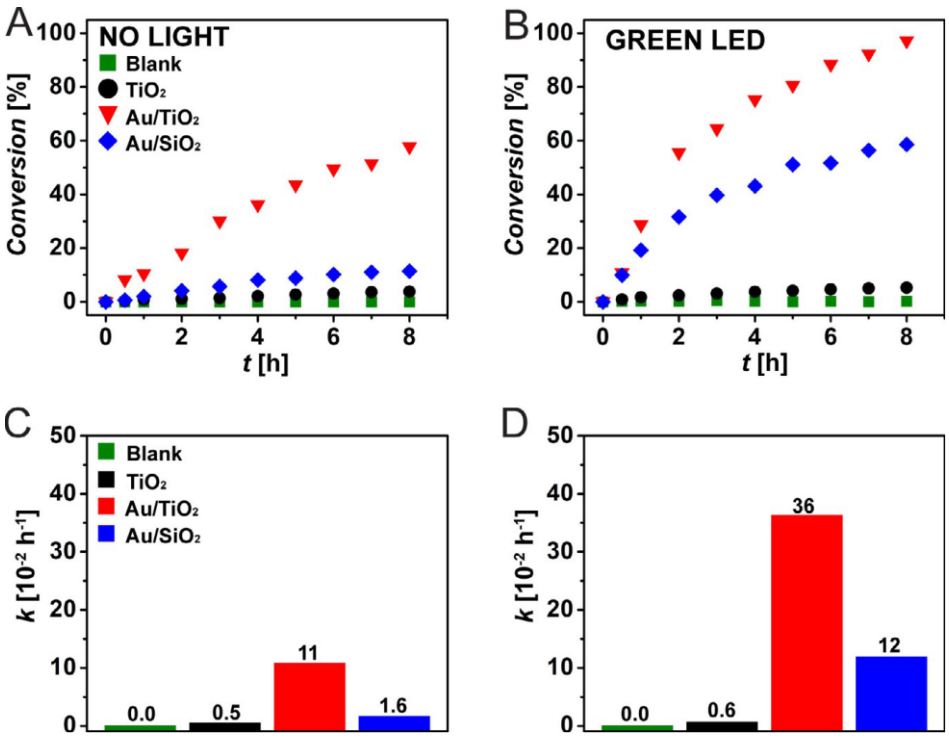

Figure 6. 4 (A and B) % conversion as a function of time for 4-nitrophenol hydrogenation by $H_{2(g)}$ catalyzed by TiO_2 colloidal spheres (black trace), Au/TiO_2 (red trace), and Au/SiO_2 (blue trace). A blank reaction (in the absence of any catalyst) is also shown (green trace). In (A), the reaction was performed in the absence of visible light excitation (conventional catalysis), whereas in (B) the reaction was performed under a green light excitation (plasmonic catalysis). (C and D) show the pseudo-first-order rate constants (k) obtained from (A and B), respectively.

The conversion % for both catalysts increased when the reaction was carried out under visible light illumination (Figure 6. 4B). The pseudo-first order rate constants (*k*) increased from 10.86×10^{-2} to 36.34×10^{-2} h^{-1} and from 1.63×10^{-2} to 11.89×10^{-2} h^{-1} after visible light excitation (green led) for the Au/TiO_2 and Au/SiO_2 NPs, respectively. The mechanism for the increase of activities under SPR excitation for the reduction of 4-nitrophenol by $H_{2(g)}$ is depicted in Figure 6. 5. In fact, it has been demonstrated that the

SPR excitation in Au NPs supported both on TiO_2 and SiO_2 lead to an increase in the rate of hydrogen dissociation. This phenomenon has been assigned, both experimentally and theoretically, to the transfer of SPR-excited hot electrons from Au NPs to the H_2 anti-bonding orbital.[75, 83] Figure 6. 6 depicts the DFT-calculated electronic structure of H_2 adsorption on an Au surface. It can be observed that the LUMO orbital of H_2 on Au is very close to the Fermi level and much lower relative to the LUMO of 4-nitrophenol and the TiO_2 conduction band (Figure 6. 4C). Thus, it is plausible that this contributes for a preferential transfer of hot electrons to the H_2 LUMO orbital relative to the support. The transfer of hot electrons to the H_2 LUMO orbital aids the H_2 splitting at the surface and thus increases the reaction rates. It is important to note that in hydrogenations involving H_2 on Au catalysts, the H_2 splitting at the surface is usually the rate-limiting step.[310, 317] Another important observation is that the relative increase on the conversion percentage under SPR excitation was observed for Au-SiO_2 NPs relative to Au-TiO_2 NPs. In the Au-TiO_2 NPs, the presence of a Schottky barrier may also enable the transfer of SPR-excited hot electrons to the TiO_2 conduction band, reducing the number of hot electrons available for transfer to the H_2 antibonding orbitals.

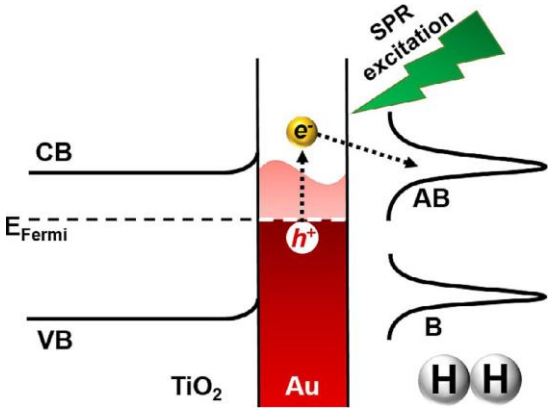

Figure 6. 5 Proposed mechanism for the detected increase in activity towards 4-nitrophenol hydrogenation by $H_{2(g)}$ catalyzed by Au/TiO_2 NPs under LSPR excitation.

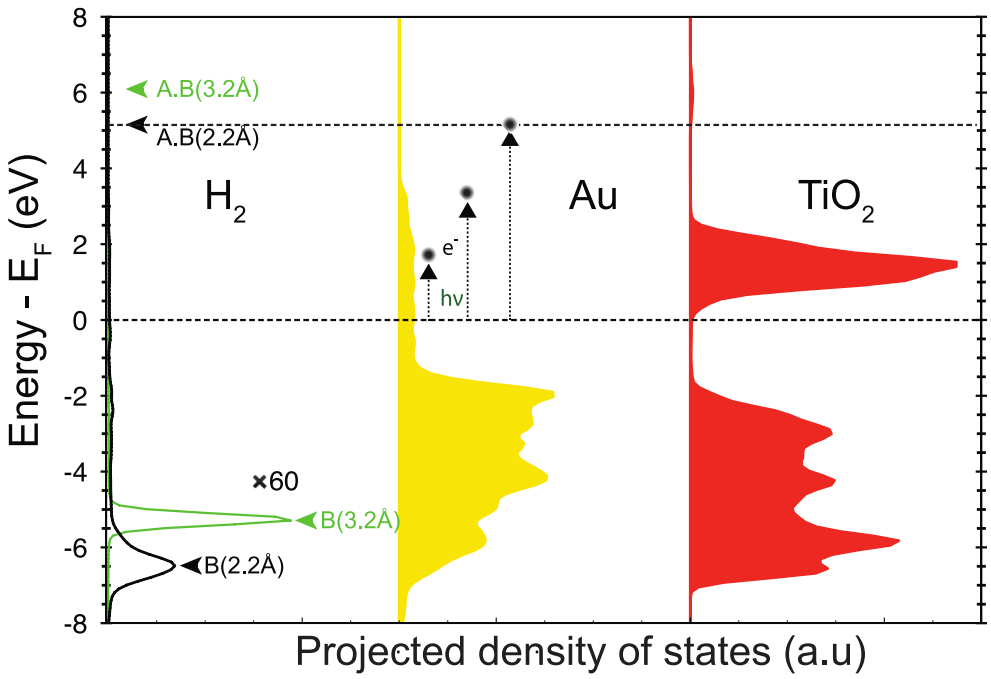

Figure 6. 6 DFT calculated electronic structure of H_2 adsorption on an Au/TiO_2 surface. Projected density of states of each component (H_2, Au, TiO_2) are shown to compare. For H_2 adsorption, we considered the physiosorbed H_2 on the surface with a vertical distance of 3.2 Å from the surface (green) and another configuration we artificially reduced the H_2 height with respect to the surface to 2.2 Å (black). Antibonding state of H_2 in each configuration is shown. The non-equilibrium hot electron in Au may be excited to ~ 5 eV about the Fermi level and injected into the H_2 antibonding state. Note electron of this energy ~ 5 eV is still bound to the Au particle because it is still between the vacuum level and Fermi level of Au.

6.1.5 Conclusions

We have systematically investigated the effect of SPR-excitation over the plasmonic catalytic activity of Au NPs supported on TiO_2 and SiO_2 towards hydrogenation reactions. We focused on how the plasmonic catalytic activity was sensitive to the nature of the reducing agent and the occurrence of charge-transfer processes between a SPR-excited metal and the support. Our results showed that both these parameters strongly affected the plasmonic catalytic activities. In particular, we employed the 4-nitrophenol hydrogenation was a model transformation and $BH_4^-{}_{(aq)}$ ions or $H_{2(g)}$ as the reducing agents. While a decrease in activity for the 4-nitrophenol reduction by $BH_4^-{}_{(aq)}$ was observed under plasmonic excitation for Au/TiO_2 NPs, an increase in activity was detected for Au/SiO_2 NPs. When $H_{2(g)}$ was employed as a reducing agent, an increase in activity under SPR excitation was detected for both Au-TiO_2 and Au-SiO_2 NPs. The results described herein shed important insights in the field of plasmonic catalysis, in which we've demonstrated that the effect of plasmonic excitation over hydrogenation reactions can be completely different as a function of the nature of the reducing agents and the utilization of supports that enable charge-transfer processes to take place. It is noteworthy that other types of transformations may also display a similar behavior and deserve further investigation. We believe that this knowledge will pave the way for the improved design of plasmonically-enhanced and greener chemical processes.

6.2 Localized Orbital Excitation Drives Bond Formation in Plasmonic Catalysis

6.2.1 Introduction

Chemical transformations on plasmonic metals can be enhanced under visible-light irradiation. Previous works explained this enhancement as energetic carriers being populated at the molecular orbitals of the reactants leading to bond dissociation. It remains unclear whether such energetic carriers can also assist with bond formation, which is a critical elementary step in reactions. Here, we present experimental and theoretical results of reduction of a nitroaromatic molecule. We use the reduction of nitrophenol as a prototype reaction, and show that, when borohydride is used as a reducing agent, the reaction rate is greatly enhanced under plasmonic excitation. Density functional theory calculations suggest that an energetic electron positioned at the reactant frontier orbital lowers the barrier for nitrophenol activation and stimulate bond formation. This effect can be further enhanced if the excited electrons can be localized at the molecular orbital that is electronically decoupled from the plasmonic metal. Specifically, we use reduction of 4-nitrophenol as a model reaction. 4-Nitrophenol is a pollutant in wastewater as a byproduct from pesticides, dyes and pharmaceuticals,[318] and its reduction to 4-aminophenol (aniline) is a valuable industry process. In this paper, we unravel the reaction mechanism in the plasmonic reduction of 4-nitrophenol on gold nanoparticles. We measured the catalytic activity on SiO_2-supported Au catalyst with and without light irradiation and observed higher reaction rate under light. The effect of light was elucidated by the comparison of the ground-state (without electronic excitation) and excited-state (with electronic excitation) potential energy surfaces (PES) based on

standard density functional theory and delta self-consistent field calculations. We observed a reduced activation barrier on the excited-state PES in the presence of extra charge; however, caused by the degeneracy of molecular orbitals and the metal extended d orbitals, it is challenging to ambiguously identify the role of the excited electrons in lowering the activation barrier. We thus propose to decouple the molecular frontier orbitals from Au by inserting a thin layer of hexagonal boron nitride (*h*-BN). We find the activation barrier of the rate-limiting step for reduction of 4-nitrophenol is significantly lowered, because of localized charge in the molecular frontier orbital.

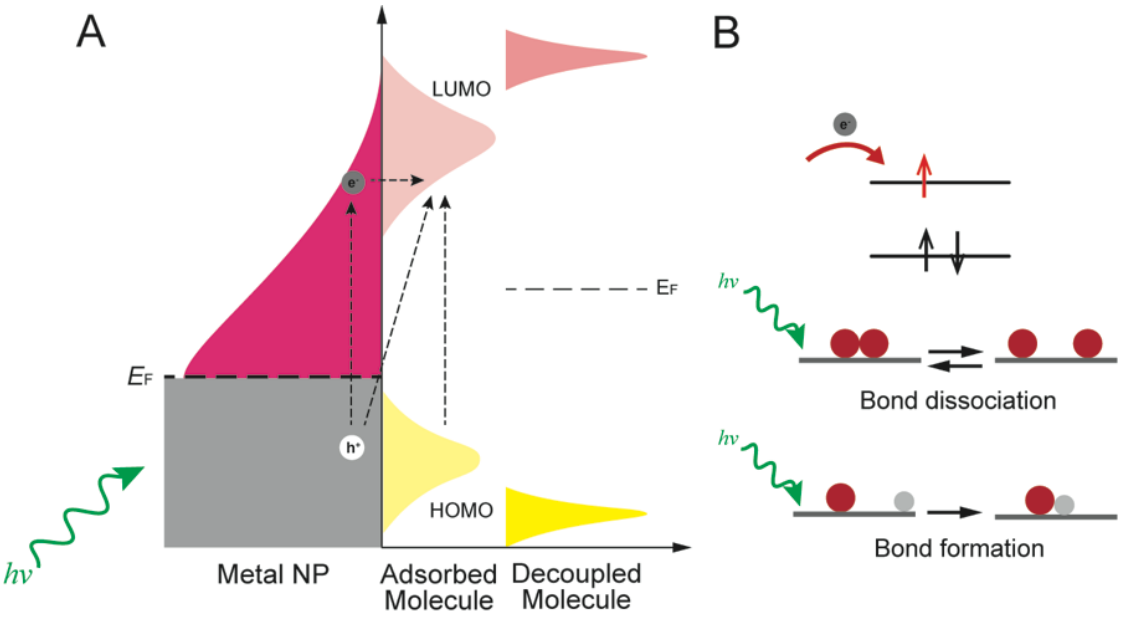

Figure 6. 7 Mechanisms of plasmon-driven photocatalysis on metal NPs under light irradiation. A. Schematic diagram of electronic excitation and charge transfer under visible light. If the photon energy matches the interfacial electronic states of the chemisorbed molecules, electrons may be excited directly from the molecular HOMO orbital or the occupied metal states to the LUMO orbital of the reactant. Hybridization between the metal d states and the molecular frontier orbitals broadens the latter ones and

makes it challenging to localize the excited carriers at specific orbitals. B. The schematic shows the bond dissociation could be assisted by adding an electron into the anti-bonding orbital of the molecule. The role of energy transfer in plasmonic bond formation could be distinct from the bond dissociation mechanism.

6.2.2 Experimental Methods

6.2.2.1 Synthesis of Au NPs

Au NPs were prepared by the citrate reduction approach.[30] In a typical procedure, 95 mL of H_2O were mixed with 5 mL of 0.5 wt. % sodium citrate trihydrate in a 250 mL round-bottom flask. This system was heated to 100 °C for 15 minutes under magnetic stirring followed by the addition of 2 mL of an aqueous solution of $AuCl_4^-$ 25mM. The reaction proceeded for approximately 10 minutes yielding a red suspension containing the Au nanoparticles.

6.2.2.2 4-Nitrophenol hydrogenation by $NaBH_4$ catalyzed by Au NPs

All the hydrogenation reactions were performed in a quartz cuvette and monitored using a UV/VIS spectrophotometer ranging from 250 nm to 500 nm. In a typical procedure, 1.5 mL of a 0.14 mM 4-nitrophenol aqueous solution was mixed in a quartz cuvette with 0.25 mL of freshly prepared 42 mM sodium borohydride solution. Afterwards, 100 L of 0.5 mM aqueous suspension containing the Au NPs were added to the quartz cuvette and this instant was defined as the reaction starting time (t = 0). To calculate the conversion of 4-nitrophenol, the change in absorption of the band at 400 nm

was monitored. In order to obtain different 4-NPh/BH_4^- molar ratios, we varied the volume of the 42 mM sodium borohydride solution added to the reaction, corresponding to 5, 25, 50, 250 and 500 L for 1:1, 1:5, 1:10, 1:50 and 1:100 molar ratios, respectively. For reactions carried out under visible light excitations, a LED green lamp (525 nm) was employed as the excitation source. The lamp was set 10 cm away from the reactor, and the position and distance of the lamp onto the reaction were kept constant in all experiments. The potency impinging the reactor corresponded to 10 mW/cm^2.

6.2.3 Computational Methods

All density functional theory calculations were carried out using Vienna Ab initio simulation package (VASP[176]), version vasp.5.4.1. The Perdew-Burke-Ernzerhof generalized gradient approximation exchange-correlation potential (PBE-GGA[319]) was used, and the valence electron wave function were treated in the projector augmented wave (PAW[243, 320]) method with a kinetic cutoff energy of 400 eV. The van der Waals interaction has been taken into account through Grimme's DFT-D3 semiempirical method.[137] The reactions were modeled accordingly. Gaussian smearing (width = 0.2 eV) was used to calculate the partial occupancies. The structures were relaxed until the force acts on each atom is smaller than 0.02 eV $Å^{-1}$. The electronic energy convergence was set to 1.0×10^{-5} eV / atom.

Au (111) was chosen to represent the energetically most stable facet. The close-packed Au (111) slab was modeled with a 4 × 4 supercell composed of four atomic layers and 20 Å of vacuum between the slabs in the Z-direction. The bottom two layers were frozen to emulate the bulk, while the top two layers and molecules positioned above the

Au surface were allowed to relax. The Brillouin zone was sampled with a 3 × 3 × 1 k-point grid for structural optimizations, and a 6 × 6 × 2 k−point grid for the density of states (DOS) calculations under this study.

To model the monolayer hexagonal boron nitride (*h*-BN), a boron nitride unit cell was optimized and cleaved in the (0 0 1) direction to form a graphenelike honeycomb structure consisting of 16 B and 16 N atoms. The BN layer was placed in the middle of the box and a large spacing of 15 Å was added to avoid interactions between layers. To model the carbon-doped *h*-BN monolayer, an N atom was replaced by a C atom, resulting in the C-B bond length being 1.49 Å, which is 0.05 Å longer than the B-N bond length (1.44 Å) in the pristine *h*-BN monolayer.

Transition state searches were performed using the dimer method[143] with the initial guesses for the transition state structure obtained through the nudged elastic band (NEB) method with eight images between initial and final states.[142] The transition states were confirmed with the presence of a unique imaginary frequency in the vibration frequency calculations. The minimum-energy paths for the reactions were then determined.

The Bader charge analysis was implemented to determine the charge state localized on each atom in the system.[321-323]

The adsorption energy (E_{ads}) was calculated as $E_{ads} = E_{i/slab} - (E_{slab} + E_i)$ where $E_{i/slab}$, $E_{slab,}$ E_i are the energies of the slabs with the adsorbed molecule, the clean metal slab, and the molecule in the gas phase, respectively. The energies of the adsorbates and gas phase molecules were calculated using a 10×10×10 supercell with a gamma-only k-point mesh.

To map the excited-state energy curves, an extra electron was added to a certain energy level. In order to estimate the excitation energy for electrons traveling from Au to 4-NPh molecule, the partial density of states and band separation calculations were performed. With the estimated excitation energy, by using a linear expansion delta self-consistent field extension of DFT (ΔSCF-DFT).[150] the excited-state energy curves along the minimum-energy path of the rate-limiting step was calculated. In this method, we first calculated and interpreted the Kohn-Sham (KS) orbitals as the molecular orbital, and the relevant KS orbitals were analyzed and identified through analysis of the local density of states and the electron density of each KS orbital. Then, the occupation in the relevant KS orbitals was modified and the system was relaxed self-consistently in a way that keeps the electron/hole in the relevant KS orbitals to model excited states.[149]

The simulation results were analyzed using Visual Molecular Dynamics (VMD)[324] and Visualization for Electronic and Structural Analysis (VESTA).[245]

6.2.4 Maximum Rate Analyses

The Langmuir-Hinshelwood (LH) kinetic approach was employed to describe 4-NPh hydrogenation in the sequence which includes the crucial steps such as surface adsorption, surface reactions and surface desorption. The most favorable mechanism is presented as the following equations:

$$BH_4^-(aq) + * \overset{k_1}{\leftrightarrow} BH_3^-(aq) + H^*$$

$$\Delta G = 0 \qquad \text{Elementary step 1}$$

$$NPh + * \overset{K_{NPh}}{\longleftrightarrow} NPh^* \qquad \text{Elementary step 2}$$

$NPh^* + H^* \xrightarrow{k_3} R - NO(OH)^* + *$ Elementary step 3

$R - NO(OH)^* + H^* \xrightarrow{k_4} R - N(OH)_2^* + *$ Elementary step 4

$R - N(OH)_2^* + H^* \xrightarrow{k_5} R - N(OH)^* + H_2O\ (g) + *$ Elementary step 5

$R - N(OH)^* + H^* \overset{k_6}{\leftrightarrow} R - NH(OH)^* + *$ Elementary step 6

$R - NH(OH)^* + H^* \overset{k_7}{\leftrightarrow} R - NH^* + H_2O\ (g) + *$ Elementary step 7

$R - NH^* + H^* \overset{k_8}{\leftrightarrow} APh^* + *$ Elementary step 8

$APh^* \overset{K_{APh}}{\longleftrightarrow} APh + *$ Elementary step 9

Where R denotes the hydroxyphenyl radical, * represents an empty Au site available for adsorption. K and k are adsorption constants and rate constants, respectively.

Following the reaction elementary steps shown in equation 1 through 9, we are able to derive the maximum rate of each elementary step[325] (θ^* is equal to unity when the reaction rate is maximized):

$$r_1 = \frac{k_B T}{h S_0} [H^{*\ddagger}]$$

$$K_1^{\ddagger} = e^{-\Delta G_1^{\ddagger}/k_B T} = \frac{\theta_{H^*}^{\ddagger}}{\theta^* C_{BH_4^-}(aq)}$$

$$r_{1,max} = \frac{k_B T}{h} e^{-\Delta G_1^{\ddagger}/k_B T} C_{BH_4^-}(aq)$$

$$r_2 = \frac{k_B T}{h S_0} [NPh^{*\ddagger}]$$

$$K_2^{\ddagger} = e^{-\Delta G_2^{\ddagger}/k_B T} = \frac{\theta_{NPh^*}^{\ddagger}}{\theta^* P_{NPh}}$$

$$r_{2,max} = \frac{k_B T}{h} e^{-\Delta G_2^{\ddagger}/k_B T} P_{NPh}$$

$$r_3 = \frac{k_B T}{h S_0}\left[\theta^{\ddagger}_{R-NO(OH)^*}\right]$$

$$K_3^{\ddagger} = e^{-\Delta G_3^{\ddagger}/k_B T} = \frac{\theta^{\ddagger}_{R-NO(OH)^*}}{\theta_{NPh^*}\theta_{H^*}}$$

$$r_{3,max} = \frac{k_B T}{h} e^{(-\Delta G_3^{\ddagger} - \Delta G_2 - \Delta G_1)/k_B T} P_{NPh} C_{BH_4^-}(aq)$$

$$r_4 = \frac{k_B T}{h S_0}\left[\theta^{\ddagger}_{R-(OH)_2^*}\right]$$

$$K_4^{\ddagger} = e^{-\Delta G_4^{\ddagger}/k_B T} = \frac{\theta^{\ddagger}_{R-(OH)_2^*}}{\theta_{R-NO(OH)^*}\theta_{H^*}}$$

$$r_{4,max} = \frac{k_B T}{h} e^{(-\Delta G_4^{\ddagger} - \Delta G_3 - \Delta G_2 - 2\Delta G_1)/k_B T} P_{NPh}[C_{BH_4^-}(aq)]^2$$

With $\Delta G_i^{\ddagger}$ indicating the transition state Gibbs free energy change and ΔG_i indicating the reaction Gibbs free energy change. According to realistic experimental conditions, $C_{BH_4^-}(aq)$ is 0.066 mol/L, and P_{NPh} is 0.002 atm. The rate is not directly compared to the experiments but used to compare different elementary steps to identify the RLS.

We included the zero-point energy (ZPE)[326] in enthalpy:

$$\text{ZPE} = \sum_i \left(\frac{1}{2}\right) h\upsilon_i$$

Where h is the Planck constant, υ_i is the DFT-calculated real frequencies of the system. The enthalpy was added up as the following equation:

$$H = E_{DFT} + ZPE + \int_{0K}^{T} C_V dT$$

In which $\int_{0K}^{T} C_V dT$ can be written as $\sum_i \frac{h\upsilon_i}{e^{h\upsilon_i/k_B T}-1}$, $k_B$is the Boltzmann constant.

The vibrational entropy contributions were calculated using the harmonic normal node approximation:[327]

$$S_{vib=}\, k_B \sum_i [\frac{h\upsilon_i}{k_B T(e^{\frac{h\upsilon_i}{k_B T}} - 1)} - \ln\left(1 - e^{-\frac{h\upsilon_i}{k_B T}}\right)]$$

The Gibbs free energy of the system at each state can be computed from the enthalpy and entropy values.

$$G = H - TS$$

According to Datta et al., the resistance for each elementary step can be described as:

$$R_{j,max} = \frac{1}{r_{j,max}}$$

The calculated maximum rates and the corresponding resistances are summarized in Table D. 1. The rate-limiting steps are likely the ones with the lowest maximum rate (highest resistance).

6.2.5 Results and discussion

6.2.5.1 Reduction of 4-nitrophenol (4-NPh) on Au surfaces

Prior work showed that the catalytic reduction of 4-NPh on Au and Ag nanoparticles could be enhanced under visible light,[85, 328] although the mechanism has not yet been reported. We have evaluated herein the conversion as a function of time for the 4-NPh hydrogenation by BH_4^-(aq) on Au NPs under LSPR excitation by a green LED light source, with various 4-NPh:BH_4^- molar ratios, as shown in Figure 6. 8. External heating was not employed. It can be clearly observed that the conversion under LSPR excitation is strongly dependent on the 4-NPh:BH_4^- molar ratios, increasing as the proportion of BH_4^- in the reaction. The initial rate constants, calculated up to 5s of

reaction, are shown in Table 7. The conversion and initial rate constants under light excitation are higher than ones under similar conditions without light irradiation for all 4-NPh:BH_4^- molar ratios (dark conditions, Figure 6. 8A). This result is in agreement with our previous reports,[328] which showed that the reaction rates for this chemical transformation on SiO_2-supported Au was greatly enhanced by LSPR excitation.

This enhancement is unlikely caused by thermal heating because of a distinct trend observed over TiO_2-supported Au under LSPR excitation. That is, decrease in reaction rate was observed under LSPR excitation over TiO_2-supported Au due to charge transfer into TiO_2 by the built-in electric field at the interface.[328] This distinct behavior between SiO_2- and TiO_2-supported Au under the same reaction conditions indicates that plasmonic heating is not the driving force, which otherwise should enhance rates in both systems. Instead, energy transfer through LSPR excitation is likely the predominant factor for the enhanced rates over SiO_2-supported Au.

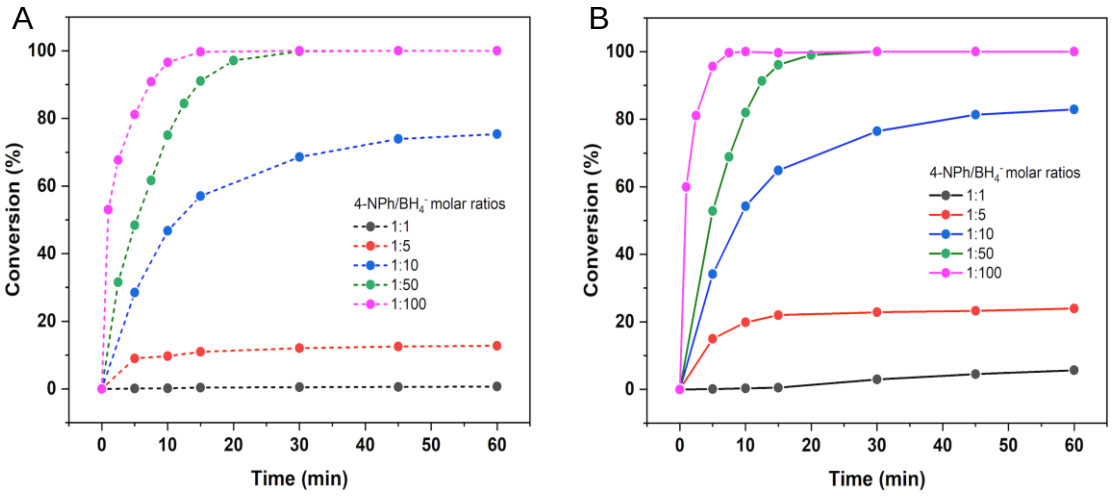

Figure 6. 8 Reduction of 4-nitrophenol by BH4- catalyzed by Au NPs. Conversion as a function of time under different 4-NPh/BH_4^- molar ratios under dark (A, dashed lines)

and under light (B, solid lines) conditions. All reactions were conducted under ambient conditions. A green LED lamp (525 nm) was employed for LSPR excitation.

4-NPh/BH_4^- molar ratios	Initial rate constant *k* (10^5 mol·L^{-1}·min^{-1})	
	Dark	LSPR excitation
1:1	0.0258	0.0264
1:5	2.3281	3.8724
1:10	7.2598	8.6896
1:50	10.9878	11.9845
1:100	16.2246	19.1212

Table 7 The initial rate constants calculated at various 4-NPh:BH_4^- molar ratios under dark and LSPR excitation.

6.2.5.2 DFT Calculations of the reaction profile at ground state

In the following we explore the reaction mechanism by performing density functional theory calculations. We first compared different adsorption configurations of 4-nitrophenol on a Au (111) surface (the most stable facet) to determine the most stable structure (Figure D. 4). It was found that the most stable adsorption structure entails the molecule lying flat on the surface. The aromatic ring interacts with four Au atoms to maximize the d-π interaction (Figure 6. 9A). Oxygen atoms from the nitro group bind closer to the surface than the aromatic ring due to their high electrophilicity (Figure 6. 9B). This configuration is similar to previously reported adsorption modes of nitroarene on nickel, platinum and other metals.[329, 330] The adsorption energy of 4-NPh is -102 kJ/mol with the van der Waals corrections. Accordingly, the distance between O_1 and O_2 (labelled in Figure 6. 9B) in the nitro group and the nearest Au atom is 3.23 and 3.03 Å, respectively. Note BH_4^- was employed as the reducing agent in experiments. The interaction of borohydride ions with Au NPs produces adsorbed H species.[331, 332] The

adsorption of the atomic H over Au (111) surface is thermodynamically unfavorable; it adsorbs most strongly on the face-centered cubic (*fcc*) sites of Au (111) with an energy cost of 0.10 eV as referenced to H_2 in the gas phase, consistent with literature.[35]

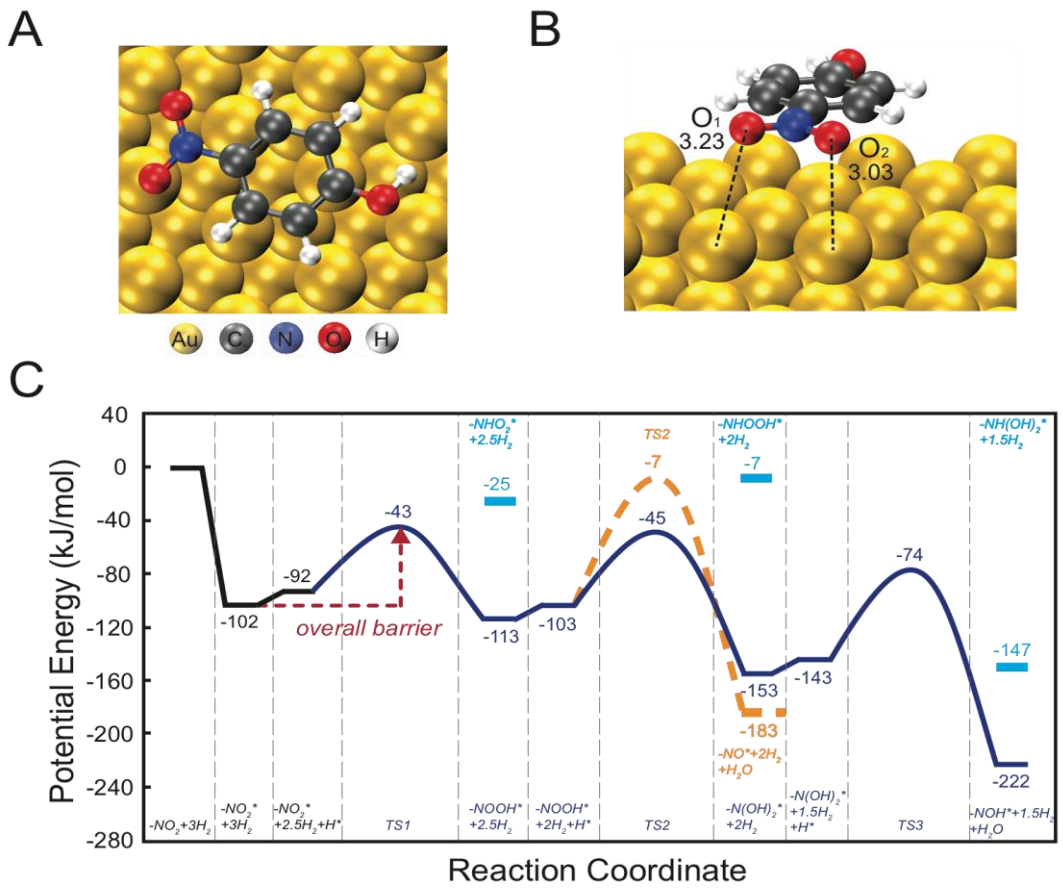

Figure 6. 9 Optimized geometries of 4-nitrophenol on Au (111): Top view (A) and side view (B) of the most stable adsorption structure. C. The potential energy profile for the 4-nitrophenol hydrogenation (first three hydrogenation steps) catalyzed by Au (111). The reaction starts with adsorption of 4-nitrophenol, and each subsequent reaction involves adsorption of ½ H_2 and its transfer to the reactant. Only the top two layers of Au atoms are displayed for simplicity.

We then computed the kinetic barriers of 4-nitrophenol reduction to 4-aminophenol (4-APh) on Au (111) to identify the rate-limiting step. Here we analyzed the reaction kinetics of surface-adsorbed species in terms of the Langmuir-Hinshelwood mechanism,[333] in which both reactants (4-NPh and H) adsorb on the surface. Previous study indicates that formation of surface-hydrogen species via borohydride ions on the Au surface is reversible and fast, which can be modeled by the Langmuir-Freundlich isotherm.[332] Also, adsorption of 4-NPh and desorption of products are assumed to be fast, so that the rate-limiting step takes place between surface-hydrogen and adsorbed species.[333] The reduction reaction of 4-NPh to the corresponding 4-APh on metal catalysts is a six-electron transfer process.[334] It is important to note that adding the first hydrogen on O-1 exhibits similar energy barrier to adding it on O-2, so that only one case is shown here. Figure 6. 8C summarizes the most likely potential energy profile from ground-state calculations. All the energies reported here don't consider lateral interactions between adsorbates. The first hydrogenation on O-2 to form R-NO(OH)* has a true activation barrier of 49 kJ/mol and reaction energy of -21 kJ/mol. The hydrogenation of N is highly unfavorable thermodynamically with an energy cost of 67 kJ/mol. The second hydrogenation has several possible pathways. The energy cost for hydrogenation of N is 96 kJ/mol. Alternatively, we examined hydrogen attack to the hydroxyl group forming a water molecule. This step is highly exothermic (-80 kJ/mol), due to the formation of two stable intermediates (R-NO* and H_2O), but it renders a high activation barrier as 96 kJ/mol. It is more likely that the reaction proceeds to form $N(OH)_2$* by hydrogenating O-1 with an unpaired electron in the nitro group. We observed that this step is moderately exothermic (-50 kJ/mol) with an activation barrier of

58 kJ/mol. After the intermediate R-N(OH)$_2$* is formed, hydrogenolysis of the N-OH bond forms H_2O. The calculated true energy barrier of this step is 69 kJ/mol with an energy gain of 79 kJ/mol.

Considering that the formation of the first water molecule is highly exothermic, and it leaves intermediate unsaturated bonds on the surface, the following elementary steps are unlikely to be rate-limiting. Therefore, we only compare herein the energies of the first three hydrogenation steps. Figure 6. 8C shows that the reaction goes downhill step by step and that the overall energy barrier is 59 kJ/mol.[335, 336] It should be noted that the transition states for the first and second hydrogenation steps exhibit similar energies. To further determine the rate-limiting step, we conducted the maximum rate analyses on the first two hydrogenation elementary steps under experimentally relevant temperature and pressure conditions with entropy contribution included. The maximum rate analyses demonstrate that the first hydrogenation step has the lowest maximum rate, suggesting that this step is rate-limiting.

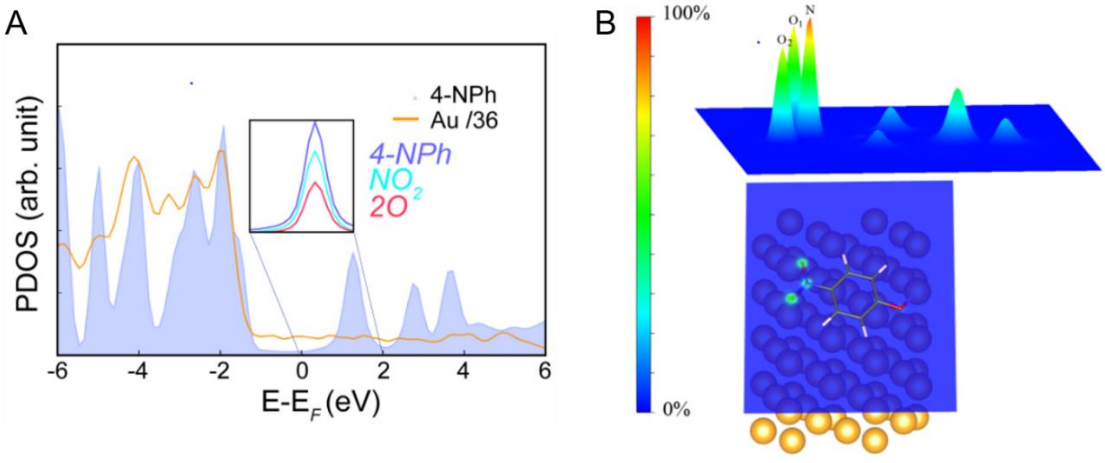

Figure 6. 10 Electronic structure of 4-nitrophenol on Au (111) surface. A. The calculated density of states projected on the 4-NPh molecule, Au, NO_2 moiety and two oxygen atoms in the NO_2 moiety. The zero energy corresponds to the Fermi level (E_F). The inset shows the PDOS of the NO_2 moiety and two oxygen atoms compared with the PDOS of 4-NPh showing that NO_2 group contributes largely to the frontier orbital of 4-NPh. The PDOS value of Au was reduced by 36 times to be comparable with the values of the other three parts. B. The spatial distribution of the molecular orbital that has the most charge contribution on the -NO_2 moiety: top view (bottom) and side view (top).

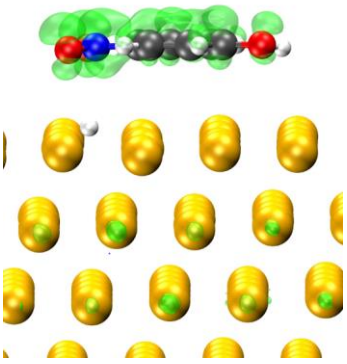

Figure 6. 11 The change in charge distribution due to the excitation. Green isosurface (0.003 $e/Å^{-3}$) represents more charge.

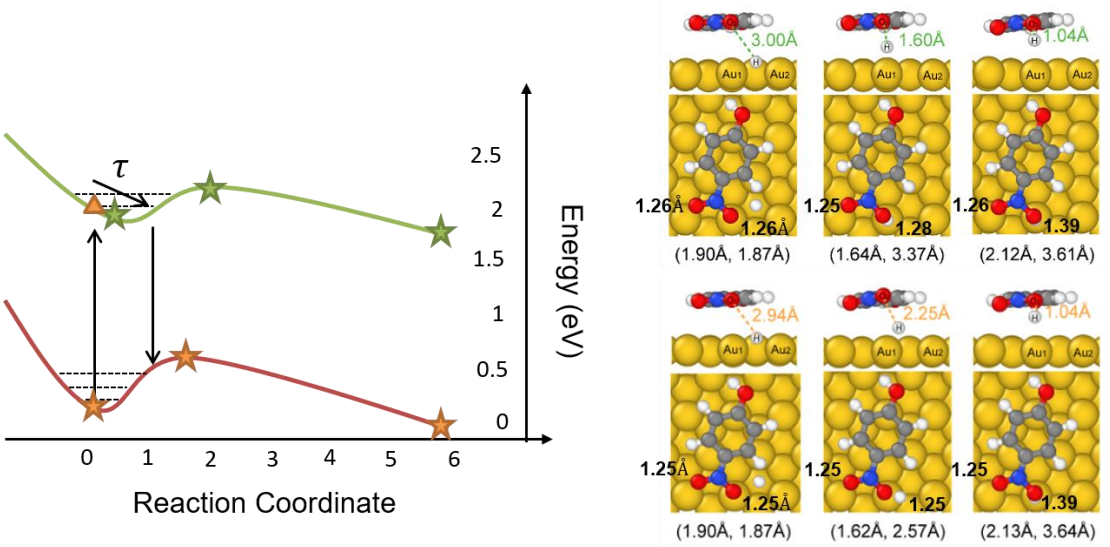

Figure 6. 12 Reaction profile of the first hydrogenation step in the reduction of 4-NPh on Au (111) surface at the ground state (orange curve) and with an electron adding to the NO2-dominant orbital (green curve). The values next to the molecule are bond lengths of N-O. The values in parentheses are $d_{Au1\text{-}H}$ and $d_{Au2\text{-}H}$, respectively. Stars represent the initial state, transition state, and final state of the rate-limiting step on the ground-state and excited-state potential energy surfaces. The vertical energy difference between orange triangle on the ground-state PES and star on the excited-state PES is the excitation energy.

6.2.5.3 Calculated potential energy surface at excited state

We first explore the molecular frontier orbitals that may be occupied by the excited electrons.[337] Figure 6. 10A shows the density of states (DOS) projected on Au, 4-NPh, the substituted nitro group, and the two oxygens in the nitro group, respectively. The DOS of pristine Au and 4-NPh are plotted in Appendix D. In Figure 6. 10A, the

hybridization between the metal substrate and 4-NPh makes the molecular orbitals less pronounced than them in the gas phase.

The desired excitations are identified by analysis of calculated electron orbitals, local densities of states, and charge densities. We then calculated and analyzed each Kohn Sham (KS) orbital ranging from the Fermi Energy (EF) to 2.33 eV and identified an energy level at 1.22 eV above the EF that has significant charge distribution on the NO_2-moiety. Since the LSPR peak of Au nanoparticles was found to locate at 532 nm (2.33 eV), if the reaction follows an indirect energy transfer mechanism, the collective electronic transition could lead to a wide distribution of hot electron from EF all the way to 2.33 eV with a narrow tail at higher energy levels.[75, 293] In principle, this is sufficient for electrons to access the targeted molecular orbital. Figure 6. 11 shows the change in charge between the resonance calculation and the ground-state calculation for the molecules coadsorption on the surface, indicating the charge not only occurs on the NPh molecule but also on the Au surface. It is worth mentioning that, at the occupied states in the DOS plot, there is strong hybridization between Au and the molecule, as a result of the dominant feature of Au d orbital and O p orbital in the energy range from -4 to -1 eV as referenced to the EF. Although there is weak hybridization between Au and 4-NPh in the unoccupied states, the available states of 64 Au atoms are still high with respect to the available states of 4-NPh.

In the next step, we examined the potential energy surface for the kinetically relevant step with an electron added to simulate the process under green light excitation. To find the excited-state potential energy surfaces, we use the method of delta self-consistent field method[148, 149] by manually positioning an electron in the aforementioned

NO_2-driven KS orbital and obtained the reaction profile of the first hydrogenation step, which is the hydrogen addition from surface to the O-2.

We compared the structures and energies of initial, final and transition states with and without an additional electron presenting. With an additional electron, there is an apparent displacement in the location of the ground state minimum (molecule adsorption) in the excited-state PES as compared to the ground state, indicating an electron hitting that could induce atomic motion in the system. This atomic motion may originate from the excited molecule having an extra electron in its antibonding orbital so it presents change in the equilibrium bond length of NO_2, see Figure 6.12. The estimated excitation energy is 1.8 eV (vertical excitation) following the equation outlined:

$$E_{excitation} = E_{ES} - E_{GS}$$

Where E_{GS} is obtained at ground state minimum, and E_{ES} is calculated self-consistently (with extra charge in the KS orbital but no relaxation) modeling the instantaneous restructuring of the electronic environment at the same vertical point. This effect can also be seen in the transition state along the excited PES that presents a late transition state feature, as it resembles the product R-NO(OH)*, showing that the transition state is stabilized with an additional electron. Meanwhile, if the reactant travels on the excited PES, the activation barrier of the rate-limiting step reduces from 0.49 to 0.21 eV. This result agrees qualitatively with our experimental findings that the catalytic activity of 4-NPh reduction to 4-APh on Au NPs is enhanced ~3 times under light,[328] considering the fact that entropy is not included in the calculations. On the other hand, given the fact that the resonance last on the time scale of femtoseconds, whereas the bond formation is on the picosecond scale, the resonance may decay before the bond formation. In this case,

the decay to ground state PES can deposit vibrational energy and optimally (consider one vibrate) reduce the energy barrier from 0.49 eV to 0.12 eV. The calculation indicates that the rate enhancements may be caused by hot electrons creating a transient negative ion to travel on the excited-state PES in the presence of light; in either way, the reactant overcomes a lower energy barrier along the excited-state PES forming the first intermediate R-NO(OH)*.

To determine if the activation barrier reduction is orbital selective, we tested other pronounced KS orbitals including the E_F and a molecular orbital dominated by the aromatic ring. In all cases, similar amounts of reduction in energy barrier were found (Table 8). To explain this insensitive orbital selectivity, the Bader charge analysis was performed.

When an extra electron was injected into the aforementioned NO_2-dominate orbital, we expected to see charge population on the reactant; however, we found 0.7e on the metal, and only 0.3e on the 4-NPh. This phenomenon was pointed out by Gacnholt et.al.[150] This charge delocalization is perhaps not surprising, because Au NPs have extended d orbitals, which overlaps with the adsorbate molecular frontier orbitals (Figure 6. 10A). Consequently, instead of being transferred to the molecule, excited electrons are trapped in the metal.

Table 8 The Bader charges of the initial state on Au (Q_{Au}) and 4-NPh (Q_{NPh}) with an extra electron added in three different orbitals (unit e). The charge distribution at ground state is also presented as reference. All the energies are in eV. Numbers in the parenthesis indicates the energy level as referenced to FL of each orbital (unit eV).

Orbitals	Activation barrier E_a	Reaction energy E_r	Q_{Au}	Q_{NPh}	Fermi energy
Without an extra electron	0.49	-0.22	-0.15	0.06	0.23
NO_2-driven (1.22)	0.21	-0.05	0.66	0.24	0.97
Fermi level (0)	0.25	-0.11	0.78	0.15	1.10
Ring (2.06)	0.21	-0.03	0.71	0.19	1.10

6.2.5.4 Calculated reaction profile of the decoupled 4-nitrophenol

To overcome the charge delocalization issue, which limits the charge that can be localized on the targeted molecular orbital, we propose here to cover the Au core with a thin layer of insulating material, such as hexagonal boron nitride (*h*-BN), and thus marrying a metal-free catalytic material with plasmonically-active light-absorbing antenna. The *h*-BN nanosheets possess band gaps close to 6 eV,[338, 339] which are insensitive to the thickness.[340] To explore the catalytic property of this prototype system, a carbon atom is employed as dopant on *h*-BN monolayer by replacing one of the N atoms with a C atom (CBN), which is a common type of defects in *h*-BN.[341] Introduction of the C is to anchor the hydrogen, which otherwise diffuses on the surface, to test the role of hot carriers in the same hydrogenation reaction.

We first compared the optimized structures of 4-NPh and H on the CBN surface. 4-NPh prefers to adsorb on CBN at a parallel adsorption mode to maximum the d-π interaction with two oxygen atoms being on top of the two corresponding boron atoms that are neighbors to the C atom (Figure 6. 13B). The adsorption energy is -65 kJ/mol, weaker than on Au. The O-1 is 3.25 Å from the surface B, and the distance between O-2 and the nearest B atom distance is 3.33 Å. As expected, H prefers to adsorb on the C

dopant on h-CBN surface with an adsorption energy of -177 kJ/mol, indicating a very strong chemisorption, mainly due to the unpaired electron in C.

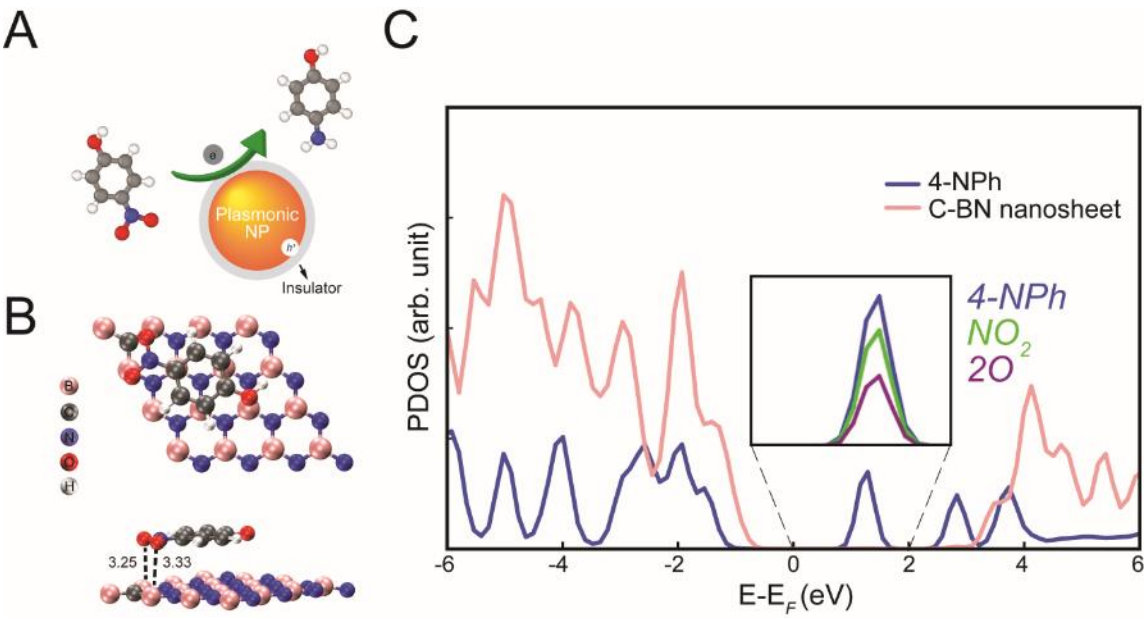

Figure 6. 13 DFT-estimated geometric and electronic structure of 4-NPh on CBN (001) surface. A. Schematic of the proposed Au@CBN core shell structure. B. DFT-simulated adsorption structures of a 4-NPh molecule on the CBN. C. Projected density of states of 4-NPh molecule, CBN surface, the NO_2 moiety and two oxygen atoms in the NO_2 moiety. The zero energy corresponds to the Fermi level (E_F). The inset shows the PDOS of the NO_2 and two oxygen atoms being compared with the PDOS of 4-NPh.

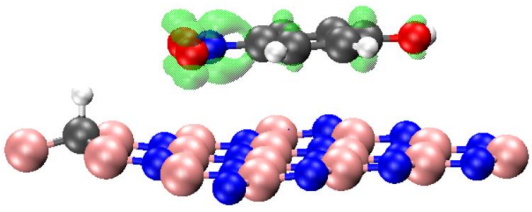

Figure 6. 14 The change in charge distribution due to the excitation. Green isosurface ($0.03\ e/Å^{-3}$) represents more charge.

Similarly, we investigated the electronic structure of 4-NPh adsorbed on CBN. To simplify the discussion, Au was not included in the model here, but we did test the electronic structure of 4-NPh adsorbed on CBN(001)/Au(111) and found the same conclusion (Appendix D Figure D. 9) CBN has less than 4 eV band gap energy (Figure D. 10), which is caused by the underestimation of the band gap in DFT calculation employing semi-local functions.[342] Regardless, as expected, there is no overlap between CBN and 4-NPh states in the energy window of E_F to 3 eV. In other words, with CBN as the substrate, the LUMO orbital of 4-NPh becomes decoupled and more localized. Meanwhile, we expect that the weak hybridization between CBN and 4-NPh extends lifetimes of excited electrons by preventing the electron-hole recombination in the metal NPs.[343, 344] This decoupled LUMO is also confirmed by the fact that the LUMO level of pure 4-NPh has similar shape in charge distribution compared to the LUMO of the adsorbed molecule (Figure D. 11). Excited electrons could tunnel from the plasmonic metal to the molecule through the thin insulator film,[345] that is in this case from the Au core to 4-NPh through the thin layer of CBN, under LSPR-induced local field enhancement at Au surface.[346]

We now compare the reaction profiles of the first hydrogenation step of 4-NPh reduction to 4-APh on the CBN surface. The calculations show this step is barrierless. The energy difference between the initial and final states is 1.87 eV at ground state, with negligible charge transfer between the molecule and the substrate (Table 9), indicating a

character of physisorption. According to the PDOS plots, we are able to identify an orbital with most charge localized on the NO_2 group, which is the LUMO orbital shown in Figure 6. 13B (the first peak above the E_F). Figure 6. 14 shows the change in charge between the resonance calculation and the ground-state calculation for the molecules coadsorption on the BN surface, indicating the charge only occurs on the NPh molecule, as opposed to on pure Au surface. With an additional electron in this orbital, the resultant reaction profile presents a significantly lower activation energy barrier (0.36 eV); the product R-NO(OH)* locates on top of the surface C, indicating that the reacting H travels a much shorter distance to adsorbed NPh (C-H bond length 3.08 Å vs 1.63 Å). The initial state stays at its adsorption site. Bader charge analysis on the initial state indicates additional 0.89e on the molecule, and only 0.11e on the substrate, distinct from the previous case where most electrons are located on the metal, and when no insulating material is inserted. Overall, it can be concluded that, by inserting a thin layer of CBN, more charge could be localized on the molecule, which facilitates the formation of an O-H bond.

We thus propose that a hybrid structure consisting of a plasmonic metal and a thin insulating film for driving bond formation and dissociation. In this hybrid complex, charge carriers can transfer indirectly by being excited in the metal NPs upon absorption, and then getting through the thin layer of an insulator[293] simultaneously through antenna's near-field amplification. The hot carriers may also be directly excited within the molecule or within the metal-molecule complex by the strong electric field at the interface. In either way, the hot carriers can occupy a targeted molecular orbital and enhance the kinetics of the rate-limiting step. The insulator plays a key role by localizing

electrons on the adsorbate to drive chemical reactions and increasing the lifetimes of the excited states sufficiently to induce the photo-association.

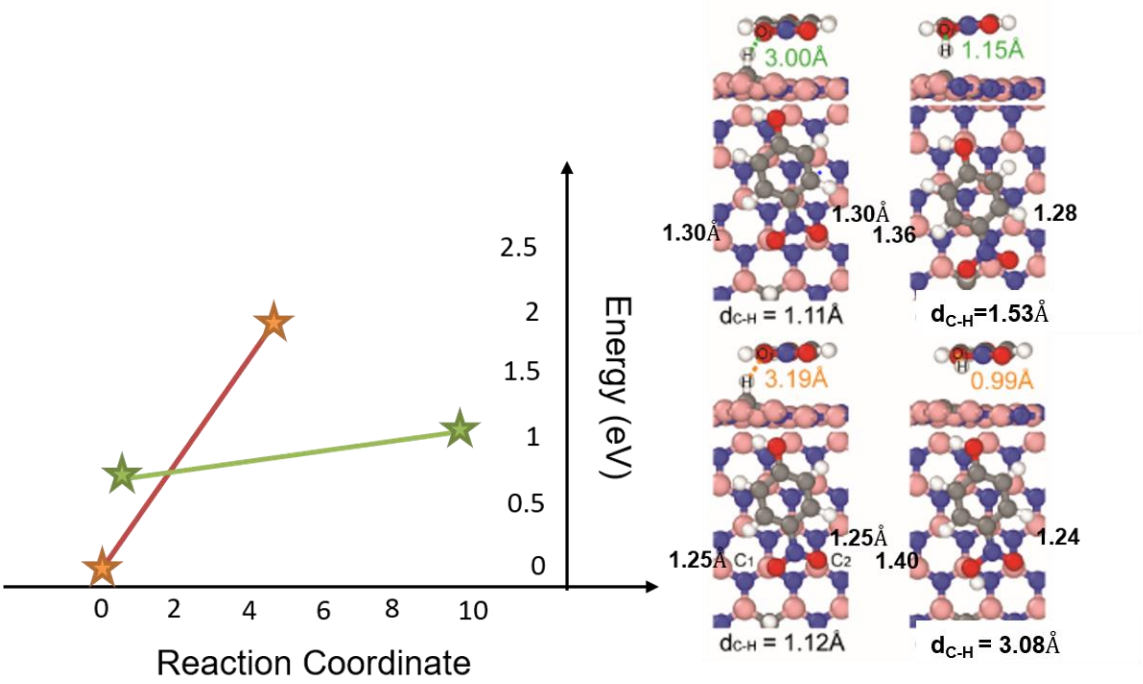

Figure 6. 15 Reaction profile of the first hydrogenation step in the reduction of 4-nitrophenol on CBN surface at ground state (orange curve) and with an electron adding to the NO_2-driven orbital (green curve). The initial and final configurations at ground state and excited state are shown.

Table 9 The Bader charges of the initial state on CBN (Q_{CBN}) and 4-NPh (Q_{NPh}) with an extra electron added in three different orbitals (unit e). The charge distribution at ground state is also presented as reference. All the energies are in eV. Numbers in the parenthesis indicates the energy level as referenced to FL of each orbital (unit eV).

Orbitals	$E_a=E_r$	Q_{CBN}	Q_{NPh}	Fermi energy
Without an extra electron	1.87	-0.05	-0.01	-1.26
NO_2-driven (1.58)	0.36	0.06	0.87	1.76
Ring (3.10)	1.82	0.40	0.50	0.38

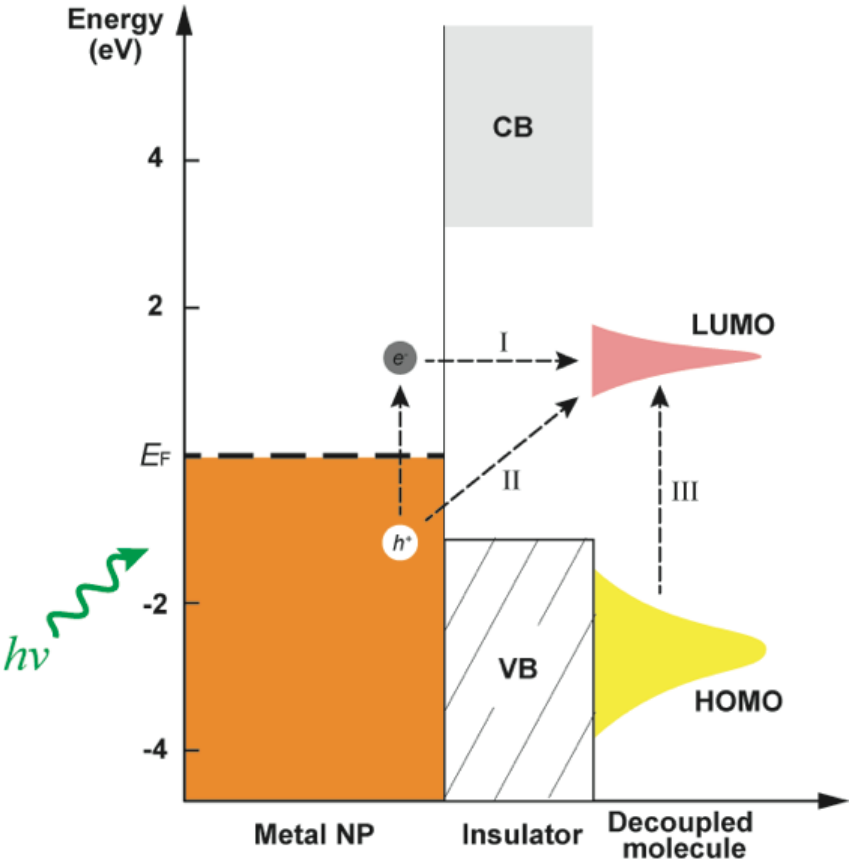

Figure 6. 16 The schematic plot of the proposed core-shell structure.

6.2.6 Conclusions

The LSPR-enhanced photocatalytic reduction reaction of 4-nitrophenol on supported Au surface was investigated through a combination of experimental and

theoretical work. Specially, the catalytic activity on supported Au catalyst with and without light irradiation was measured and higher reaction rate under light irradiation was observed. This was compared with the reaction energy profiles with and without excited electrons from density functional theory calculations. Our results suggest that hot electrons injected into the LUMO orbital lowers the activation barrier of the rate-limiting step. However, caused by the degeneracy of molecular frontier orbitals, it is challenging to ambiguously identify the role of hot electrons in lowering the energy barrier. Thus, we propose that, by inserting a thin layer of carbon-doped BN, the Au@h-CBN core shell structure is essential in localizing excited electrons on the adsorbate and facilitating the bond formation processes. We stress that the thin layer insulating material could have other candidates such as NaCl[347] and Cu_2N[348]. We believe our results shed new insights into the optimization of plasmonically enhanced chemical reactions and aids the future design of plasmonic catalyst structure.

Chapter 7. Conclusions and Future Directions

7.1 Dissertation Summary

This thesis focused on the understanding of hydrotreating processes as a promising route for a variety of applications: semiconductor manufacturing and heterogeneous catalytic processes. Herein, density functional theory method, in combination with its extensions, were employed as an approach to elucidate the essential role of hydrogen molecule by thoroughly investigating their thermodynamic and kinetics properties to ultimately optimize the performance of solar cell and photocatalytic systems. Throughout the study here, we attempted to bridge solar energy utilization with electrical and chemical energy production at ambient conditions.

The thesis begins with the discussion of several light-absorbing materials, quartnary alloy GaInNAs, two dimentional black phosphorene, as well as natural van der Waals heterostructure, all of which present potential optical properties for absorbing a certain wavelength range on the sunlight spectrum. Several factors such as bonding modes, organic ligand-surface interactions, functional groups and layer combinations have been taken into consideration to study materials property. A major topic of the first part is the nitrogen-related defects in dilute nitride material GaInNAs, which shows promising candidacy as the fourth junction in multijunction solar cells. In-related defects were studied systematically and compared with known Ga-related impurities. Thermodynamic study revealed that there is energy cost for hydrogen addition, the values vary with different bonding modes of the material. Importantly, hydrogen addition plays a crucial role in altering electronic properties of the material.

Hydrotreating processes in the field of heterogeneous catalysis were next explored on several supported metal catalysts, namely, Pd, Pt, Au. The hydrogenation activity of nonpolar and polar group in the selected model compounds was shown to depend largely on the metal. All the catalysts in this study were modeled by the close-packed 111 surfaces, which was shown to be the most stable facet of face-centered metal nanoparticles. From a kinetic prospective, changing hydrogen coverage is critical for possible enhancement of the reaction activity. Also, high hydrogen pressure allows phase transition from palladium to palladium hydride, which is possible to further facilitate hydrogen addition to the organic molecule.

In Chapter 6, a reaction pathway-dependent analysis was performed by employing two different hydrogen sources BH_4^- and H_2 in hydrogenation of a model compound with a polar NO_2 group. Although the same supported metal catalyst was utilized, the reaction proceeds via different paths by having different reducing agents. Specially, gold nanoparticle was employed as catalyst due to its inertness in H_2 splitting, which allows a further study of light-influenced hydrotreating process on top of its superior plasmonic property. This adds another complexity to the whole picture, since Au here serves as both plasmonically and catalytically active component. We compared conventional thermal reactions where heat is the primary energy source to drive the reaction with plasmonic reactions where charge carriers, through the application of light irradiation, is the energy source. In thermal reactions, the reaction happens on the ground state potential energy surface, which can be obtained with standard DFT calculations at 0 K. However, In the case of photocatalytic reactions, excited electrons have to be accounted for. Here delta SCF method was employed to model reaction on excited state potential energy surface.

We observed reduction in activation energy barrier of the kinetically relevant elementary step under resonant excitation. In order to decouple the molecular orbital from extended metal d states, a thin layer of insulator was added to further reduce the energy barrier as well as increase the carrier lifetime. The advantage of this plasmonic catalytic strategy includes low temperature and pressure (mostly at room conditions) and possibly selectivity towards desired product.

7.2 Future Directions

It is evident in Figure 3. 1a,b that a third feature is evident at lower energy (longer wavelength), E_{In}, at ~1.1 eV. Particularly at low temperatures, the narrowed width of E_{In} leads to a more pronounced feature in the PL spectra, though its overall contribution is similar at the various temperatures. Previously, lower-energy transitions have been attributed to N−N clusters and defects.[169] However, such large nitrogen-derived clusters could be selectively passivated by the hydrogenation process and almost completely removed from PL spectra at the levels of hydrogenation used here. In Figure 3. 1b, it appears that the hydrogenation process has little direct effect on the complexes that constitute this transition, such that its overall contribution to the PL does not appear to decrease significantly. Since the homogeneity of the system is improved and the contribution of defects and impurities is reduced, the resolution of E_{In} is improved, and its contribution to the emission is more clearly resolved. Thus, it is believed that that E_{In} is not associated with nitrogen-related defects but rather is tentatively attributed to the formation of small inclusions or phases of InAs, which are known to form in these systems.[187] While the emission energy of InAs QD-like centers is consistent with the peak observed, the effect

of hydrogen (or not) on such centers remains relatively unknown and is now currently under investigation.

Since E_{In} is relatively unaffected by temperature, also, the behavior of E_{In} is not affected by hydrogenation showing that E_{In} is not similar to In-related nor Ga-related impurities tackled in this thesis, which can be passivated via hydrotreating. The passivation of E_{In} should require a non-hydrogen process. So, the future research should be focused on investigating the nature and passivation of E_{In} related defects.

Organic compounds containing additional functional groups can be studied on Pd surface. Specially, hydrogenation of unsaturated aldehydes such as crotonaldehyde, cinnamaldehyde could be investigated on different metal surfaces to compare reaction selectivity. Factors such as H coverage, aldehyde coverage, solvent effect can all be taken into consideration to generate a complete picture of thermal activated reactions. For plasmonic catalysis, further analysis of charge transfer mechanism is needed. The realization of which may require utilizing methodologies beyond conventional DFT and GGA functionals to better describe excited state potential energy surface with moderate computation load. Techniques such as the embedding theory, linear-expansion delta SCF method, or real time time-dependent DFT might be desired. Secondly, hydrogenation of small molecules can be investigated so that molecular orbital overlap with metal extended orbitals may be reduced.

References

1. Chen, B.; Dingerdissen, U.; Krauter, J. G. E.; Rotgerink, H. G. J. L.; Möbus, K.; Ostgard, D. J.; Panster, P.; Riermeier, T. H.; Seebald, S.; Tacke, T., New developments in hydrogenation catalysis particularly in synthesis of fine and intermediate chemicals. *Applied Catalysis A: General* **2005,** *280* (1), 17-46.
2. Ertl, G.; Knözinger, H.; Weitkamp, J., Handbook of heterogeneous catalysis. **1997**.
3. Boudart, M., Heterogeneous catalysis by metals. *Journal of molecular catalysis* **1985,** *30* (1-2), 27-38.
4. Boudart, M., Catalysis by supported metals. In *Advances in catalysis*, Elsevier: 1969; Vol. 20, pp 153-166.
5. Erisman, J. W.; Sutton, M. A.; Galloway, J.; Klimont, Z.; Winiwarter, W., How a century of ammonia synthesis changed the world. *Nature Geoscience* **2008,** *1* (10), 636-639.
6. Yuan, Y.; Yao, S.; Wang, M.; Lou, S.; Yan, N., Recent progress in chemoselective hydrogenation of α, β-unsaturated aldehyde to unsaturated alcohol over nanomaterials. *Current Organic Chemistry* **2013,** *17* (4), 400-413.
7. Tomkins, P.; Ranocchiari, M.; van Bokhoven, J. A., Direct conversion of methane to methanol under mild conditions over Cu-zeolites and beyond. *Accounts of chemical research* **2017,** *50* (2), 418-425.
8. Lambert, C. K., Current state of the art and future needs for automotive exhaust catalysis. *Nature Catalysis* **2019,** *2* (7), 554-557.
9. Liu, H.; Song, C.; Zhang, L.; Zhang, J.; Wang, H.; Wilkinson, D. P., A review of anode catalysis in the direct methanol fuel cell. *Journal of Power Sources* **2006,** *155* (2), 95-110.
10. Liu, J.; Uhlman, M. B.; Montemore, M. M.; Trimpalis, A.; Giannakakis, G.; Shan, J.; Cao, S.; Hannagan, R. T.; Sykes, E. C. H.; Flytzani-Stephanopoulos, M., Integrated Catalysis-Surface Science-Theory Approach to Understand Selectivity in the Hydrogenation of 1-Hexyne to 1-Hexene on PdAu Single-Atom Alloy Catalysts. *ACS Catalysis* **2019,** *9* (9), 8757-8765.
11. Wang, A.; Li, J.; Zhang, T., Heterogeneous single-atom catalysis. *Nature Reviews Chemistry* **2018,** *2* (6), 65-81.
12. Boronat, M.; Leyva-Pérez, A.; Corma, A., Theoretical and experimental insights into the origin of the catalytic activity of subnanometric gold clusters: attempts to predict reactivity with clusters and nanoparticles of gold. *Accounts of chemical research* **2014,** *47* (3), 834-844.
13. Liu, L.; Corma, A., Metal catalysts for heterogeneous catalysis: from single atoms to nanoclusters and nanoparticles. *Chemical reviews* **2018,** *118* (10), 4981-5079.
14. Chinchilla, R.; Najera, C., Chemicals from alkynes with palladium catalysts. *Chemical reviews* **2014,** *114* (3), 1783-1826.
15. Saavedra, J.; Whittaker, T.; Chen, Z.; Pursell, C. J.; Rioux, R. M.; Chandler, B. D., Controlling activity and selectivity using water in the Au-catalysed preferential oxidation of CO in H 2. *Nature chemistry* **2016,** *8* (6), 584.

16. Grabow, L. C.; Gokhale, A. A.; Evans, S. T.; Dumesic, J. A.; Mavrikakis, M., Mechanism of the water gas shift reaction on Pt: First principles, experiments, and microkinetic modeling. *The Journal of Physical Chemistry C* **2008,** *112* (12), 4608-4617.
17. Anaya, F.; Resasco, D. E., Enhanced Fischer-Tropsch Synthesis Rates by the Combined Presence of Aqueous and Organic Media in Biphasic Systems. *ACS Catalysis* **2020**.
18. Hinrichsen, O.; Rosowski, F.; Hornung, A.; Muhler, M.; Ertl, G., The kinetics of ammonia synthesis over Ru-based catalysts: 1. The dissociative chemisorption and associative desorption of N2. *Journal of Catalysis* **1997,** *165* (1), 33-44.
19. Hammer, B.; Nørskov, J. K., Electronic factors determining the reactivity of metal surfaces. *Surface Science* **1995,** *343* (3), 211-220.
20. Nørskov, J. K., Catalysis—Calculations and Concepts. *Advances in Catalysis: Impact of surface science on catalysis* **2001,** *45*, 71.
21. Nørskov, J. K.; Bligaard, T.; Hvolbæk, B.; Abild-Pedersen, F.; Chorkendorff, I.; Christensen, C. H., The nature of the active site in heterogeneous metal catalysis. *Chemical Society Reviews* **2008,** *37* (10), 2163-2171.
22. Nørskov, J. K.; Rossmeisl, J.; Logadottir, A.; Lindqvist, L.; Kitchin, J. R.; Bligaard, T.; Jonsson, H., Origin of the overpotential for oxygen reduction at a fuel-cell cathode. *The Journal of Physical Chemistry B* **2004,** *108* (46), 17886-17892.
23. Medford, A. J.; Vojvodic, A.; Hummelshøj, J. S.; Voss, J.; Abild-Pedersen, F.; Studt, F.; Bligaard, T.; Nilsson, A.; Nørskov, J. K., From the Sabatier principle to a predictive theory of transition-metal heterogeneous catalysis. *Journal of Catalysis* **2015,** *328*, 36-42.
24. Crampton, A. S.; Rötzer, M. D.; Schweinberger, F. F.; Yoon, B.; Landman, U.; Heiz, U., Ethylene hydrogenation on supported Ni, Pd and Pt nanoparticles: Catalyst activity, deactivation and the d-band model. *Journal of Catalysis* **2016,** *333*, 51-58.
25. Marinelli, T.; Nabuurs, S.; Ponec, V., Activity and Selectivity in the Reactions of Substituted α, β-Unsaturated Aldehydes. *Journal of Catalysis* **1995,** *151* (2), 431-438.
26. Zaera, F., The surface chemistry of metal-based hydrogenation catalysis. *ACS Catalysis* **2017,** *7* (8), 4947-4967.
27. Mäki-Arvela, P.; Hájek, J.; Salmi, T.; Murzin, D. Y., Chemoselective hydrogenation of carbonyl compounds over heterogeneous catalysts. *Applied Catalysis A: General* **2005,** *292*, 1-49.
28. Singh, U. K.; Vannice, M. A., Kinetics of liquid-phase hydrogenation reactions over supported metal catalysts—a review. *Applied Catalysis A: General* **2001,** *213* (1), 1-24.
29. Ponec, V., On the role of promoters in hydrogenations on metals; α, β-unsaturated aldehydes and ketones. *Applied Catalysis A: General* **1997,** *149* (1), 27-48.
30. Lopez, N.; Łodziana, Z.; Illas, F.; Salmeron, M., When Langmuir is too simple: H 2 dissociation on Pd (111) at high coverage. *Physical review letters* **2004,** *93* (14), 146103.
31. Horiuti, I.; Polanyi, M., Exchange reactions of hydrogen on metallic catalysts. *Transactions of the Faraday Society* **1934,** *30*, 1164-1172.
32. Yang, B.; Gong, X.-Q.; Wang, H.-F.; Cao, X.-M.; Rooney, J. J.; Hu, P., Evidence to challenge the universality of the Horiuti–Polanyi mechanism for hydrogenation in heterogeneous catalysis: origin and trend of the preference of a non-

Horiuti–Polanyi mechanism. *Journal of the American Chemical Society* **2013,** *135* (40), 15244-15250.
33. Segura, Y.; López, N.; Pérez-Ramírez, J., Origin of the superior hydrogenation selectivity of gold nanoparticles in alkyne+ alkene mixtures: Triple-versus double-bond activation. *Journal of Catalysis* **2007,** *247* (2), 383-386.
34. Montoya, A.; Schlunke, A.; Haynes, B. S., Reaction of hydrogen with Ag (111): Binding states, minimum energy paths, and kinetics. *The Journal of Physical Chemistry B* **2006,** *110* (34), 17145-17154.
35. Lucci, F. R.; Darby, M. T.; Mattera, M. F. G.; Ivimey, C. J.; Therrien, A. J.; Michaelides, A.; Stamatakis, M.; Sykes, E. C. H., Controlling hydrogen activation, spillover, and desorption with Pd–Au single-atom alloys. *The journal of physical chemistry letters* **2016,** *7* (3), 480-485.
36. Spiewak, B. E.; Cortright, R. D.; Dumesic, J. A., Microcalorimetric studies of H2, C2H4, and C2H2adsorption on Pt powder. *Journal of Catalysis* **1998,** *176* (2), 405-414.
37. Bridier, B.; López, N.; Pérez-Ramírez, J., Partial hydrogenation of propyne over copper-based catalysts and comparison with nickel-based analogues. *Journal of Catalysis* **2010,** *269* (1), 80-92.
38. Watson, G. W.; Wells, R. P. K.; Willock, D. J.; Hutchings, G. J., A comparison of the adsorption and diffusion of hydrogen on the {111} surfaces of Ni, Pd, and Pt from density functional theory calculations. *The Journal of Physical Chemistry B* **2001,** *105* (21), 4889-4894.
39. Hu, B.; Ding, K.; Wu, T.; Zhou, X.; Fan, H.; Jiang, T.; Wang, Q.; Han, B., Shape controlled synthesis of palladium nanocrystals by combination of oleylamine and alkylammonium alkylcarbamate and their catalytic activity. *Chemical Communications* **2010,** *46* (45), 8552-8554.
40. Yarulin, A. E.; Crespo-Quesada, R. M.; Egorova, E. V.; Kiwi-Minsker, L. L., Structure sensitivity of selective acetylene hydrogenation over the catalysts with shape-controlled palladium nanoparticles. *Kinetics and Catalysis* **2012,** *53* (2), 253-261.
41. Kang, J. H.; Shin, E. W.; Kim, W. J.; Park, J. D.; Moon, S. H., Selective hydrogenation of acetylene on TiO2-added Pd catalysts. *Journal of catalysis* **2002,** *208* (2), 310-320.
42. Zhang, Y.; Diao, W.; Williams, C. T.; Monnier, J. R., Selective hydrogenation of acetylene in excess ethylene using Ag-and Au–Pd/SiO2 bimetallic catalysts prepared by electroless deposition. *Applied Catalysis A: General* **2014,** *469*, 419-426.
43. Studt, F.; Abild-Pedersen, F.; Bligaard, T.; Sørensen, R. Z.; Christensen, C. H.; Nørskov, J. K., Identification of non-precious metal alloy catalysts for selective hydrogenation of acetylene. *Science* **2008,** *320* (5881), 1320-1322.
44. Cao, Y.; Sui, Z.; Zhu, Y.; Zhou, X.; Chen, D., Selective hydrogenation of acetylene over Pd-In/Al2O3 catalyst: promotional effect of indium and composition-dependent performance. *ACS Catalysis* **2017,** *7* (11), 7835-7846.
45. Miegge, P.; Rousset, J. L.; Tardy, B.; Massardier, J.; Bertolini, J. C., Pd1Ni99 and Pd5Ni95: Pd surface segregation and reactivity for the hydrogenation of 1, 3-Butadiene. *Journal of Catalysis* **1994,** *149* (2), 404-413.

46. McCue, A. J.; McRitchie, C. J.; Shepherd, A. M.; Anderson, J. A., Cu/Al2O3 catalysts modified with Pd for selective acetylene hydrogenation. *Journal of catalysis* **2014,** *319*, 127-135.
47. Coq, B.; Figueras, F., Bimetallic palladium catalysts: influence of the co-metal on the catalyst performance. *Journal of Molecular Catalysis A: Chemical* **2001,** *173* (1-2), 117-134.
48. Huang, D. C.; Chang, K. H.; Pong, W. F.; Tseng, P. K.; Hung, K. J.; Huang, W. F., Effect of Ag-promotion on Pd catalysts by XANES. *Catalysis letters* **1998,** *53* (3-4), 155-159.
49. Sheth, P. A.; Neurock, M.; Smith, C. M., First-Principles Analysis of the Effects of Alloying Pd with Ag for the Catalytic Hydrogenation of Acetylene− Ethylene Mixtures. *The Journal of Physical Chemistry B* **2005,** *109* (25), 12449-12466.
50. Rosi, N. L.; Eckert, J.; Eddaoudi, M.; Vodak, D. T.; Kim, J.; O'Keeffe, M.; Yaghi, O. M., Hydrogen storage in microporous metal-organic frameworks. *Science* **2003,** *300* (5622), 1127-1129.
51. Sheth, P. A.; Neurock, M.; Smith, C. M., A first-principles analysis of acetylene hydrogenation over Pd (111). *The Journal of Physical Chemistry B* **2003,** *107* (9), 2009-2017.
52. Teschner, D.; Borsodi, J.; Wootsch, A.; Révay, Z.; Hävecker, M.; Knop-Gericke, A.; Jackson, S. D.; Schlögl, R., The roles of subsurface carbon and hydrogen in palladium-catalyzed alkyne hydrogenation. *Science* **2008,** *320* (5872), 86-89.
53. Zhang, Q.; Li, J.; Liu, X.; Zhu, Q., Synergetic effect of Pd and Ag dispersed on Al2O3 in the selective hydrogenation of acetylene. *Applied Catalysis A: General* **2000,** *197* (2), 221-228.
54. Gillespie, L. J.; Galstaun, L. S., The Palladium-Hydrogen Equilibrium and New Palladium Hydrides1. *Journal of the American Chemical Society* **1936,** *58* (12), 2565-2573.
55. Vaidya, P. D.; Mahajani, V. V., Kinetics of liquid-phase hydrogenation of furfuraldehyde to furfuryl alcohol over a Pt/C catalyst. *Industrial & engineering chemistry research* **2003,** *42* (17), 3881-3885.
56. Koo-amornpattana, W.; Winterbottom, J. M., Pt and Pt-alloy catalysts and their properties for the liquid-phase hydrogenation of cinnamaldehyde. *Catalysis today* **2001,** *66* (2-4), 277-287.
57. Loffreda, D.; Delbecq, F.; Vigné, F.; Sautet, P., Catalytic hydrogenation of unsaturated aldehydes on Pt (111): understanding the selectivity from first-principles calculations. *Angewandte Chemie International Edition* **2005,** *44* (33), 5279-5282.
58. Lashdaf, M.; Krause, A. O. I.; Lindblad, M.; Tiitta, M.; Venäläinen, T., Behaviour of palladium and ruthenium catalysts on alumina and silica prepared by gas and liquid phase deposition in cinnamaldehyde hydrogenation. *Applied Catalysis A: General* **2003,** *241* (1-2), 65-75.
59. Scheler, T.; Degtyareva, O.; Marqués, M.; Guillaume, C. L.; Proctor, J. E.; Evans, S.; Gregoryanz, E., Synthesis and properties of platinum hydride. *Physical Review B* **2011,** *83* (21), 214106.
60. Hammer, B.; Norskov, J. K., Why gold is the noblest of all the metals. *Nature* **1995,** *376* (6537), 238-240.

61. Haruta, M.; Daté, M., Advances in the catalysis of Au nanoparticles. *Applied Catalysis A: General* **2001,** *222* (1-2), 427-437.
62. Mohr, C.; Claus, P., Hydrogenation properties of supported nanosized gold particles. *Science progress* **2001,** *84* (4), 311-334.
63. Pan, M.; Pozun, Z. D.; Yu, W.-Y.; Henkelman, G.; Mullins, C. B., Structure revealing H/D exchange with co-adsorbed hydrogen and water on gold. *The journal of physical chemistry letters* **2012,** *3* (14), 1894-1899.
64. Pan, M.; Brush, A. J.; Pozun, Z. D.; Ham, H. C.; Yu, W.-Y.; Henkelman, G.; Hwang, G. S.; Mullins, C. B., Model studies of heterogeneous catalytic hydrogenation reactions with gold. *Chemical Society Reviews* **2013,** *42* (12), 5002-5013.
65. Albrecht, G.; Ubl, M.; Kaiser, S.; Giessen, H.; Hentschel, M., Comprehensive study of plasmonic materials in the visible and near-infrared: linear, refractory, and nonlinear optical properties. *Acs Photonics* **2018,** *5* (3), 1058-1067.
66. Zhang, Y.; He, S.; Guo, W.; Hu, Y.; Huang, J.; Mulcahy, J. R.; Wei, W. D., Surface-plasmon-driven hot electron photochemistry. *Chemical reviews* **2017,** *118* (6), 2927-2954.
67. Brongersma, M. L.; Halas, N. J.; Nordlander, P., Plasmon-induced hot carrier science and technology. *Nature nanotechnology* **2015,** *10* (1), 25.
68. Aslam, U.; Rao, V. G.; Chavez, S.; Linic, S., Catalytic conversion of solar to chemical energy on plasmonic metal nanostructures. *Nature Catalysis* **2018,** *1* (9), 656-665.
69. Kim, C.; Lee, H., Light-assisted surface reactions on metal nanoparticles. *Catalysis Science & Technology* **2018,** *8* (15), 3718-3727.
70. Link, S.; El-Sayed, M. A., Spectral properties and relaxation dynamics of surface plasmon electronic oscillations in gold and silver nanodots and nanorods. ACS Publications: 1999.
71. El-Sayed, M. A., Some interesting properties of metals confined in time and nanometer space of different shapes. *Accounts of chemical research* **2001,** *34* (4), 257-264.
72. Manjavacas, A.; Liu, J. G.; Kulkarni, V.; Nordlander, P., Plasmon-induced hot carriers in metallic nanoparticles. *ACS nano* **2014,** *8* (8), 7630-7638.
73. Frischkorn, C.; Wolf, M., Femtochemistry at metal surfaces: nonadiabatic reaction dynamics. *Chemical reviews* **2006,** *106* (10), 4207-4233.
74. Thrall, E. S.; Preska Steinberg, A.; Wu, X.; Brus, L. E., The role of photon energy and semiconductor substrate in the plasmon-mediated photooxidation of citrate by silver nanoparticles. *The Journal of Physical Chemistry C* **2013,** *117* (49), 26238-26247.
75. Mukherjee, S.; Libisch, F.; Large, N.; Neumann, O.; Brown, L. V.; Cheng, J.; Lassiter, J. B.; Carter, E. A.; Nordlander, P.; Halas, N. J., Hot electrons do the impossible: plasmon-induced dissociation of H2 on Au. *Nano letters* **2013,** *13* (1), 240-247.
76. Boerigter, C.; Campana, R.; Morabito, M.; Linic, S., Evidence and implications of direct charge excitation as the dominant mechanism in plasmon-mediated photocatalysis. *Nature communications* **2016,** *7* (1), 1-9.
77. Boerigter, C.; Aslam, U.; Linic, S., Mechanism of charge transfer from plasmonic nanostructures to chemically attached materials. *ACS nano* **2016,** *10* (6), 6108-6115.

78. Lindstrom, C. D.; Zhu, X. Y., Photoinduced electron transfer at molecule− metal interfaces. *Chemical reviews* **2006,** *106* (10), 4281-4300.
79. Jia, C.; Li, X.; Xin, N.; Gong, Y.; Guan, J.; Meng, L.; Meng, S.; Guo, X., Interface‐Engineered Plasmonics in Metal/Semiconductor Heterostructures. *Advanced Energy Materials* **2016,** *6* (17), 1600431.
80. Clavero, C., Plasmon-induced hot-electron generation at nanoparticle/metal-oxide interfaces for photovoltaic and photocatalytic devices. *Nature Photonics* **2014,** *8* (2), 95.
81. Martirez, J. M. P.; Carter, E. A., Excited-state N2 dissociation pathway on Fe-functionalized Au. *Journal of the American Chemical Society* **2017,** *139* (12), 4390-4398.
82. Martirez, J. M. P.; Carter, E. A., Prediction of a low-temperature N2 dissociation catalyst exploiting near-IR–to–visible light nanoplasmonics. *Science advances* **2017,** *3* (12), eaao4710.
83. Mukherjee, S.; Zhou, L.; Goodman, A. M.; Large, N.; Ayala-Orozco, C.; Zhang, Y.; Nordlander, P.; Halas, N. J., Hot-electron-induced dissociation of H2 on gold nanoparticles supported on SiO2. *Journal of the American Chemical Society* **2014,** *136* (1), 64-67.
84. Zhou, L.; Swearer, D. F.; Zhang, C.; Robatjazi, H.; Zhao, H.; Henderson, L.; Dong, L.; Christopher, P.; Carter, E. A.; Nordlander, P., Quantifying hot carrier and thermal contributions in plasmonic photocatalysis. *Science* **2018,** *362* (6410), 69-72.
85. Cortés, E.; Xie, W.; Cambiasso, J.; Jermyn, A. S.; Sundararaman, R.; Narang, P.; Schlücker, S.; Maier, S. A., Plasmonic hot electron transport drives nano-localized chemistry. *Nature communications* **2017,** *8* (1), 1-10.
86. Xiao, Q.; Sarina, S.; Waclawik, E. R.; Jia, J.; Chang, J.; Riches, J. D.; Wu, H.; Zheng, Z.; Zhu, H., Alloying gold with copper makes for a highly selective visible-light photocatalyst for the reduction of nitroaromatics to anilines. *ACS Catalysis* **2016,** *6* (3), 1744-1753.
87. Zhang, Q.; Jin, X.; Xu, Z.; Zhang, J.; Rendón, U. F.; Razzari, L.; Chaker, M.; Ma, D., Plasmonic Au-loaded hierarchical hollow Porous TiO2 spheres: Synergistic catalysts for nitroaromatic reduction. *The journal of physical chemistry letters* **2018,** *9* (18), 5317-5326.
88. Kelly, K. L.; Coronado, E.; Zhao, L. L.; Schatz, G. C., The optical properties of metal nanoparticles: the influence of size, shape, and dielectric environment. ACS Publications: 2003.
89. Linic, S.; Christopher, P.; Ingram, D. B., Plasmonic-metal nanostructures for efficient conversion of solar to chemical energy. *Nature materials* **2011,** *10* (12), 911-921.
90. Kale, M. J.; Avanesian, T.; Xin, H.; Yan, J.; Christopher, P., Controlling catalytic selectivity on metal nanoparticles by direct photoexcitation of adsorbate–metal bonds. *Nano letters* **2014,** *14* (9), 5405-5412.
91. Quiroz, J.; Barbosa, E. C. M.; Araujo, T. P.; Fiorio, J. L.; Wang, Y.-C.; Zou, Y.-C.; Mou, T.; Alves, T. V.; de Oliveira, D. C.; Wang, B., Controlling reaction selectivity over hybrid plasmonic nanocatalysts. *Nano letters* **2018,** *18* (11), 7289-7297.
92. Jain, P. K.; Lee, K. S.; El-Sayed, I. H.; El-Sayed, M. A., Calculated absorption and scattering properties of gold nanoparticles of different size, shape, and composition: applications in biological imaging and biomedicine. *The journal of physical chemistry B* **2006,** *110* (14), 7238-7248.

93. McEvoy, A.; Markvart, T., *Solar cells: materials, manufacture and operation*. Academic Press: 2012.
94. Sharma, S.; Jain, K. K.; Sharma, A., Solar cells: in research and applications—a review. *Materials Sciences and Applications* **2015,** *6* (12), 1145.
95. Green, M. A.; Dunlop, E. D.; Levi, D. H.; Hohl-Ebinger, J.; Yoshita, M.; Ho-Baillie, A. W. Y., Solar cell efficiency tables (version 54). *Progress in Photovoltaics: Research and Applications* **2019,** *27* (7), 565-575.
96. Nayak, P. K.; Mahesh, S.; Snaith, H. J.; Cahen, D., Photovoltaic solar cell technologies: analysing the state of the art. *Nature Reviews Materials* **2019,** *4* (4), 269.
97. Choubey, P. C.; Oudhia, A.; Dewangan, R., A review: Solar cell current scenario and future trends. *Recent Research in Science and Technology* **2012,** *4* (8).
98. Posorski, R.; Bussmann, M.; Menke, C., Does the use of Solar Home Systems (SHS) contribute to climate protection? *Renewable Energy* **2003,** *28* (7), 1061-1080.
99. Seboldt, W.; Klimke, M.; Leipold, M.; Hanowski, N., European sail tower SPS concept. *Acta Astronautica* **2001,** *48* (5-12), 785-792.
100. Lamei, A.; Van der Zaag, P.; Von Muench, E., Impact of solar energy cost on water production cost of seawater desalination plants in Egypt. *Energy policy* **2008,** *36* (5), 1748-1756.
101. Weiner, D.; Fisher, D.; Moses, E. J.; Katz, B.; Meron, G., Operation experience of a solar-and wind-powered desalination demonstration plant. *Desalination* **2001,** *137* (1-3), 7-13.
102. Meah, K.; Ula, S.; Barrett, S., Solar photovoltaic water pumping—opportunities and challenges. *Renewable and Sustainable Energy Reviews* **2008,** *12* (4), 1162-1175.
103. Chandratilleke, T. T.; Ho, J. C., A study of a photovoltaic array for water pumping. *Solar & wind technology* **1986,** *3* (1), 59-71.
104. Badescu, V., Time dependent model of a complex PV water pumping system. *Renewable Energy* **2003,** *28* (4), 543-560.
105. Zhao, J.; Wang, A.; Green, M. A.; Ferrazza, F., 19.8% efficient "honeycomb" textured multicrystalline and 24.4% monocrystalline silicon solar cells. *Applied Physics Letters* **1998,** *73* (14), 1991-1993.
106. Chapin, D. M.; Fuller, C. S.; Pearson, G. L., A new silicon p-n junction photocell for converting solar radiation into electrical power. *Journal of Applied Physics* **1954,** *25* (5), 676-677.
107. Schultz, O.; Glunz, S. W.; Willeke, G. P., ACCELERATED PUBLICATION: Multicrystalline silicon solar cells exceeding 20% efficiency. *Progress in Photovoltaics: Research and Applications* **2004,** *12* (7), 553-558.
108. Gobat, A. R.; Lamorte, M. F.; McIver, G. W., Characteristics of high-conversion-efficiency gallium-arsenide solar cells. *IRE Transactions on military electronics* **1962,** (1), 20-27.
109. Li, B.; Wang, L.; Kang, B.; Wang, P.; Qiu, Y., Review of recent progress in solid-state dye-sensitized solar cells. *Solar energy materials and solar cells* **2006,** *90* (5), 549-573.
110. Wudl, F.; Srdanov, G., Conducting polymer formed of poly (2-methoxy, 5-(2'-ethyl-hexyloxy)-p-phenylenevinylene). Google Patents: 1993.
111. Li, G.; Zhu, R.; Yang, Y., Polymer solar cells. *Nature photonics* **2012,** *6* (3), 153.

112. Wang, R.; Mujahid, M.; Duan, Y.; Wang, Z. K.; Xue, J.; Yang, Y., A review of perovskites solar cell stability. *Advanced Functional Materials* **2019,** *29* (47), 1808843.
113. Shockley, W.; Queisser, H. J., Detailed balance limit of efficiency of p-n junction solar cells. *Journal of applied physics* **1961,** *32* (3), 510-519.
114. Andreev, V. M., GaAs and High-Efficiency Space Cells. In *McEvoy's Handbook of Photovoltaics*, Elsevier: 2018; pp 421-438.
115. Shvarts, M. Z.; Chosta, O. I.; Kochnev, I. V.; Lantratov, V. M.; Andreev, V. M., Radiation resistant AlGaAs/GaAs concentrator solar cells with internal Bragg reflector. *Solar energy materials and solar cells* **2001,** *68* (1), 105-122.
116. Gokcen, N. A.; Loferski, J. J., Efficiency of tandem solar cell systems as a function of temperature and solar energy concentration ratio. *Solar Energy Materials* **1979,** *1* (3-4), 271-286.
117. Dimroth, F.; Kurtz, S., High-efficiency multijunction solar cells. *MRS bulletin* **2007,** *32* (3), 230-235.
118. Miles, R. W.; Hynes, K. M.; Forbes, I., Photovoltaic solar cells: An overview of state-of-the-art cell development and environmental issues. *Progress in crystal growth and characterization of materials* **2005,** *51* (1-3), 1-42.
119. Luque, A.; Hegedus, S., *Handbook of photovoltaic science and engineering*. John Wiley & Sons: 2011.
120. Christensen, C. H.; Nørskov, J. K., A molecular view of heterogeneous catalysis. *The Journal of chemical physics* **2008,** *128* (18), 182503.
121. Kohn, W.; Sham, L. J., Self-consistent equations including exchange and correlation effects. *Physical review* **1965,** *140* (4A), A1133.
122. Hohenberg, P.; Kohn, W., Inhomogeneous electron gas. *Physical review* **1964,** *136* (3B), B864.
123. Perdew, J. P.; Ruzsinszky, A.; Tao, J.; Staroverov, V. N.; Scuseria, G. E.; Csonka, G. I., Prescription for the design and selection of density functional approximations: More constraint satisfaction with fewer fits. *The Journal of chemical physics* **2005,** *123* (6), 062201.
124. Perdew, J. P.; Burke, K.; Ernzerhof, M., Generalized gradient approximation made simple. *Physical review letters* **1996,** *77* (18), 3865.
125. Perdew, J. P.; Chevary, J. A.; Vosko, S. H.; Jackson, K. A.; Pederson, M. R.; Singh, D. J.; Fiolhais, C., Atoms, molecules, solids, and surfaces: Applications of the generalized gradient approximation for exchange and correlation. *Physical review B* **1992,** *46* (11), 6671.
126. Zhang, Y.; Yang, W., Comment on "Generalized gradient approximation made simple". *Physical Review Letters* **1998,** *80* (4), 890.
127. Hammer, B.; Hansen, L. B.; Nørskov, J. K., Improved adsorption energetics within density-functional theory using revised Perdew-Burke-Ernzerhof functionals. *Physical review B* **1999,** *59* (11), 7413.
128. Vogiatzis, K. D.; Polynski, M. V.; Kirkland, J. K.; Townsend, J.; Hashemi, A.; Liu, C.; Pidko, E. A., Computational approach to molecular catalysis by 3d transition metals: Challenges and opportunities. *Chemical reviews* **2018,** *119* (4), 2453-2523.
129. Lee, C.; Yang, W.; Parr, R. G., Development of the Colle-Salvetti correlation-energy formula into a functional of the electron density. *Physical review B* **1988,** *37* (2), 785.

130. Becke, A. D., Density-functional thermochemistry. III. The role of exact exchange. *The Journal of Chemical Physics* **1993,** *98* (7), 5648-5652.
131. Heyd, J.; Scuseria, G. E.; Ernzerhof, M., Hybrid functionals based on a screened Coulomb potential. *The Journal of chemical physics* **2003,** *118* (18), 8207-8215.
132. Adamo, C.; Barone, V., Toward reliable density functional methods without adjustable parameters: The PBE0 model. *The Journal of chemical physics* **1999,** *110* (13), 6158-6170.
133. Zhao, Y.; Truhlar, D. G., The M06 suite of density functionals for main group thermochemistry, thermochemical kinetics, noncovalent interactions, excited states, and transition elements: two new functionals and systematic testing of four M06-class functionals and 12 other functionals. *Theoretical Chemistry Accounts* **2008,** *120* (1-3), 215-241.
134. Liechtenstein, A. I.; Anisimov, V. I.; Zaanen, J., Density-functional theory and strong interactions: Orbital ordering in Mott-Hubbard insulators. *Physical Review B* **1995,** *52* (8), R5467.
135. Anisimov, V. I.; Zaanen, J.; Andersen, O. K., Band theory and Mott insulators: Hubbard U instead of Stoner I. *Physical Review B* **1991,** *44* (3), 943.
136. Grimme, S., Semiempirical GGA-type density functional constructed with a long-range dispersion correction. *Journal of computational chemistry* **2006,** *27* (15), 1787-1799.
137. Grimme, S.; Antony, J.; Ehrlich, S.; Krieg, H., A consistent and accurate ab initio parametrization of density functional dispersion correction (DFT-D) for the 94 elements H-Pu. *The Journal of chemical physics* **2010,** *132* (15), 154104.
138. Dion, M.; Rydberg, H.; Schröder, E.; Langreth, D. C.; Lundqvist, B. I., Van der Waals density functional for general geometries. *Physical review letters* **2004,** *92* (24), 246401.
139. Lee, K.; Murray, É. D.; Kong, L.; Lundqvist, B. I.; Langreth, D. C., Higher-accuracy van der Waals density functional. *Physical Review B* **2010,** *82* (8), 081101.
140. Klimeš, J.; Bowler, D. R.; Michaelides, A., Chemical accuracy for the van der Waals density functional. *Journal of Physics: Condensed Matter* **2009,** *22* (2), 022201.
141. Klimeš, J.; Bowler, D. R.; Michaelides, A., Van der Waals density functionals applied to solids. *Physical Review B* **2011,** *83* (19), 195131.
142. Henkelman, G.; Uberuaga, B. P.; Jónsson, H., A climbing image nudged elastic band method for finding saddle points and minimum energy paths. *The Journal of chemical physics* **2000,** *113* (22), 9901-9904.
143. Henkelman, G.; Jónsson, H., A dimer method for finding saddle points on high dimensional potential surfaces using only first derivatives. *The Journal of chemical physics* **1999,** *111* (15), 7010-7022.
144. Huang, L.-y.; Lambrecht, W. R. L., Electronic band structure trends of perovskite halides: Beyond Pb and Sn to Ge and Si. *Physical Review B* **2016,** *93* (19), 195211.
145. Runge, E.; Gross, E. K. U., Density-functional theory for time-dependent systems. *Physical Review Letters* **1984,** *52* (12), 997.
146. Wu, Q.; Van Voorhis, T., Direct optimization method to study constrained systems within density-functional theory. *Physical Review A* **2005,** *72* (2), 024502.

147. Wu, Q.; Van Voorhis, T., Direct calculation of electron transfer parameters through constrained density functional theory. *The Journal of Physical Chemistry A* **2006,** *110* (29), 9212-9218.
148. Jones, R. O.; Gunnarsson, O., The density functional formalism, its applications and prospects. *Reviews of Modern Physics* **1989,** *61* (3), 689.
149. Hellman, A.; Razaznejad, B.; Lundqvist, B. I., Potential-energy surfaces for excited states in extended systems. *The Journal of chemical physics* **2004,** *120* (10), 4593-4602.
150. Gavnholt, J.; Olsen, T.; Engelund, M.; Schiøtz, J., Δ self-consistent field method to obtain potential energy surfaces of excited molecules on surfaces. *Physical Review B* **2008,** *78* (7), 075441.
151. Olsen, T.; Gavnholt, J.; Schiøtz, J., Hot-electron-mediated desorption rates calculated from excited-state potential energy surfaces. *Physical Review B* **2009,** *79* (3), 035403.
152. Klüner, T.; Govind, N.; Wang, Y. A.; Carter, E. A., Periodic density functional embedding theory for complete active space self-consistent field and configuration interaction calculations: Ground and excited states. *The Journal of chemical physics* **2002,** *116* (1), 42-54.
153. Essig, S.; Allebe, C.; Remo, T.; Geisz, J. F.; Steiner, M. A.; Horowitz, K.; Barraud, L.; Ward, J. S.; Schnabel, M.; Descoeudres, A.; Young, D. L.; Woodhouse, M.; Despeisse, M.; Ballif, C.; Tamboli, A., Raising the one-sun conversion efficiency of III-V/Si solar cells to 32.8% for two junctions and 35.9% for three junctions. *Nat Energy* **2017,** *2* (9), 17144.
154. King, R.; Law, D.; Edmondson, K.; Fetzer, C.; Kinsey, G.; Yoon, H.; Sherif, R.; Karam, N., 40% efficient metamorphic GaInP／GaInAs／Ge multijunction solar cells. *Applied physics letters* **2007,** *90* (18), 183516.
155. Dimroth, F.; Grave, M.; Beutel, P.; Fiedeler, U.; Karcher, C.; Tibbits, T. N.; Oliva, E.; Siefer, G.; Schachtner, M.; Wekkeli, A., Wafer bonded four‐junction GaInP/GaAs//GaInAsP/GaInAs concentrator solar cells with 44.7% efficiency. *Progress in Photovoltaics: Research and Applications* **2014,** *22* (3), 277-282.
156. Green, M. A.; Emery, K.; Hishikawa, Y.; Warta, W., Solar cell efficiency tables (version 37). *Progress in photovoltaics: research and applications* **2011,** *19* (1), 84-92.
157. Kurtz, S. R.; Myers, D.; Olson, J. M. In *Projected performance of three-and four-junction devices using GaAs and GaInP*, Photovoltaic Specialists Conference, 1997., Conference Record of the Twenty-Sixth IEEE, IEEE: 1997; pp 875-878.
158. O'Reilly, E.; Lindsay, A.; Klar, P.; Polimeni, A.; Capizzi, M., Trends in the electronic structure of dilute nitride alloys. *Semiconductor Science and Technology* **2009,** *24* (3), 033001.
159. Kurtz, S.; Webb, J.; Gedvilas, L.; Friedman, D.; Geisz, J.; Olson, J.; King, R.; Joslin, D.; Karam, N., Structural changes during annealing of GaInAsN. *Applied Physics Letters* **2001,** *78* (6), 748-750.
160. Xin, H.; Tu, C.; Geva, M., Annealing behavior of p-type Ga 0.892 In 0.108 N x As 1− x (0⩽ X⩽ 0.024) grown by gas-source molecular beam epitaxy. *Applied physics letters* **1999,** *75* (10), 1416-1418.

161. Rosenow, P.; Bannow, L. C.; Fischer, E. W.; Stolz, W.; Volz, K.; Koch, S. W.; Tonner, R., Ab initio calculations of the concentration dependent band gap reduction in dilute nitrides. *Physical Review B* **2018,** *97* (7), 075201.
162. Polojarvi, V.; Aho, A.; Tukiainen, A.; Raappana, M.; Aho, T.; Schramm, A.; Guina, M., Influence of As/group-III flux ratio on defects formation and photovoltaic performance of GaInNAs solar cells. *Solar Energy Materials and Solar Cells* **2016,** *149*, 213-220.
163. Aho, A.; Polojarvi, V.; Korpijarvi, V. M.; Salmi, J.; Tukiainen, A.; Laukkanen, P.; Guina, M., Composition dependent growth dynamics in molecular beam epitaxy of GaInNAs solar cells. *Solar Energy Materials and Solar Cells* **2014,** *124*, 150-158.
164. Weyers, M.; Sato, M.; Ando, H., Red shift of photoluminescence and absorption in dilute GaAsN alloy layers. *Japanese Journal of Applied Physics* **1992,** *31* (7A), L853.
165. Pashartis, C.; Rubel, O., Localization of Electronic States in III-V Semiconductor Alloys: A Comparative Study. *Phys Rev Appl* **2017,** *7* (6), 064011.
166. Polimeni, A.; Bissiri, H.; Capizzi, M.; Fischer, M.; Reinhardt, M.; Forchel, A., Effect of hydrogen on the electronic properties of In x Ga 1− x As 1− y N y/GaAs quantum wells. *Physical Review B* **2001,** *63* (20), 201304.
167. Bonapasta, A. A.; Filippone, F.; Mattioli, G., H-Induced dangling bonds in H–isoelectronic-impurity complexes formed in GaAs 1− y N y alloys. *Physical review letters* **2007,** *98* (20), 206403.
168. Janotti, A.; Zhang, S.; Wei, S.-H.; Van de Walle, C., Effects of hydrogen on the electronic properties of dilute GaAsN alloys. *Physical review letters* **2002,** *89* (8), 086403.
169. Fukuda, M.; Whiteside, V.; Keay, J.; Meleco, A.; Sellers, I.; Hossain, K.; Golding, T.; Leroux, M.; Al Khalfioui, M., Improved performance in GaInNAs solar cells by hydrogen passivation. *Applied Physics Letters* **2015,** *106* (14), 141904.
170. Bissiri, M.; von Högersthal, G. B. H.; Polimeni, A.; Gaspari, V.; Ranalli, F.; Capizzi, M.; Bonapasta, A. A.; Jiang, F.; Stavola, M.; Gollub, D., Hydrogen-induced passivation of nitrogen in GaAs 1− y N y. *Physical Review B* **2002,** *65* (23), 235210.
171. Polimeni, A.; von Högersthal, G. B. H.; Bissiri, M.; Capizzi, M.; Frova, A.; Fischer, M.; Reinhardt, M.; Forchel, A., Role of hydrogen in III–N–V compound semiconductors. *Semiconductor science and technology* **2002,** *17* (8), 797.
172. Brown, C.; Estes, N.; Whiteside, V.; Wang, B.; Hossain, K.; Golding, T.; Leroux, M.; Al Khalfioui, M.; Tischler, J.; Ellis, C., The effect and nature of N–H complexes in the control of the dominant photoluminescence transitions in UV-hydrogenated GaInNAs. *RSC Advances* **2017,** *7* (41), 25353-25361.
173. Patriarche, G.; Largeau, L.; Harmand, J. C.; Gollub, D., Morphology and composition of highly strained InGaAs and InGaAsN layers grown on GaAs substrate. *Applied Physics Letters* **2004,** *84* (2), 203-205.
174. Uno, K.; Yamada, M.; Tanaka, I.; Ohtsuki, O.; Takizawa, T., Thermal annealing effects and local atomic configurations in GaInNAs thin films. *J Cryst Growth* **2005,** *278* (1-4), 214-218.
175. Pinault, M. A.; Tournie, E., On the origin of carrier localization in Ga1-xInxNyAs1-y/GaAs quantum wells. *Applied Physics Letters* **2001,** *78* (11), 1562-1564.
176. Kresse, G.; Furthmuller, J., Efficient Iterative Schemes for ab Initio Total-Energy Calculations Using a Plane-Wave Basis Set. *Physical Review B* **1996,** *54*, 11169-11186.

177. Perdew, J. P.; Burke, K.; Ernzerhof, M., Generalized Gradient Approximation Made Simple. *Physical Review B* **1996,** *77*, 3865-3868.
178. Blochl, P. E., Projector Augmented-Wave Method. *Physical Review B* **1994,** *50*, 17953-17979.
179. Grimme, S.; Ehrlich, S.; Goerigk, L., Effect of the Damping Function in Dispersion Corrected Density Functional Theory. *J Comput Chem* **2011,** *32* (7), 1456-1465.
180. Krukau, A. V.; Vydrov, O. A.; Izmaylov, A. F.; Scuseria, G. E., Influence of the exchange screening parameter on the performance of screened hybrid functionals. *The Journal of chemical physics* **2006,** *125* (22), 224106.
181. Moses, P. G.; Miao, M.; Yan, Q.; Van de Walle, C. G., Hybrid functional investigations of band gaps and band alignments for AlN, GaN, InN, and InGaN. *The Journal of chemical physics* **2011,** *134* (8), 084703.
182. Nuytten, T.; Hayne, M.; Bansal, B.; Liu, H. Y.; Hopkinson, M.; Moshchalkov, V. V., Charge separation and temperature-induced carrier migration in Ga1-xInxNyAs1-y multiple quantum wells. *Physical Review B* **2011,** *84* (4).
183. Kudrawiec, R.; Latkowska, M.; Baranowski, M.; Misiewicz, J.; Li, L. H.; Harmand, J. C., Photoreflectance, photoluminescence, and microphotoluminescence study of optical transitions between delocalized and localized states in GaN0.02As0.98, Ga0.95In0.05N0.02As0.98, and GaN0.02As0.90Sb0.08 layers. *Physical Review B* **2013,** *88* (12).
184. Kudrawiec, R.; Syperek, M.; Latkowska, M.; Misiewicz, J.; Korpijarvi, V. M.; Laukkanen, P.; Pakarinen, J.; Dumitrescu, M.; Guina, M.; Pessa, M., Influence of non-radiative recombination on photoluminescence decay time in GaInNAs quantum wells with Ga- and In-rich environments of nitrogen atoms. *Journal of Applied Physics* **2012,** *111* (6).
185. Wu, J.; Shan, W.; Walukiewicz, W., Band anticrossing in highly mismatched III-V semiconductor alloys. *Semiconductor Science and Technology* **2002,** *17* (8), 860-869.
186. Varshni, Y. P., Temperature dependence of the energy gap in semiconductors. *physica* **1967,** *34* (1), 149-154.
187. Harris, J. S., The opportunities, successes and challenges for GaInNAsSb. *J Cryst Growth* **2005,** *278* (1-4), 3-17.
188. Li, L.; Yu, Y.; Ye, G. J.; Ge, Q.; Ou, X.; Wu, H.; Feng, D.; Chen, X. H.; Zhang, Y., Black phosphorus field-effect transistors. *Nature Nanotechnology* **2014,** *9*, 372-377.
189. Koenig, S. P.; Doganov, R. A.; Schmidt, H.; Neto, A. H. C.; Ozyilmaz, B., Electric field effect in ultrathin black phosphorus. *Applied Physics Letters* **2014,** *104* (10), 103106.
190. Liu, H.; Neal, A. T.; Zhu, Z.; Luo, Z.; Xu, X. F.; Tomanek, D.; Ye, P. D., Phosphorene: An Unexplored 2D Semiconductor with a High Hole Mobility. *Acs Nano* **2014,** *8* (4), 4033-4041.
191. Xia, F.; Wang, H.; Jia, Y., Rediscovering black phosphorus as an anisotropic layered material for optoelectronics and electronics. *Nature Communication* **2014,** *5*, 4458-4465.
192. Carvalho, A.; Wang, M.; Zhu, X.; Rodin, A. S.; Su, H.; Neto, A. H. C., Phosphorene: from theory to applications. *Nature Reviews Materials* **2016,** *1*, 16061.

193. Hong, T.; Chamlagain, B.; Wang, T. J.; Chuang, H. J.; Zhou, Z. X.; Xu, Y. Q., Anisotropic photocurrent response at black phosphorus-MoS2 p-n heterojunctions. *Nanoscale* **2015,** *7* (44), 18537-18541.
194. Tran, V.; Soklaski, R.; Liang, Y.; Yang, L., Layer-controlled band gap and anisotropic excitons in few-layer black phosphorus. *Physical Review B* **2014,** *89* (23), 235319.
195. Wu, M. H.; Zeng, X. C., Intrinsic Ferroelasticity and/or Multiferroicity in Two-Dimensional Phosphorene and Phosphorene Analogues. *Nano Letters* **2016,** *16* (5), 3236-3241.
196. Huang, Y.; Qiao, J.; He, K.; Bliznakov, S.; Sutter, E.; Chen, X.; Luo, D.; Meng, F.; Su, D.; Decker, J.; Ji, W.; Ruoff, R. S.; Sutter, P., Interaction of Black Phosphorus with Oxygen and Water. *Chem Mater* **2016,** *28* (22), 8330-8339.
197. Zhou, Q. H.; Chen, Q.; Tong, Y. L.; Wang, J. L., Light-Induced Ambient Degradation of Few-Layer Black Phosphorus: Mechanism and Protection. *Angew Chem Int Edit* **2016,** *55* (38), 11437-11441.
198. Illarionov, Y. Y.; Waltl, M.; Rzepa, G.; Kim, J. S.; Kim, S.; Dodabalapur, A.; Akinwande, D.; Grasser, T., Long-Term Stability and Reliability of Black Phosphorus Field-Effect Transistors. *Acs Nano* **2016,** *10* (10), 9543-9549.
199. Yang, Q.; Xiong, W.; Zhu, L.; Gao, G. Y.; Wu, M. H., Chemically Functionalized Phosphorene: Two-Dimensional Multiferroics with Vertical Polarization and Mobile Magnetism. *Journal of the American Chemical Society* **2017,** *139* (33), 11506-11512.
200. Hu, G. H.; Albrow-Owen, T.; Jin, X. X.; Ali, A.; Hu, Y. W.; Howe, R. C. T.; Shehzad, K.; Yang, Z. Y.; Zhu, X. K.; Woodward, R. I.; Wu, T. C.; Jussila, H.; Wu, J. B.; Peng, P.; Tan, P. H.; Sun, Z. P.; Kelleher, E. J. R.; Zhang, M.; Xu, Y.; Hasan, T., Black phosphorus ink formulation for inkjet printing of optoelectronics and photonics. *Nature Communications* **2017,** *8*, 278.
201. Tsetseris, L.; Wang, B.; Pantelides, S. T., Substitutional doping of graphene: The role of carbon divacancies. *Physical Review B* **2014,** *89* (3), 035411.
202. Kuila, T.; Bose, S.; Mishra, A. K.; Khanra, P.; Kim, N. H.; Lee, J. H., Chemical functionalization of graphene and its applications. *Progress in Materials Science* **2012,** *57* (7), 1061-1105.
203. Georgakilas, V.; Otyepka, M.; Bourlinos, A. B.; Chandra, V.; Kim, N.; Kemp, K. C.; Hobza, P.; Zboril, R.; Kim, K. S., Functionalization of graphene: covalent and non-covalent approaches, derivatives and applications. *Chemical reviews* **2012,** *112* (11), 6156-6214.
204. Wang, B.; Tsetseris, L.; Pantelides, S. T., Introduction of nitrogen with controllable configuration into graphene via vacancies and edges. *Journal of Materials Chemistry A* **2013,** *1* (47), 14927-14934.
205. Pantelides, S. T.; Puzyrev, Y.; Tsetseris, L.; Wang, B., Defects and doping and their role in functionalizing graphene. *Mrs Bulletin* **2012,** *37* (12), 1187-1194.
206. Zhang, H.; Bekyarova, E.; Huang, J. W.; Zhao, Z.; Bao, W. Z.; Wang, F. L.; Haddon, R. C.; Lau, C. N., Aryl Functionalization as a Route to Band Gap Engineering in Single Layer Graphene Devices. *Nano Letters* **2011,** *11* (10), 4047-4051.

207. He, H. K.; Gao, C., General Approach to Individually Dispersed, Highly Soluble, and Conductive Graphene Nanosheets Functionalized by Nitrene Chemistry. *Chem Mater* **2010,** *22* (17), 5054-5064.
208. Si, Y.; Samulski, E. T., Synthesis of water soluble graphene. *Nano Letters* **2008,** *8* (6), 1679-1682.
209. Hossain, M. Z.; Walsh, M. A.; Hersam, M. C., Scanning Tunneling Microscopy, Spectroscopy, and Nanolithography of Epitaxial Graphene Chemically Modified with Aryl Moieties. *Journal of the American Chemical Society* **2010,** *132* (43), 15399-15403.
210. Tayari, V.; Hemsworth, N.; Fakih, I.; Favron, A.; Gaufres, E.; Gervais, G.; Martel, R.; Szkopek, T., Two-dimensional magnetotransport in a black phosphorus naked quantum well. *Nature Communications* **2015,** *6*, 7702.
211. Ahmet Avsar, I. J. V.-M., Jun You Tan, Kenji Watanabe, Takashi Taniguchi,; Antonio H. Castro Neto, B. O., Air-Stable Transport in Graphene-Contacted, Fully Encapsulated Ultrathin Black Phosphorus Based Field-Effect Transistors. *ACS Nano* **2015,** *9*, 4138-4145.
212. Doganov, R. A.; Koenig, S. P.; Yeo, Y. T.; Watanabe, K.; Taniguchi, T.; Ozyilmaz, B., Transport properties of ultrathin black phosphorus on hexagonal boron nitride. *Applied Physics Letters* **2015,** *106* (8), 083505.
213. Wood, J. D.; Wells, S. A.; Jariwala, D.; Chen, K.-S.; Cho, E.; Sangwan, V. K.; Liu, X.; Marks, L. J.; Hersam, M. C., Effective Passivation of Exfoliated Black Phosphorus Transistors against Ambient Degradation. *Nanoletters* **2014,** *14*, 6964-6970.
214. Ryder, C. R.; Wood, J. D.; Wells, S. A.; Yang, Y.; Jariwala, D.; Marks, T. J.; Schatz, G. C.; Hersam, M. C., Covalent functionalization and passivation of exfoliated black phosphorus via aryl diazonium chemistry. *Nature Chemistry* **2016,** *8*, 597-602.
215. Li, Q.; Zhou, Q.; Niu, X.; Zhao, Y.; Chen, Q.; Wang, J., Covalent Functionalization of Black Phosphorus from First-Principles. *The Journal of Physical Chemistry Letters* **2016,** *7* (22), 4540-4546.
216. Grimme, S.; Antony, J.; Ehrlich, S.; Krieg, H., A consistent and accurate ab intitio parametrization of density functional dispersion correction [DFT-D] for the 94 elements H-Pu. *The Journal of Chemical Physics* **2010,** *132*, 154104.
217. Stefan Grimme; Stephan Ehrlich; Goerigk, L., Effect of the Damping Function in Dispersion Coreected Density Functional Theory. *The Journal of Computational Chemistry* **2011,** *32*, 1456-1465.
218. AV, K.; OA, V.; AF, I.; GE, S., Influence of the exchange screening parameter on the performance of screened hybrid functionals. *The Journal of Chemical Physics* **2006,** *125*, 224106.
219. Qiao, J. S.; Kong, X. H.; Hu, Z. X.; Yang, F.; Ji, W., High-mobility transport anisotropy and linear dichroism in few-layer black phosphorus. *Nature Communications* **2014,** *5*, 4475.
220. Cai, Y. Q.; Zhang, G.; Zhang, Y. W., Layer-dependent Band Alignment and Work Function of Few-Layer Phosphorene. *Sci Rep-Uk* **2014,** *4*, 6677.
221. Schusteritsch, G.; Uhrin, M.; Pickard, C. J., Single-Layered Hittorf's Phosphorus: A Wide-Bandgap High Mobility 2D Material. *Nano Letters* **2016,** *16* (5), 2975-2980.
222. Allan Brown, S. R., Refinement of the crystal structure of black phosphorus. *Acta Crystallogr* **1965,** *19*.

223. Cartz, L.; Srinivasa, S. R.; Riedner, R. J.; Jorgensen, J. D.; Worlton, T. G., Effect of Pressure on Bonding in Black Phosphorus. *J Chem Phys* **1979,** *71* (4), 1718-1721.
224. Wang, B.; Gunther, S.; Wintterlin, J.; Bocquet, M. L., Periodicity, work function and reactivity of graphene on Ru(0001) from first principles. *New J Phys* **2010,** *12*, 043041.
225. Liu, N. S.; Zhou, S., Gas adsorption on monolayer blue phosphorus: implications for environmental stability and gas sensors. *Nanotechnology* **2017,** *28* (17), 175708.
226. Henkelman, G.; Arnaldsson, A.; Jonsson, H., A fast and robust algorithm for Bader decomposition of charge density. *Comp Mater Sci* **2006,** *36* (3), 354-360.
227. Resasco, D. E.; Wang, B.; Crossley, S., Zeolite-catalysed C–C bond forming reactions for biomass conversion to fuels and chemicals. *Catalysis Science & Technology* **2016,** *6* (8), 2543-2559.
228. Gumidyala, A.; Wang, B.; Crossley, S., Direct carbon-carbon coupling of furanics with acetic acid over Brønsted zeolites. *Science advances* **2016,** *2* (9), e1601072.
229. Huang, L.; Huo, N. J.; Li, Y.; Chen, H.; Yang, J. H.; Wei, Z. M.; Li, J. B.; Li, S. S., Electric-Field Tunable Band Offsets in Black Phosphorus and MoS2 van der Waals p-n Heterostructure. *J Phys Chem Lett* **2015,** *6* (13), 2483-2488.
230. Zhou, L. J.; Zhang, J.; Zhuo, Z. W.; Kou, L. Z.; Ma, W.; Shao, B.; Du, A. J.; Meng, S.; Frauenheim, T., Novel Excitonic Solar Cells in Phosphorene-TiO2 Heterostructures with Extraordinary Charge Separation Efficiency. *J Phys Chem Lett* **2016,** *7* (10), 1880-1887.
231. Rahman, M. Z.; Kwong, C. W.; Davey, K.; Qiao, S. Z., 2D phosphorene as a water splitting photocatalyst: fundamentals to applications. *Energ Environ Sci* **2016,** *9* (3), 709-728.
232. Geim, A. K.; Grigorieva, I. V., Van der Waals heterostructures. *Nature* **2013,** *499* (7459), 419-425.
233. Liu, Y.; Weiss, N. O.; Duan, X.; Cheng, H.-C.; Huang, Y.; Duan, X., Van der Waals heterostructures and devices. *Nature Reviews Materials* **2016,** *1* (9), 1-17.
234. Novoselov, K. S.; Mishchenko, A.; Carvalho, A.; Neto, A. H. C., 2D materials and van der Waals heterostructures. *Science* **2016,** *353* (6298), aac9439.
235. Butler, S. Z.; Hollen, S. M.; Cao, L.; Cui, Y.; Gupta, J. A.; Gutiérrez, H. R.; Heinz, T. F.; Hong, S. S.; Huang, J.; Ismach, A. F., Progress, challenges, and opportunities in two-dimensional materials beyond graphene. *ACS nano* **2013,** *7* (4), 2898-2926.
236. Molina-Mendoza, A. J.; Giovanelli, E.; Paz, W. S.; Niño, M. A.; Island, J. O.; Evangeli, C.; Aballe, L.; Foerster, M.; Van Der Zant, H. S. J.; Rubio-Bollinger, G., Franckeite as a naturally occurring van der Waals heterostructure. *Nature communications* **2017,** *8* (1), 1-9.
237. Velický, M.; Toth, P. S.; Rakowski, A. M.; Rooney, A. P.; Kozikov, A.; Woods, C. R.; Mishchenko, A.; Fumagalli, L.; Yin, J.; Zólyomi, V., Exfoliation of natural van der Waals heterostructures to a single unit cell thickness. *Nature communications* **2017,** *8* (1), 1-11.
238. Prando, G., Van der Waals heterostructures: The natural way. *Nature nanotechnology* **2017,** *12* (3), 191.

239. Klots, A. R.; Newaz, A. K. M.; Wang, B.; Prasai, D.; Krzyzanowska, H.; Lin, J.; Caudel, D.; Ghimire, N. J.; Yan, J.; Ivanov, B. L., Probing excitonic states in suspended two-dimensional semiconductors by photocurrent spectroscopy. *Sci Rep-Uk* **2014,** *4*, 6608.
240. Xia, Y.; Whitesides, G. M., Soft lithography. *Annual review of materials science* **1998,** *28* (1), 153-184.
241. Kresse, G.; Furthmüller, J., Efficient iterative schemes for ab initio total-energy calculations using a plane-wave basis set. *Physical review B* **1996,** *54* (16), 11169.
242. Blöchl, P. E., Projector augmented-wave method. *Physical review B* **1994,** *50* (24), 17953.
243. Kresse, G.; Joubert, D., From ultrasoft pseudopotentials to the projector augmented-wave method. *Physical review b* **1999,** *59* (3), 1758.
244. Makovicky, E.; Petříček, V.; Dušek, M.; Topa, D., The crystal structure of franckeite, Pb21. 7Sn9. 3Fe4. 0Sb8. 1S56. 9. *American Mineralogist* **2011,** *96* (11-12), 1686-1702.
245. Momma, K.; Izumi, F., VESTA 3 for three-dimensional visualization of crystal, volumetric and morphology data. *Journal of applied crystallography* **2011,** *44* (6), 1272-1276.
246. Wang, B.; Bocquet, M. L.; Marchini, S.; Günther, S.; Wintterlin, J., Chemical origin of a graphene moiré overlayer on Ru (0001). *Physical Chemistry Chemical Physics* **2008,** *10* (24), 3530-3534.
247. Wang, B.; Bocquet, M.-L., Interfacial coupling in rotational monolayer and bilayer graphene on Ru (0001) from first principles. *Nanoscale* **2012,** *4* (15), 4687-4693.
248. Xu, Y.; Schoonen, M. A. A., The absolute energy positions of conduction and valence bands of selected semiconducting minerals. *American Mineralogist* **2000,** *85* (3-4), 543-556.
249. Boldish, S. I.; White, W. B., Optical band gaps of selected ternary sulfide minerals. *American Mineralogist* **1998,** *83* (7-8), 865-871.
250. Unuchak, D. M.; Bente, K.; Kloess, G.; Schmitz, W.; Gremenok, V. F.; Ivanov, V. A.; Ukhov, V., Structure and optical properties of PbS-SnS mixed crystal thin films. *physica status solidi c* **2009,** *6* (5), 1191-1194.
251. Soriano, R. B.; Malliakas, C. D.; Wu, J.; Kanatzidis, M. G., Cubic Form of Pb2–x Sn x S2 Stabilized through Size Reduction to the Nanoscale. *Journal of the American Chemical Society* **2012,** *134* (6), 3228-3233.
252. He, J.; Girard, S. N.; Zheng, J. C.; Zhao, L.; Kanatzidis, M. G.; Dravid, V. P., Strong phonon scattering by layer structured PbSnS2 in PbTe based thermoelectric materials. *Advanced Materials* **2012,** *24* (32), 4440-4444.
253. Segal, E.; Madon, R.; Boudart, M., Catalytic hydrogenation of cyclohexene: I. Vapor-phase reaction on supported platinum. *Journal of Catalysis* **1978,** *52* (1), 45-49.
254. Madon, R.; O'connell, J.; Boudart, M., Catalytic hydrogenation of cyclohexene: Part II. Liquid phase reaction on supported platinum in a gradientless slurry reactor. *AIChE Journal* **1978,** *24* (5), 904-911.
255. Gonzo, E.; Boudart, M., Catalytic hydrogenation of cyclohexene: 3. Gas-phase and liquid-phase reaction on supported palladium. *Journal of Catalysis* **1978,** *52* (3), 462-471.

256. Boudart, M.; Cheng, W., Catalytic hydrogenation of cyclohexene: 7. Liquid phase reaction on supported nickel. *Journal of Catalysis* **1987,** *106* (1), 134-143.
257. Boudart, M.; Sajkowski, D., Catalytic hydrogenation of cyclohexene: liquid-phase reaction on rhodium. *Faraday Discussions* **1991,** *92*, 57-67.
258. Chen, Y.-W.; Li, C., Liquid phase hydrogenation of cyclohexene over Pt/aluminum borate catalyst. *Catalysis letters* **1992,** *13* (4), 359-361.
259. Lu, S.; Lonergan, W. W.; Bosco, J. P.; Wang, S.; Zhu, Y.; Xie, Y.; Chen, J. G., Low temperature hydrogenation of benzene and cyclohexene: a comparative study between γ-Al 2 O 3 supported PtCo and PtNi bimetallic catalysts. *Journal of Catalysis* **2008,** *259* (2), 260-268.
260. Rioux, R.; Hsu, B.; Grass, M.; Song, H.; Somorjai, G. A., Influence of particle size on reaction selectivity in cyclohexene hydrogenation and dehydrogenation over silica-supported monodisperse Pt particles. *Catalysis letters* **2008,** *126* (1-2), 10.
261. Denning, A. L.; Dang, H.; Liu, Z.; Nicholas, K. M.; Jentoft, F. C., Deoxydehydration of Glycols Catalyzed by Carbon-Supported Perrhenate. *ChemCatChem* **2013,** *5* (12), 3567-3570.
262. Sitthisa, S.; Resasco, D. E., Hydrodeoxygenation of furfural over supported metal catalysts: a comparative study of Cu, Pd and Ni. *Catalysis letters* **2011,** *141* (6), 784-791.
263. Silverstein, R. M.; Webster, F. X.; Kiemle, D. J.; Bryce, D. L., *Spectrometric identification of organic compounds*. John wiley & sons: 2014.
264. Slater, J. C., Atomic radii in crystals. *The Journal of Chemical Physics* **1964,** *41* (10), 3199-3204.
265. Mukherjee, S.; Vannice, M. A., Solvent effects in liquid-phase reactions II. Kinetic modeling for citral hydrogenation. *Journal of Catalysis* **2006,** *243* (1), 131-148.
266. Rao, R. S.; Baker, R. T. K.; Vannice, M. A., Furfural hydrogenation over carbon-supported copper. *Catalysis Letters* **1999,** *60* (1-2), 51-57.
267. Nie, L.; Resasco, D. E., Kinetics and mechanism of m-cresol hydrodeoxygenation on a Pt/SiO 2 catalyst. *Journal of Catalysis* **2014,** *317*, 22-29.
268. Watwe, R. M.; Cortright, R. D.; Nørskov, J. K.; Dumesic, J. A., Theoretical studies of stability and reactivity of C2 hydrocarbon species on Pt clusters, Pt (111), and Pt (211). *The Journal of Physical Chemistry B* **2000,** *104* (10), 2299-2310.
269. Eberhardt, W.; Louie, S. G.; Plummer, E., Interaction of hydrogen with a Pd (111) surface. *Physical Review B* **1983,** *28* (2), 465.
270. Mitsui, T.; Rose, M.; Fomin, E.; Ogletree, D.; Salmeron, M., Dissociative hydrogen adsorption on palladium requires aggregates of three or more vacancies. *Nature* **2003,** *422* (6933), 705-707.
271. Watson, G. W.; Wells, R. P.; Willock, D. J.; Hutchings, G. J., A comparison of the adsorption and diffusion of hydrogen on the {111} surfaces of Ni, Pd, and Pt from density functional theory calculations. *The Journal of Physical Chemistry B* **2001,** *105* (21), 4889-4894.
272. Singh, U. K.; Vannice, M. A., Kinetic and thermodynamic analysis of liquid-phase benzene hydrogenation. *AIChE journal* **1999,** *45* (5), 1059-1071.
273. Laidler, K. J., *Chemical kinetics*. 1987.
274. Neurock, M.; Pallassana, V.; van Santen, R. A., The importance of transient states at higher coverages in catalytic reactions. *Journal of the American Chemical Society* **2000,** *122* (6), 1150-1153.

275. Züttel, A., Materials for hydrogen storage. *Materials today* **2003,** *6* (9), 24-33.
276. Sheng, W.; Kattel, S.; Yao, S.; Yan, B.; Liang, Z.; Hawxhurst, C. J.; Wu, Q.; Chen, J. G., Electrochemical reduction of CO 2 to synthesis gas with controlled CO/H 2 ratios. *Energ Environ Sci* **2017,** *10* (5), 1180-1185.
277. Zuzek, E.; Abriata, J.; San-Martin, A.; Manchester, F., Phase Diagrams of Binary Hydrogen Alloys. *ASM International, Materials Park, OH* **2000**, 309-310.
278. Johansson, M.; Skulason, E.; Nielsen, G.; Murphy, S.; Nielsen, R. M.; Chorkendorff, I., Hydrogen adsorption on palladium and palladium hydride at 1 bar. *Surface science* **2010,** *604* (7-8), 718-729.
279. Aslam, U.; Chavez, S.; Linic, S., Controlling energy flow in multimetallic nanostructures for plasmonic catalysis. *Nature nanotechnology* **2017,** *12* (10), 1000.
280. Baffou, G.; Quidant, R., Nanoplasmonics for chemistry. *Chemical Society Reviews* **2014,** *43* (11), 3898-3907.
281. Linic, S.; Aslam, U.; Boerigter, C.; Morabito, M., Photochemical transformations on plasmonic metal nanoparticles. *Nature materials* **2015,** *14* (6), 567-576.
282. Hashmi, A. S. K.; Hutchings, G. J., Gold catalysis. *Angewandte Chemie International Edition* **2006,** *45* (47), 7896-7936.
283. Dong, X.-Y.; Gao, Z.-W.; Yang, K.-F.; Zhang, W.-Q.; Xu, L.-W., Nanosilver as a new generation of silver catalysts in organic transformations for efficient synthesis of fine chemicals. *Catalysis Science & Technology* **2015,** *5* (5), 2554-2574.
284. Hao, C.-H.; Guo, X.-N.; Pan, Y.-T.; Chen, S.; Jiao, Z.-F.; Yang, H.; Guo, X.-Y., Visible-light-driven selective photocatalytic hydrogenation of cinnamaldehyde over Au/SiC catalysts. *Journal of the American Chemical Society* **2016,** *138* (30), 9361-9364.
285. Wang, J. L.; Ando, R. A.; Camargo, P. H. C., Investigating the plasmon-mediated catalytic activity of AgAu nanoparticles as a function of composition: are two metals better than one? *ACS Catalysis* **2014,** *4* (11), 3815-3819.
286. Shown, I.; Hsu, H.-C.; Chang, Y.-C.; Lin, C.-H.; Roy, P. K.; Ganguly, A.; Wang, C.-H.; Chang, J.-K.; Wu, C.-I.; Chen, L.-C., Highly efficient visible light photocatalytic reduction of CO2 to hydrocarbon fuels by Cu-nanoparticle decorated graphene oxide. *Nano letters* **2014,** *14* (11), 6097-6103.
287. Knight, M. W.; King, N. S.; Liu, L.; Everitt, H. O.; Nordlander, P.; Halas, N. J., Aluminum for plasmonics. *ACS nano* **2014,** *8* (1), 834-840.
288. Cushing, S. K.; Wu, N., Progress and perspectives of plasmon-enhanced solar energy conversion. *The journal of physical chemistry letters* **2016,** *7* (4), 666-675.
289. Peiris, S.; McMurtrie, J.; Zhu, H.-Y., Metal nanoparticle photocatalysts: emerging processes for green organic synthesis. *Catalysis Science & Technology* **2016,** *6* (2), 320-338.
290. Kim, Y.; Dumett Torres, D.; Jain, P. K., Activation energies of plasmonic catalysts. *Nano letters* **2016,** *16* (5), 3399-3407.
291. Kumar, D.; Lee, A.; Lee, T.; Lim, M.; Lim, D.-K., Ultrafast and efficient transport of hot plasmonic electrons by graphene for Pt free, highly efficient visible-light responsive photocatalyst. *Nano letters* **2016,** *16* (3), 1760-1767.
292. Hughes, M. D.; Xu, Y.-J.; Jenkins, P.; McMorn, P.; Landon, P.; Enache, D. I.; Carley, A. F.; Attard, G. A.; Hutchings, G. J.; King, F., Tunable gold catalysts for

selective hydrocarbon oxidation under mild conditions. *Nature* **2005,** *437* (7062), 1132-1135.
293. Robatjazi, H.; Zhao, H.; Swearer, D. F.; Hogan, N. J.; Zhou, L.; Alabastri, A.; McClain, M. J.; Nordlander, P.; Halas, N. J., Plasmon-induced selective carbon dioxide conversion on earth-abundant aluminum-cuprous oxide antenna-reactor nanoparticles. *Nature communications* **2017,** *8* (1), 1-10.
294. Shao, L.; Huang, X.; Teschner, D.; Zhang, W., Gold supported on graphene oxide: an active and selective catalyst for phenylacetylene hydrogenations at low temperatures. *ACS Catalysis* **2014,** *4* (7), 2369-2373.
295. da Silva, A. G. M.; Rodrigues, T. S.; Correia, V. G.; Alves, T. V.; Alves, R. S.; Ando, R. A.; Ornellas, F. R.; Wang, J.; Andrade, L. H.; Camargo, P. H. C., Plasmonic Nanorattles as Next-Generation Catalysts for Surface Plasmon Resonance-Mediated Oxidations Promoted by Activated Oxygen. *Angewandte Chemie International Edition* **2016,** *55* (25), 7111-7115.
296. Hou, W.; Cronin, S. B., A review of surface plasmon resonance-enhanced photocatalysis. *Advanced Functional Materials* **2013,** *23* (13), 1612-1619.
297. Naya, S.-i.; Kimura, K.; Tada, H., One-step selective aerobic oxidation of amines to imines by gold nanoparticle-loaded rutile titanium (IV) oxide plasmon photocatalyst. *Acs Catalysis* **2013,** *3* (1), 10-13.
298. Christopher, P.; Xin, H.; Linic, S., Visible-light-enhanced catalytic oxidation reactions on plasmonic silver nanostructures. *Nature chemistry* **2011,** *3* (6), 467.
299. Long, R.; Rao, Z.; Mao, K.; Li, Y.; Zhang, C.; Liu, Q.; Wang, C.; Li, Z. Y.; Wu, X.; Xiong, Y., Efficient Coupling of Solar Energy to Catalytic Hydrogenation by Using Well-Designed Palladium Nanostructures. *Angewandte Chemie International Edition* **2015,** *54* (8), 2425-2430.
300. Besson, M. l.; Gallezot, P.; Pinel, C., Conversion of biomass into chemicals over metal catalysts. *Chemical reviews* **2014,** *114* (3), 1827-1870.
301. Corma, A.; Serna, P., Chemoselective hydrogenation of nitro compounds with supported gold catalysts. *Science* **2006,** *313* (5785), 332-334.
302. Wang, D.; Astruc, D., The golden age of transfer hydrogenation. *Chemical reviews* **2015,** *115* (13), 6621-6686.
303. Bond, G. C., Hydrogenation by gold catalysts: an unexpected discovery and a current assessment. *Gold Bulletin* **2016,** *49* (3-4), 53-61.
304. Bond, G. C.; Sermon, P. A.; Webb, G.; Buchanan, D. A.; Wells, P. B., Hydrogenation over supported gold catalysts. *Journal of the Chemical Society, Chemical Communications* **1973,** (13), 444b-445.
305. Cococcioni, M.; De Gironcoli, S., Linear response approach to the calculation of the effective interaction parameters in the LDA+ U method. *Physical Review B* **2005,** *71* (3), 035105.
306. Mattioli, G.; Alippi, P.; Filippone, F.; Caminiti, R.; Amore Bonapasta, A., Deep versus shallow behavior of intrinsic defects in rutile and anatase TiO2 polymorphs. *The Journal of Physical Chemistry C* **2010,** *114* (49), 21694-21704.
307. Tsukamoto, D.; Shiraishi, Y.; Sugano, Y.; Ichikawa, S.; Tanaka, S.; Hirai, T., Gold nanoparticles located at the interface of anatase/rutile TiO2 particles as active plasmonic photocatalysts for aerobic oxidation. *Journal of the American Chemical Society* **2012,** *134* (14), 6309-6315.

308. Dong, R.; Zhang, Q.; Gao, W.; Pei, A.; Ren, B., Highly efficient light-driven TiO2–Au Janus micromotors. *ACS nano* **2016,** *10* (1), 839-844.
309. Tan, T. H.; Scott, J.; Ng, Y. H.; Taylor, R. A.; Aguey-Zinsou, K.-F.; Amal, R., Understanding plasmon and band gap photoexcitation effects on the thermal-catalytic oxidation of ethanol by TiO2-supported gold. *ACS catalysis* **2016,** *6* (3), 1870-1879.
310. Herves, P.; Pérez-Lorenzo, M.; Liz-Marzán, L. M.; Dzubiella, J.; Lu, Y.; Ballauff, M., Catalysis by metallic nanoparticles in aqueous solution: model reactions. *Chemical Society Reviews* **2012,** *41* (17), 5577-5587.
311. Corma, A.; Concepción, P.; Serna, P., A different reaction pathway for the reduction of aromatic nitro compounds on gold catalysts. *Angewandte Chemie International Edition* **2007,** *46* (38), 7266-7269.
312. Fujitani, T.; Nakamura, I.; Akita, T.; Okumura, M.; Haruta, M., Hydrogen dissociation by gold clusters. *Angewandte Chemie International Edition* **2009,** *48* (50), 9515-9518.
313. Gao, S.; Zhang, Z.; Liu, K.; Dong, B., Direct evidence of plasmonic enhancement on catalytic reduction of 4-nitrophenol over silver nanoparticles supported on flexible fibrous networks. *Applied Catalysis B: Environmental* **2016,** *188*, 245-252.
314. Grätzel, M., Photoelectrochemical cells. *nature* **2001,** *414* (6861), 338-344.
315. Panayotov, D. A.; Frenkel, A. I.; Morris, J. R., Catalysis and photocatalysis by nanoscale Au/TiO2: perspectives for renewable energy. *ACS Energy Letters* **2017,** *2* (5), 1223-1231.
316. Stratakis, M.; Garcia, H., Catalysis by supported gold nanoparticles: beyond aerobic oxidative processes. *Chemical Reviews* **2012,** *112* (8), 4469-4506.
317. Aditya, T.; Pal, A.; Pal, T., Nitroarene reduction: a trusted model reaction to test nanoparticle catalysts. *Chemical Communications* **2015,** *51* (46), 9410-9431.
318. Chiou, J.-R.; Lai, B.-H.; Hsu, K.-C.; Chen, D.-H., One-pot green synthesis of silver/iron oxide composite nanoparticles for 4-nitrophenol reduction. *Journal of hazardous materials* **2013,** *248*, 394-400.
319. Perdew, J. P.; Burke, K.; Ernzerhof, M., Generalized Gradient Approximation Made Simple. *Physical Review Letters* **1996,** *77*, 3865-3868.
320. Blochl, P. E., Projector Augmented-Wave Method. *Physical Review B: Condensed Matter Materials* **1994,** *50*, 17953-17979.
321. Tang, W.; Sanville, E.; Henkelman, G., A grid-based Bader analysis algorithm without lattice bias. *Journal of Physics: Condensed Matter* **2009,** *21* (8), 084204.
322. Sanville, E.; Kenny, S. D.; Smith, R.; Henkelman, G., Improved grid-based algorithm for Bader charge allocation. *Journal of computational chemistry* **2007,** *28* (5), 899-908.
323. Henkelman, G.; Arnaldsson, A.; Jónsson, H., A fast and robust algorithm for Bader decomposition of charge density. *Comp Mater Sci* **2006,** *36* (3), 354-360.
324. Humphrey, W.; Dalke, A.; Schulten, K., VMD: visual molecular dynamics. *Journal of molecular graphics* **1996,** *14* (1), 33-38.
325. Farberow, C. A.; Dumesic, J. A.; Mavrikakis, M., Density functional theory calculations and analysis of reaction pathways for reduction of nitric oxide by hydrogen on Pt (111). *Acs Catalysis* **2014,** *4* (10), 3307-3319.

326. Lerch, D.; Klein, A.; Schmidt, A.; Müller, S.; Hammer, L.; Heinz, K.; Weinert, M., Unusual adsorption site of hydrogen on the unreconstructed Ir (100) surface. *Physical Review B* **2006,** *73* (7), 075430.
327. Gokhale, A. A.; Kandoi, S.; Greeley, J. P.; Mavrikakis, M.; Dumesic, J. A., Molecular-level descriptions of surface chemistry in kinetic models using density functional theory. *Chemical Engineering Science* **2004,** *59* (22-23), 4679-4691.
328. Barbosa, E. C. M.; Fiorio, J. L.; Mou, T.; Wang, B.; Rossi, L. M.; Camargo, P. H. C., Reaction pathway dependence in plasmonic catalysis: hydrogenation as a model molecular transformation. *Chemistry–A European Journal* **2018,** *24* (47), 12330-12339.
329. Zhang, L.; Cao, X.-M.; Hu, P., Insight into chemoselectivity of nitroarene hydrogenation: A DFT-D3 study of nitroarene adsorption on metal surfaces under the realistic reaction conditions. *Applied Surface Science* **2017,** *392*, 456-471.
330. Millán, R.; Liu, L.; Boronat, M.; Corma, A., A new molecular pathway allows the chemoselective reduction of nitroaromatics on non-noble metal catalysts. *Journal of Catalysis* **2018,** *364*, 19-30.
331. Liu, B. H.; Li, Z. P., A review: hydrogen generation from borohydride hydrolysis reaction. *Journal of Power Sources* **2009,** *187* (2), 527-534.
332. Guella, G.; Patton, B.; Miotello, A., Kinetic features of the platinum catalyzed hydrolysis of sodium borohydride from 11B NMR measurements. *The Journal of Physical Chemistry C* **2007,** *111* (50), 18744-18750.
333. Wunder, S.; Polzer, F.; Lu, Y.; Mei, Y.; Ballauff, M., Kinetic analysis of catalytic reduction of 4-nitrophenol by metallic nanoparticles immobilized in spherical polyelectrolyte brushes. *The Journal of Physical Chemistry C* **2010,** *114* (19), 8814-8820.
334. Bae, S.; Gim, S.; Kim, H.; Hanna, K., Effect of NaBH4 on properties of nanoscale zero-valent iron and its catalytic activity for reduction of p-nitrophenol. *Applied Catalysis B: Environmental* **2016,** *182*, 541-549.
335. Chang, Y.-C.; Chen, D.-H., Catalytic reduction of 4-nitrophenol by magnetically recoverable Au nanocatalyst. *Journal of hazardous materials* **2009,** *165* (1-3), 664-669.
336. Kuroda, K.; Ishida, T.; Haruta, M., Reduction of 4-nitrophenol to 4-aminophenol over Au nanoparticles deposited on PMMA. *Journal of Molecular Catalysis A: Chemical* **2009,** *298* (1-2), 7-11.
337. Tacey, S. A.; Szilvási, T.; Xu, L.; Schauer, J. J.; Mavrikakis, M., The role of iron-oxide aerosols and sunlight in the atmospheric reduction of Hg (II) species: A DFT+ U study. *Applied Catalysis B: Environmental* **2018,** *234*, 347-356.
338. Kubota, Y.; Watanabe, K.; Tsuda, O.; Taniguchi, T., Deep ultraviolet light-emitting hexagonal boron nitride synthesized at atmospheric pressure. *Science* **2007,** *317* (5840), 932-934.
339. Shishkin, M.; Kresse, G., Self-consistent G W calculations for semiconductors and insulators. *Physical Review B* **2007,** *75* (23), 235102.
340. Li, L. H.; Chen, Y., Atomically thin boron nitride: unique properties and applications. *Advanced Functional Materials* **2016,** *26* (16), 2594-2608.
341. Sinthika, S.; Kumar, E. M.; Thapa, R., Doped h-BN monolayer as efficient noble metal-free catalysts for CO oxidation: the role of dopant and water in activity and catalytic de-poisoning. *Journal of Materials Chemistry A* **2014,** *2* (32), 12812-12820.

342. Topsakal, M.; Aktürk, E.; Ciraci, S., First-principles study of two-and one-dimensional honeycomb structures of boron nitride. *Physical Review B* **2009,** *79* (11), 115442.
343. Kazuma, E.; Jung, J.; Ueba, H.; Trenary, M.; Kim, Y., Direct pathway to molecular photodissociation on metal surfaces using visible light. *Journal of the American Chemical Society* **2017,** *139* (8), 3115-3121.
344. Xie, W.; Schlücker, S., Hot electron-induced reduction of small molecules on photorecycling metal surfaces. *Nature communications* **2015,** *6*, 7570.
345. Swearer, D. F.; Zhao, H.; Zhou, L.; Zhang, C.; Robatjazi, H.; Martirez, J. M. P.; Krauter, C. M.; Yazdi, S.; McClain, M. J.; Ringe, E., Heterometallic antenna–reactor complexes for photocatalysis. *Proceedings of the National Academy of Sciences* **2016,** *113* (32), 8916-8920.
346. Halas, N. J.; Lal, S.; Chang, W.-S.; Link, S.; Nordlander, P., Plasmons in strongly coupled metallic nanostructures. *Chemical reviews* **2011,** *111* (6), 3913-3961.
347. Olsson, F. E.; Persson, M.; Repp, J.; Meyer, G., Scanning tunneling microscopy and spectroscopy of NaCl overlayers on the stepped Cu (311) surface: Experimental and theoretical study. *Physical Review B* **2005,** *71* (7), 075419.
348. Choi, T.; Ruggiero, C. D.; Gupta, J. A., Incommensurability and atomic structure of c (2× 2) N/Cu (100): A scanning tunneling microscopy study. *Physical Review B* **2008,** *78* (3), 035430.

Appendix A

SUPPLEMENTARY INFORMATION FOR CHAPTER 3

Table A. 1 Formation energy values of H by breaking N-Ga bonds for different configurations used in this work. All the energy values are in eV.

H formation energy	Previously reported Ga-N defect	In-N	In_3-N	$In_3 \equiv N$
on N	0.2	0.3	0.3	0.6
on Ga	0.1	0.1	0.1	0.6

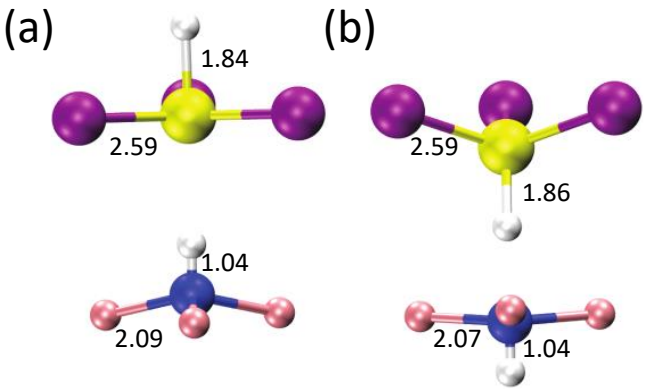

Figure A. 1 Structures of H adsorption (the configuration shown in Figure 3. 2b (a) on the bond-center sites of N and the opposite site of In, (b) on the opposite site of N and In.

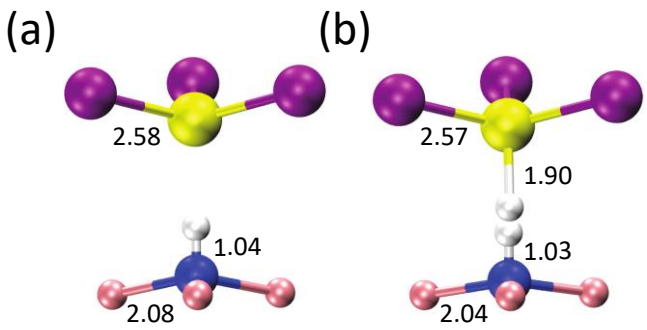

Figure A. 2 Structures of H adsorption (the configuration shown in Figure 3. 2d on the bond-center sites of (a) N and (b) In.

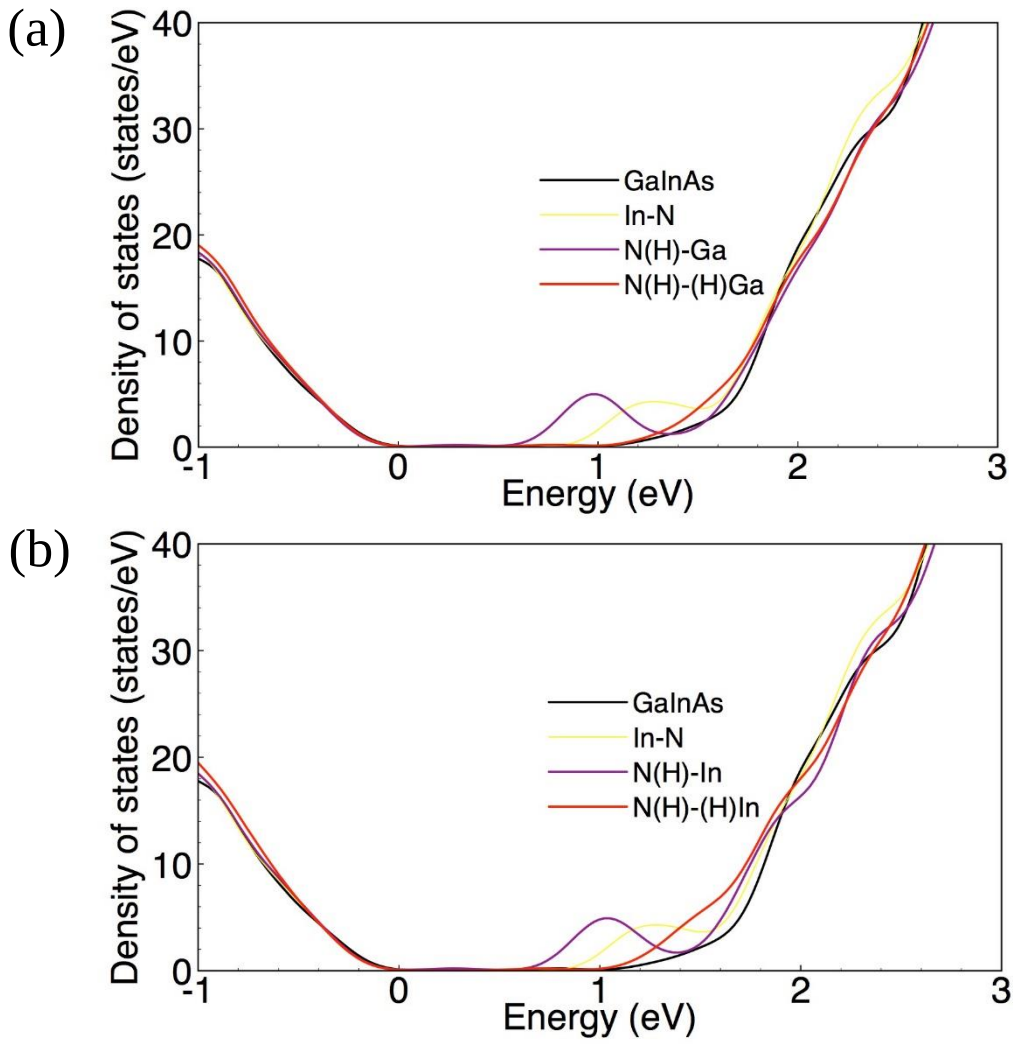

Figure A. 3 Comparison of the total density of states for the In-N structure (Figure 3. 2b) and the subsequent hydrogenation of (a) Ga and (b) In by breaking the Ga-N and In-N bonds. The DOS for original GaInAs (black curve) is plotted as reference. The zero-energy level is set at the valence band edge.

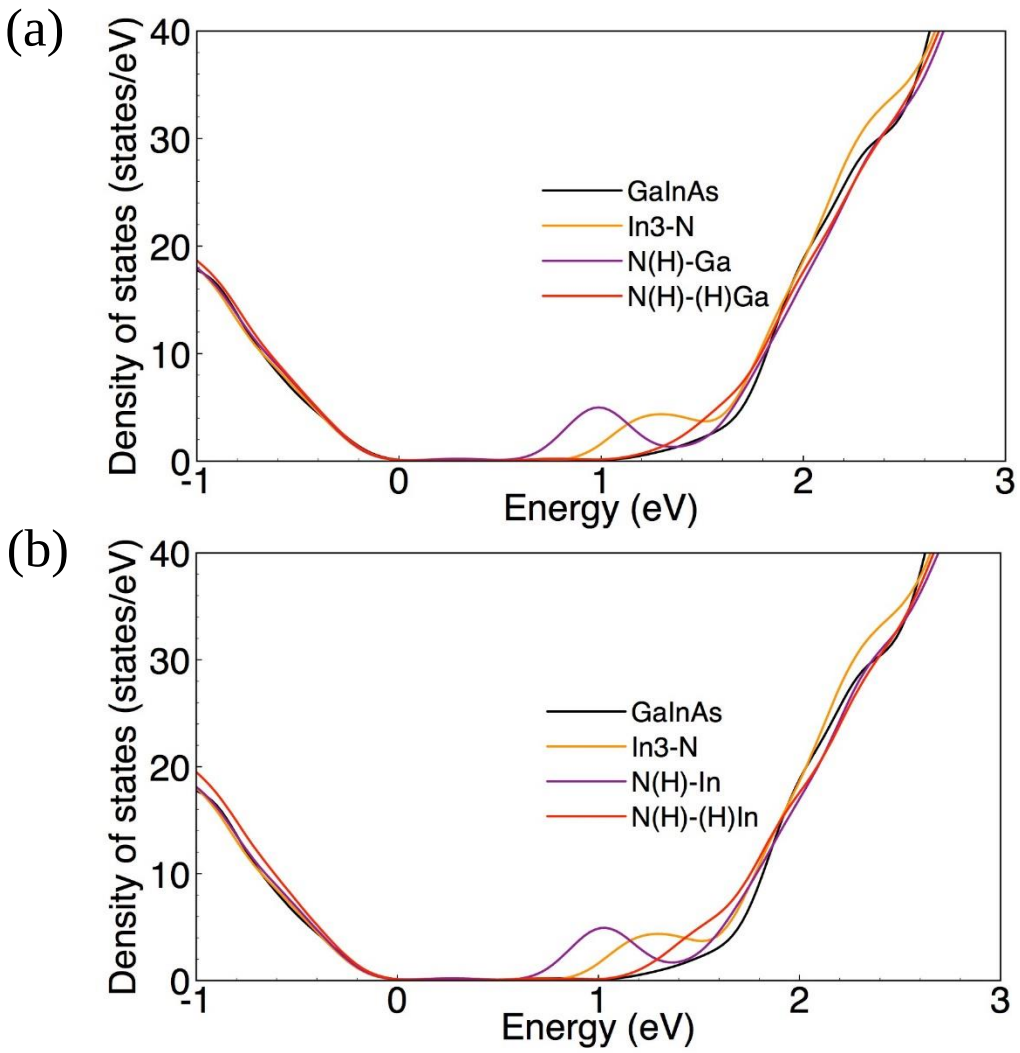

Figure A. 4 Comparison of the total density of states for the In_3-N structure (Figure 3. 2d) and the subsequent hydrogenation of (a) Ga and (b) In by breaking the Ga-N and In-N bonds. The DOS for original GaInAs (black curve) is plotted as reference. The zero-energy level is set at the valence band edge.

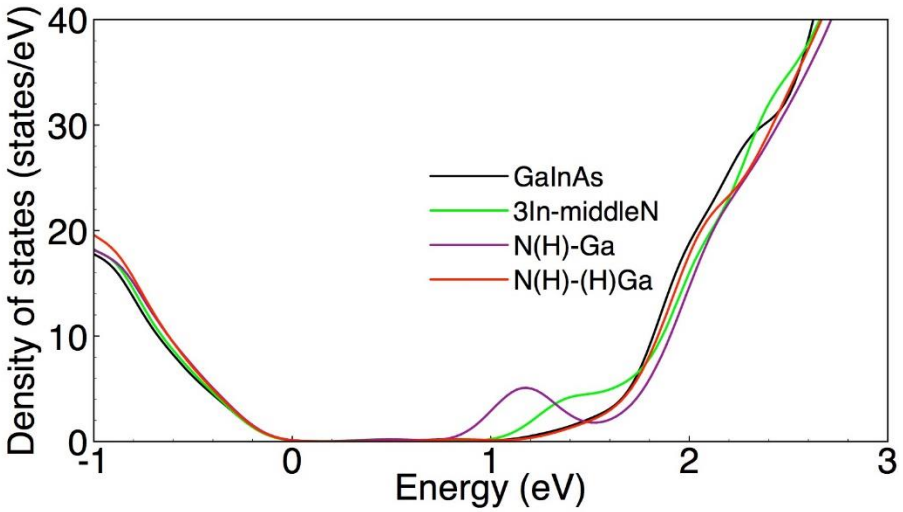

Figure A. 5 Comparison of the total density of states for the $In_3{\equiv}N$ structure (Figure 3. 2d) and the subsequent hydrogenation of Ga by breaking the Ga-N bond. The DOS for original GaInAs (black curve) is plotted as reference. The zero-energy level is set at the valence band edge.

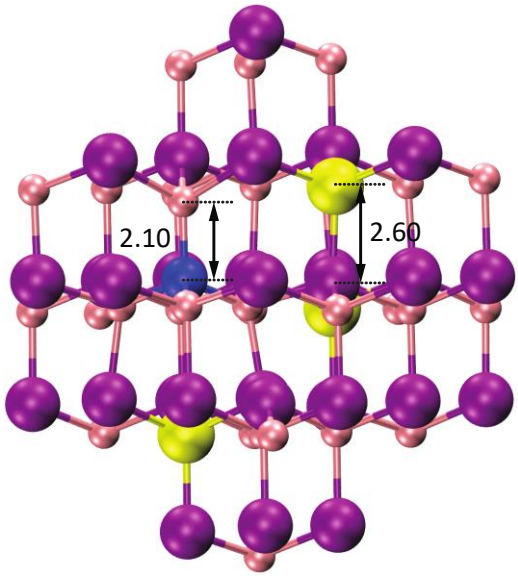

Figure A. 6 The structure of previously reported Ga-N bonding configuration (N with all four neighbors as Ga atoms).

Appendix B

SUPPLEMENTARY INFORMATION FOR CHAPTER 4

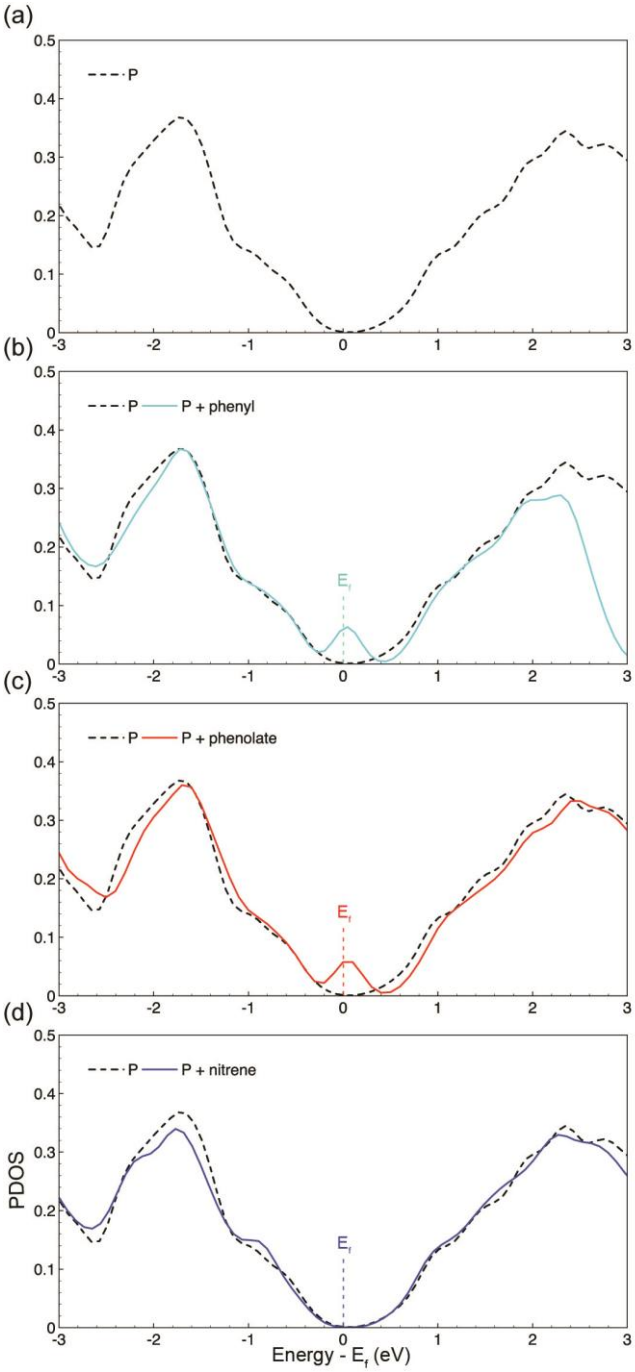

Figure B. 1 DFT-PBE calculated structures of functionalized black phosphorus with different functional groups (a) pristine black phosphorus, (b) phenyl, (c) phenolate, and

(d) nitrene. The projected density of states (PDOS) of the pristine black phosphorus (dashed curve) is shown in all panels. In the functionalized case, the PDOS onto black phosphorus (solid curves) is shown to compare with the pristine material (dashed curve).

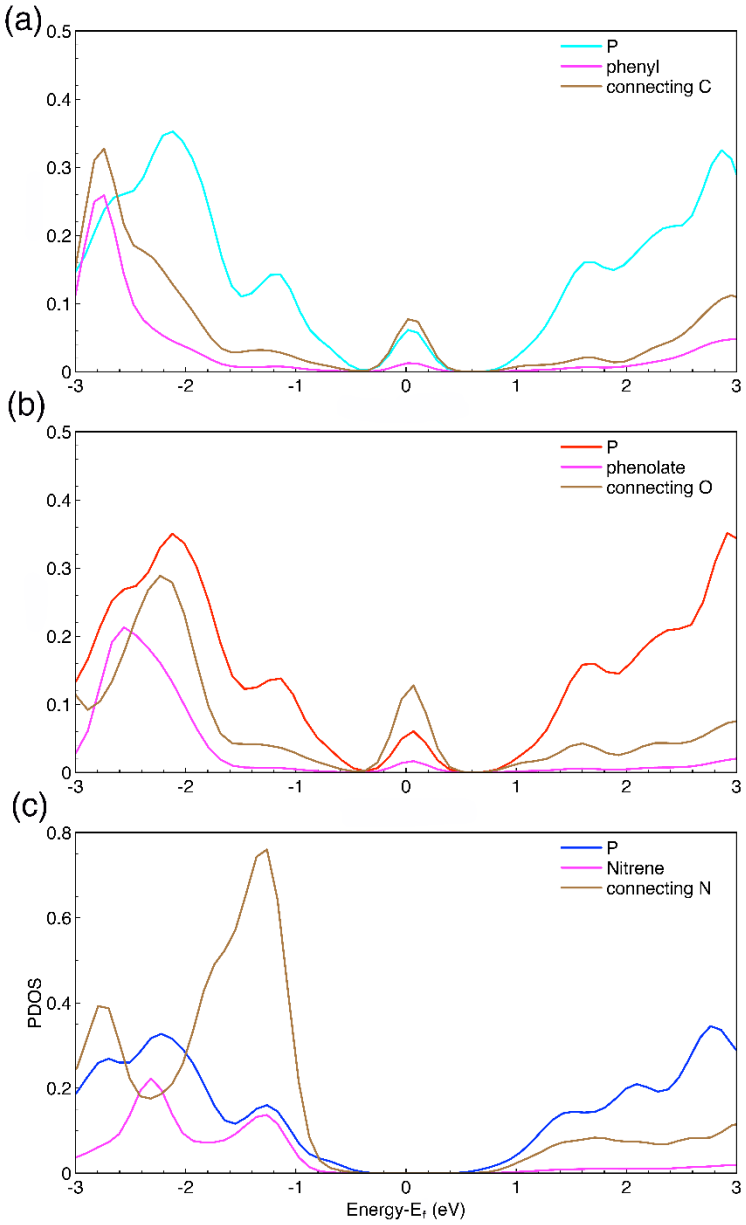

Figure B. 2 The projected density of states (DOS) of (a) phenyl (divided by 11), (b) phenolate (divided by 12) and (c) nitrene (divided by 12) and their corresponding connecting C, O and N atoms.

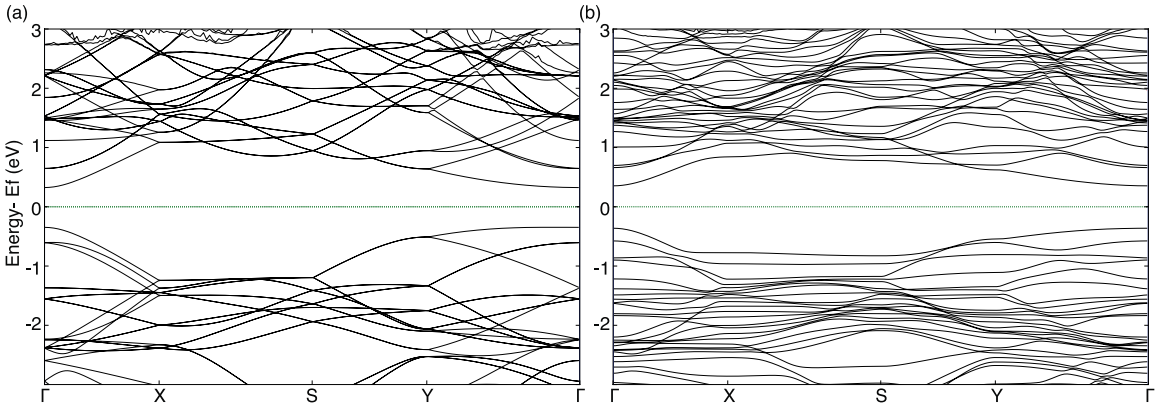

Figure B. 3 DFT-PBE calculated band structure of (a) pristine black phosphorus and (b) nitrene functionalized black phosphorus. Together with Figure B. 2, both band structure and DOS calculations suggest nitrene functionalization does not perturb the electronic property of black phosphorus.

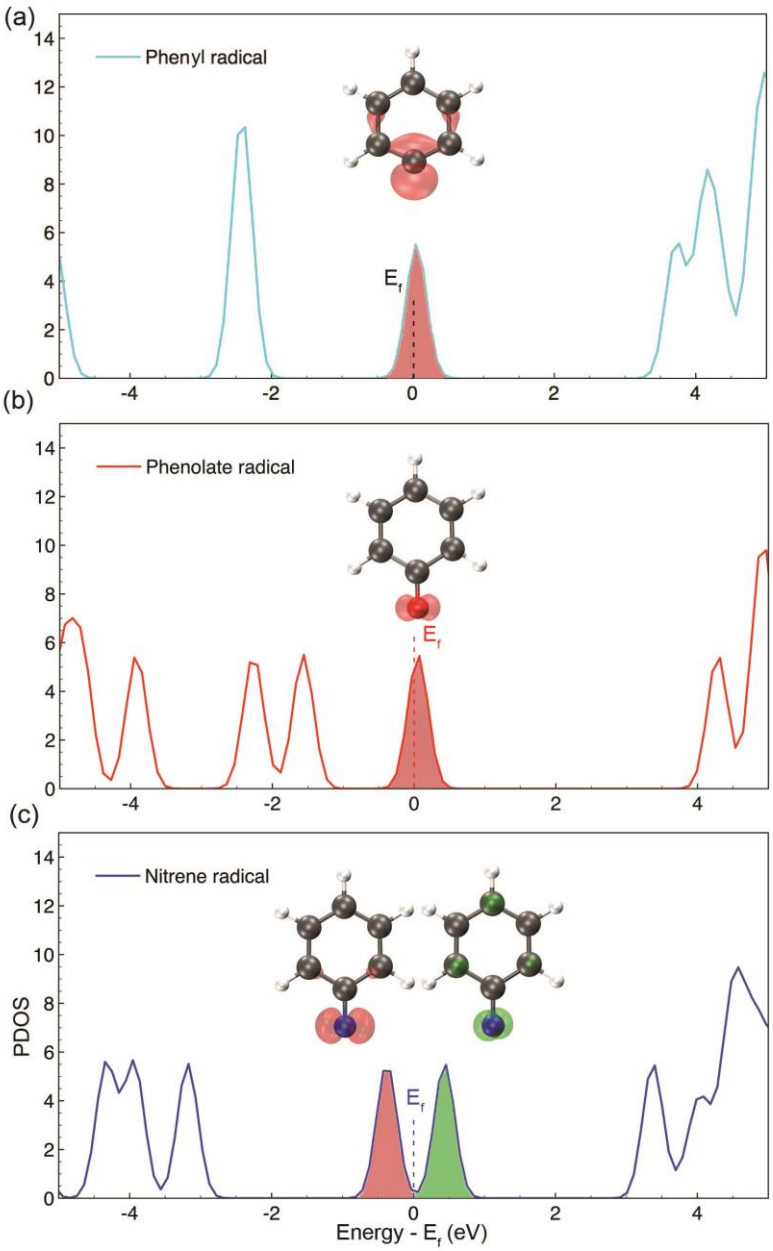

Figure B. 4 The density of states of (a) phenyl, (b) phenolate, and (c) nitrene radical. Black, white, red, blue balls denote C, H, O and N atoms, respectively. The shaded areas indicate the energy window used for charge integration.

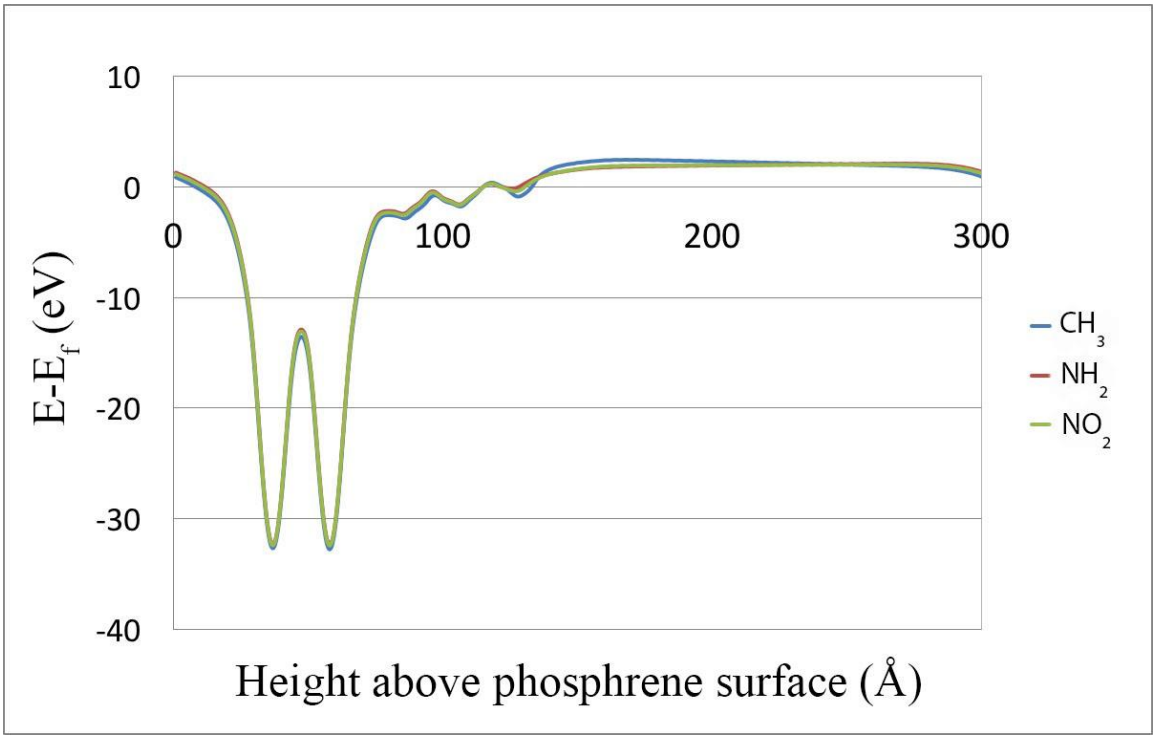

Figure B. 5 Electrostatic potentials of BP with different functional groups one one side using the DFT-PBE functional. Results of CH_3, NH_2 and NO_2-substituted are shown in blue, red, green solid lines, respectively.

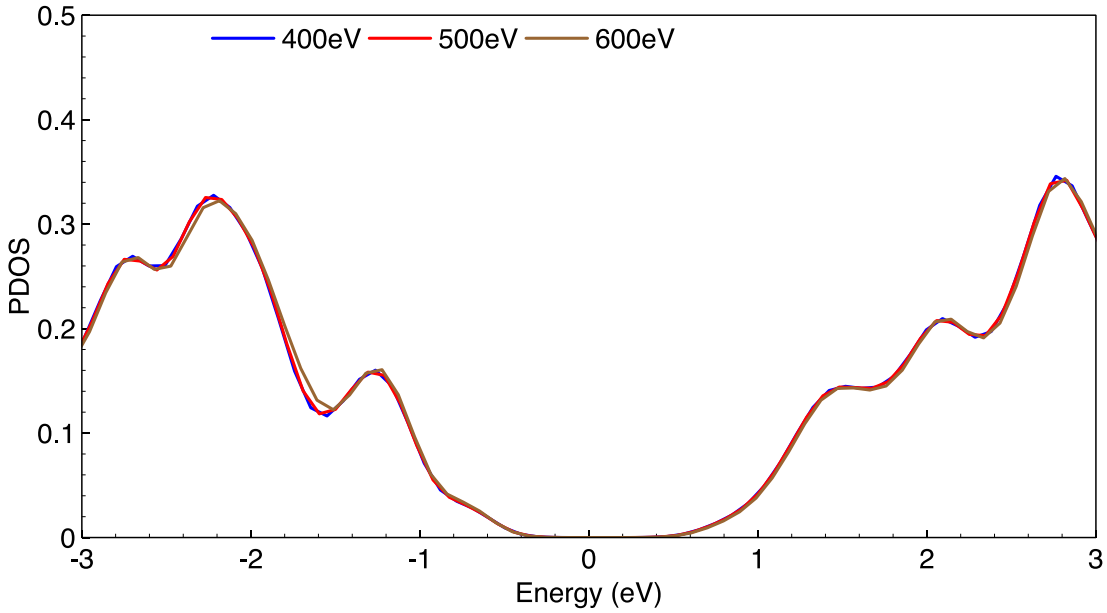

Figure B. 6 Electronic structure of BP functionalized with nitrene with cutoff energy at 400 eV (blue), 500 eV (red) and 600 eV (brown) and a smearing width of 0.02 eV.

Table B. 1 Calculated work function change at different coverage of the functional moieties. The numbers are reported in eV. Coverage (1/18 and 1/9 monolayer (ML)) is calculated based on number of functional groups divided by the number of surface P atoms.

	CH_3	NH_2	NO_2	Nitrene
WF (1/18 ML)	4.2	3.8	5.5	4.3
WF (1/9 ML)	4.1	3.7	6.2	4.3

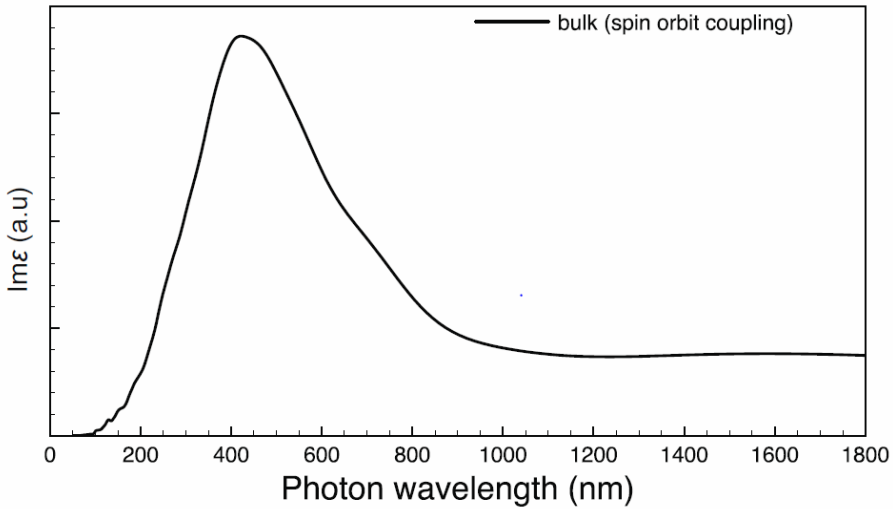

Figure B. 7 The imaginary part of the dielectric function for the franckeite bulk material with spin orbit coupling included.

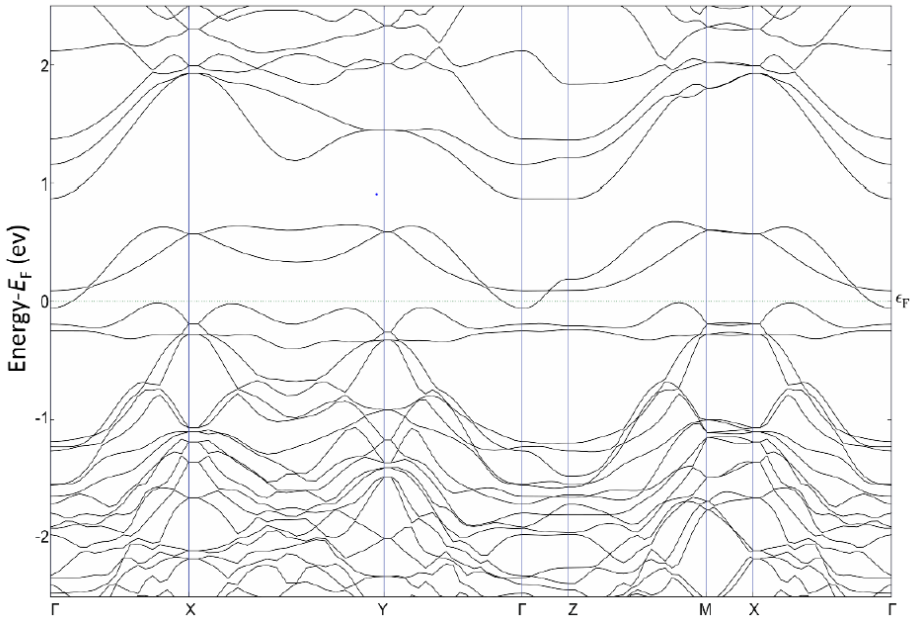

Figure B. 8 DFT calculated band structure of the bulk franckeite with spin-orbit coupling included.

Appendix C

SUPPLEMENTARY INFORMATION FOR CHAPTER 5

C.1 Catalyst preparation

The catalyst used in this study was synthesized by conventional incipient wetness impregnation. 0.25 wt.% Pd/α-Al_2O_3 was considered to potentially minimize the effect of mass transfer. Non-porous α-Al_2O_3 was applied to eliminate the internal mass transfer and the low metal loading was applied to ensure the measured rates are within kinetic regimes. The aqueous solution of catalyst precursor palladium (II) nitrate dihydrate (Sigma-Aldrich) was added drop by drop onto the catalyst support α-Al_2O_3 (Sigma-Aldrich) followed by drying at 70°C overnight. The sample was then calcined in air for 6 h at 300°C.

C.2 Catalyst characterization

Supported 0.25 wt.% Pd catalysts were characterized in a transmission electron microscope JEOL JEM-2100, operating with an accelerating voltage of 200 kV, equipped with LaB6 gun. The TEM sample was prepared by drop-casting a solution, which pre-reduced 0.25 wt.% Pd/α-Al_2O_3 was well dispersed in propanol by sonication, onto a holey carbon film mounted on a copper TEM grid. The Pd particles were analyzed using ImageJ to acquire particle size distribution and surface structure.

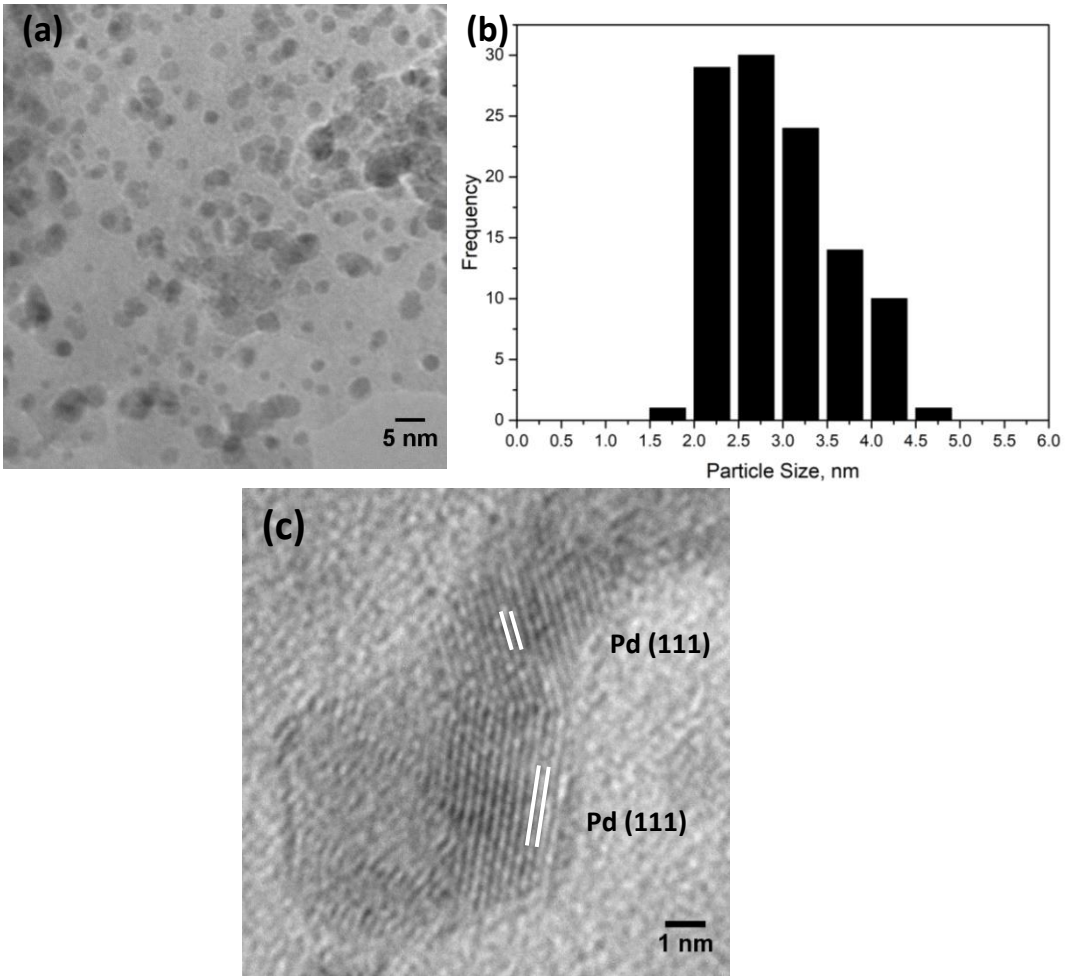

Figure C. 1 (a) TEM image of 0.25 wt.% Pd/α-Al_2O_3. (b) Histogram of Pd particles size distribution. (c) HRTEM image of Pd particles.

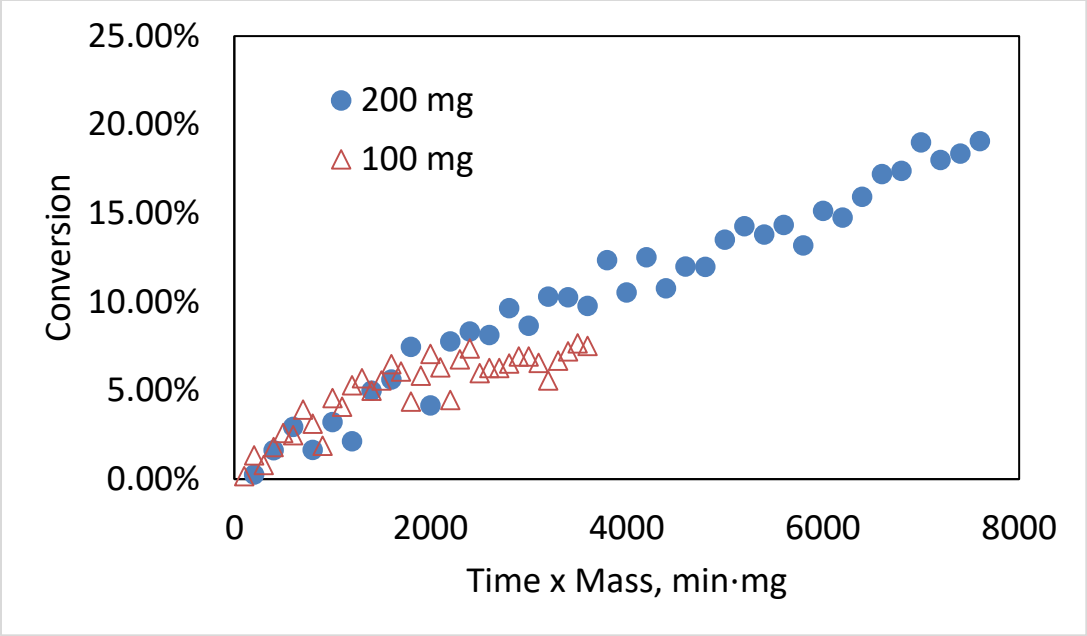

Figure C. 2 Deactivation study on 0.25 wt.% Pd/α-Al_2O_3. Reaction conditions: solvent heptane, H_2 pressure 560 psi, temperature 70°C, cyclohexene initial concentration 0.42M.

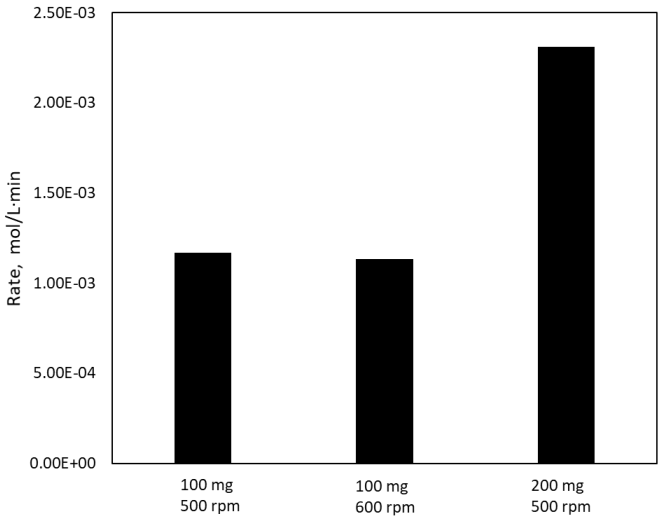

Figure C. 3 External mass transfer test. Reaction conditions: solvent heptane, H_2 pressure 560 psi, temperature 70°C, cyclohexene initial concentration 0.42M.

Table C. 1 Kinetic model fitting parameters.

	In heptane	In methylcyclohexane	In decalin
k_3, mol/L·min·g	0.022	0.022	0.022
K_{H_2}, psi^{-1}	0.018	0.018	0.018
K_E, L/mol	5.621	5.621	5.621
$K_{solv\ Hep}$, L/mol	0.000		
$K_{solv\ Ma}$, L/mol		0.491	
$K_{solv\ Dl}$, L/mol			4.370

Table C. 2 Kinetic and thermodynamic parameters from experimental fittings.

	ΔS, J/mol·K	ΔH, kJ/mol	$\alpha_{H_{ads}}$, kJ/mol
k_3	-2±1	81±2	
K'_E	-143±19	-75±14	22±6
K'_{H_2}	-108±12	-41±7	8±1

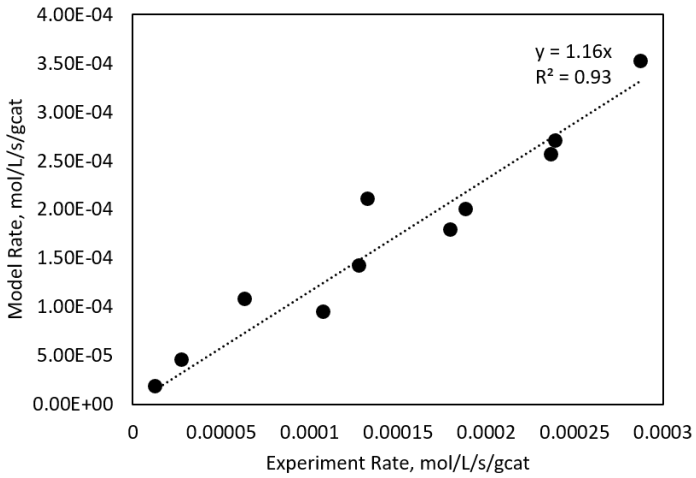

Figure C. 4 Comparison between rates from experimental measurement and model prediction using parameters from Table 6.

Appendix D

SUPPLEMENTARY INFORMATION FOR CHAPTER 6

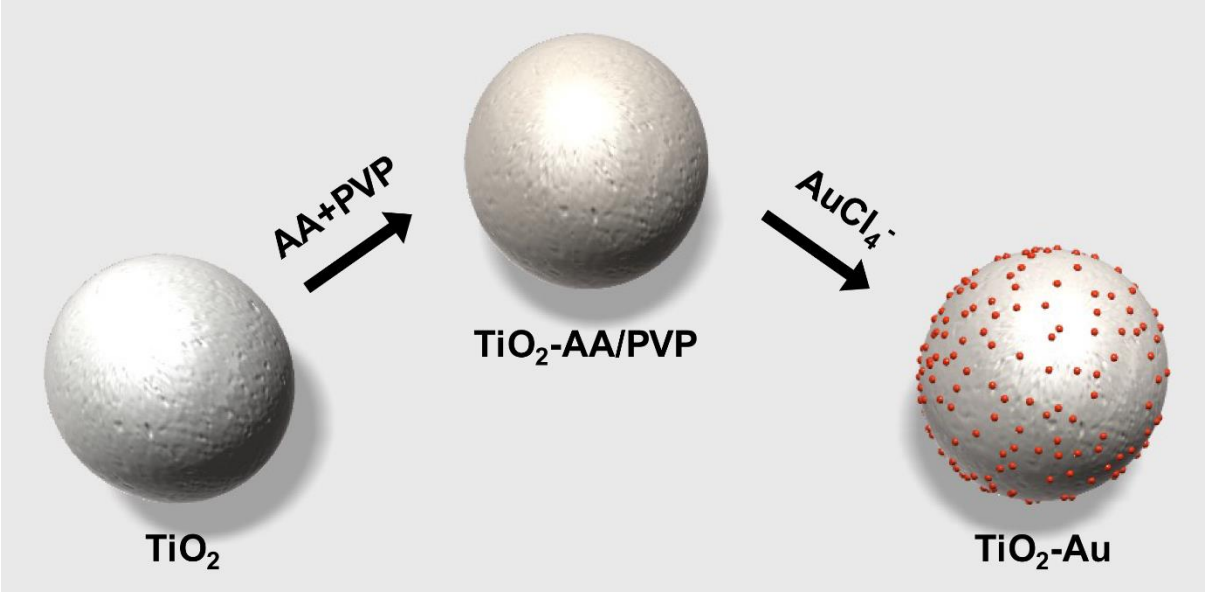

Figure D. 1 Schematic representation for the synthesis of TiO_2 colloidal spheres and TiO_2 colloidal spheres decorated with Au NPs (TiO_2-Au NPs). In this case, pre-formed TiO_2 colloidal spheres are used as seeds for the deposition of Au nanoparticles using $AuCl_4^-{}_{(aq)}$ as the Au precursor, ascorbic acid (AA) as reducing agent, polyvinylpyrrolidone (PVP) as stabilizer, and 90 °C as the reaction temperature.

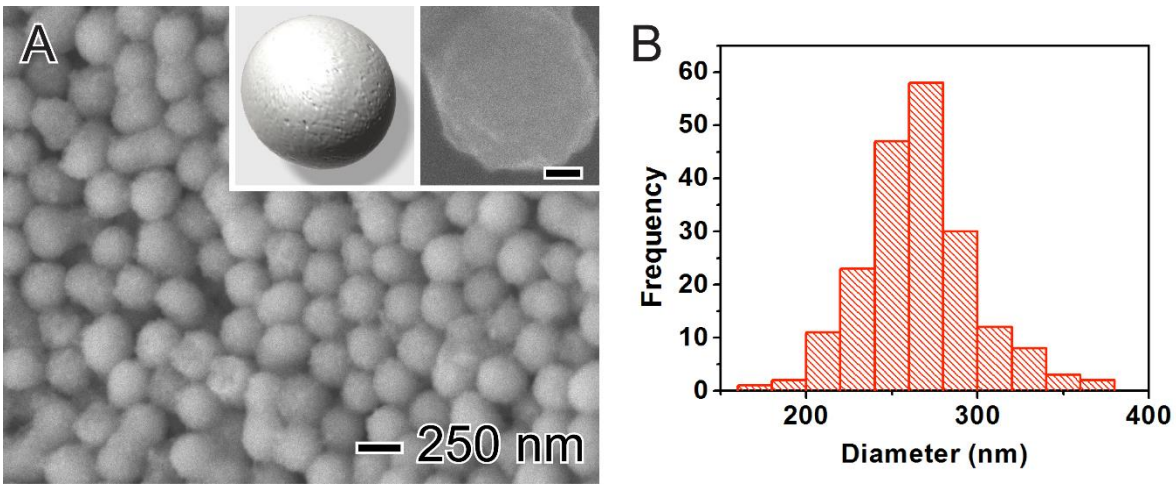

Figure D. 2 SEM image (A), and histogram of size distribution (B) for the TiO_2 colloidal spheres. They were 267.8 ± 37.8 nm in diameter, monodisperse, and displayed slightly rough surfaces. The scale bar in the inset corresponds to 50 nm.

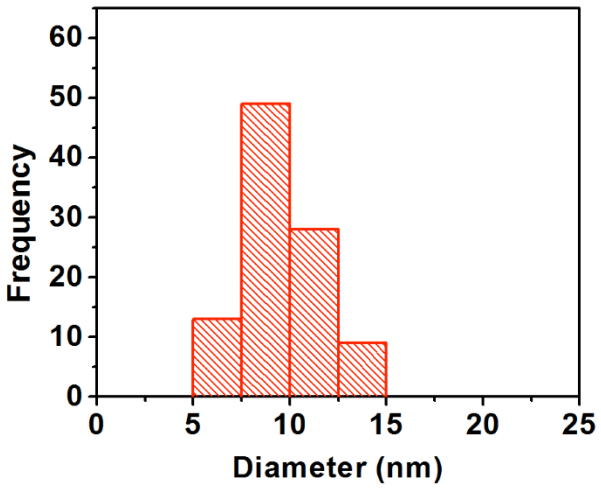

Figure D. 3 Histogram of size distribution for the Au NPs in the Au-TiO_2 materials. The average size corresponded to 9.7 ± 2.2 nm in diameter.

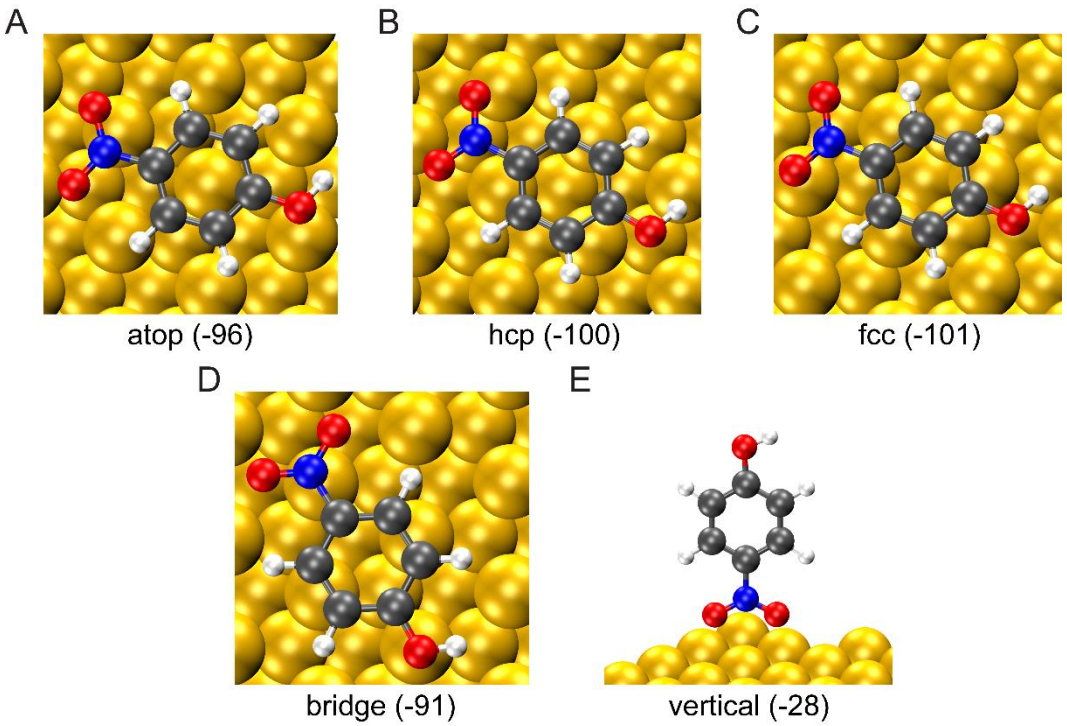

Figure D. 4 Structures of 4-NPh adsorbed on a Au (111) surface. The energies in brackets are adsorption energies in kJ/mol.

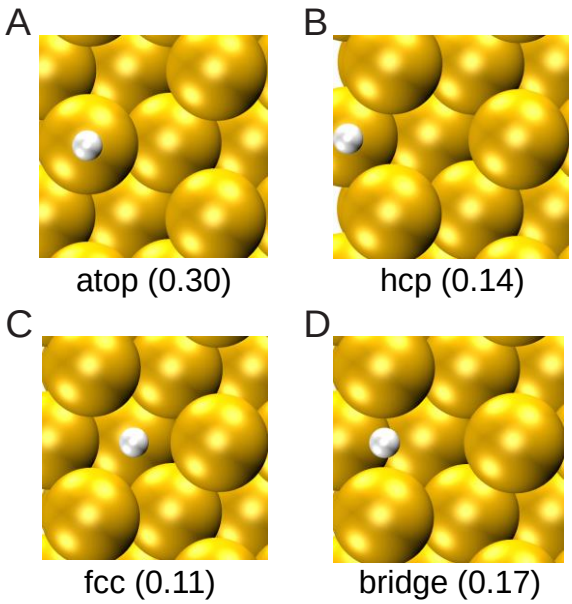

Figure D. 5 Structures of H adsorbed on a Au (111) surface. The energies in brackets are adsorption energies in kJ/mol.

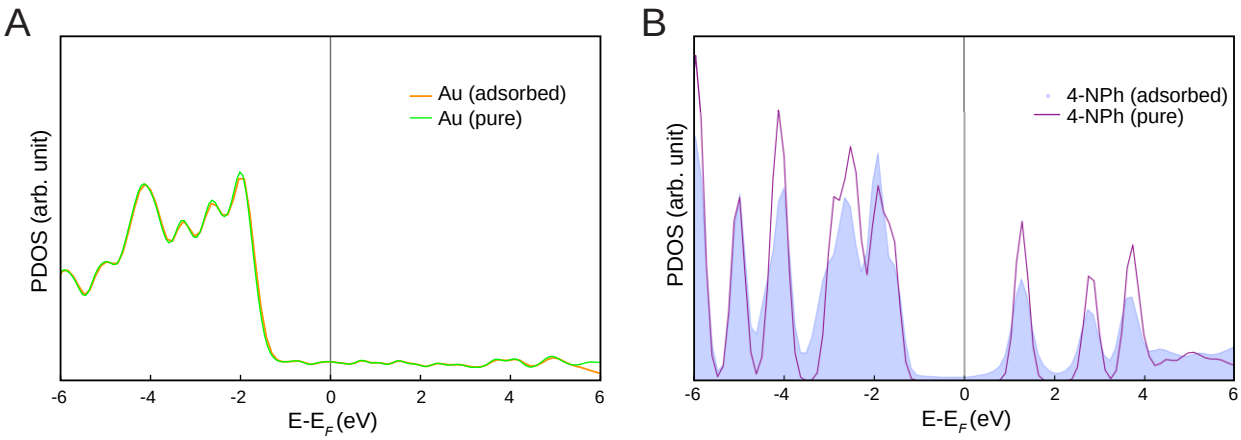

Figure D. 6 Electronic structures of 4-NPh adsorbed on a Au (111) surface, A. projected density of states (PDOS) of Au with 4-NPh adsorbed and DOS of prinstine Au for comparison, B. PDOS of adsorbed 4-NPh and DOS of gas phase 4-NPh for comparison.

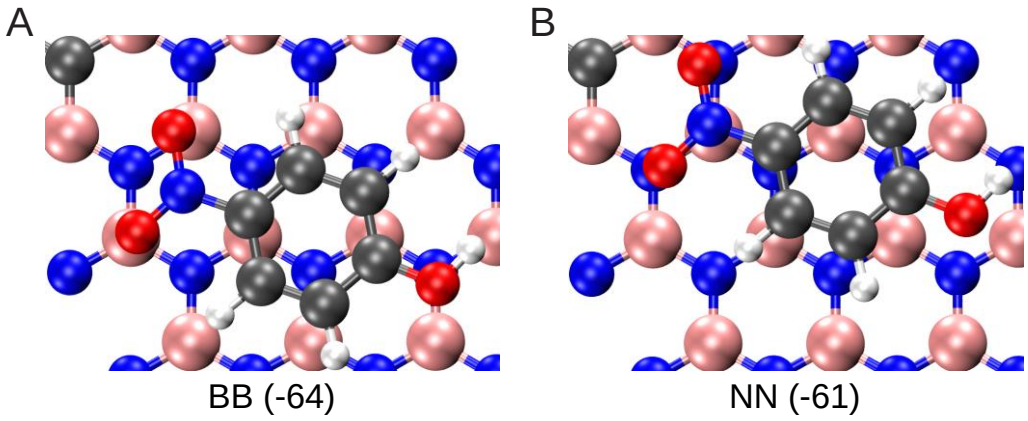

Figure D. 7 Structures of 4-NPh adsorbed on a CBN (001) surface.

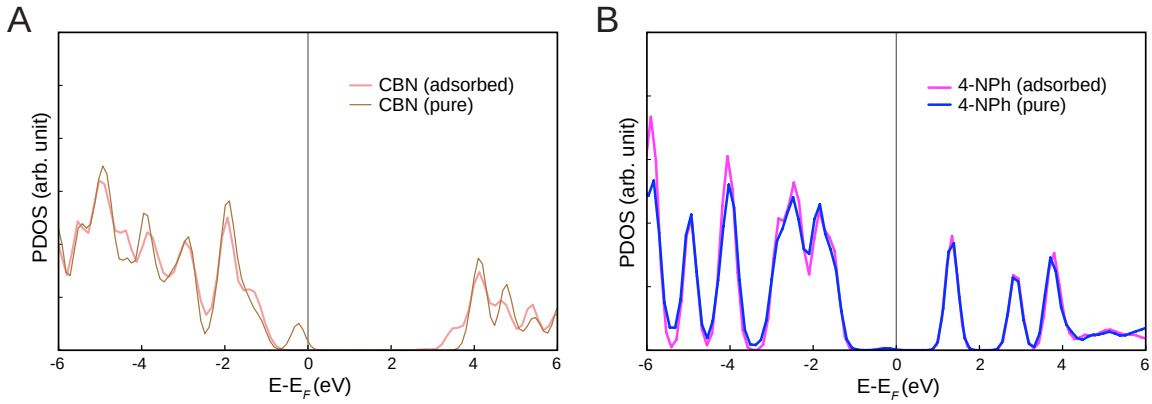

Figure D. 8 Electronic structures of 4-NPh adsorbed on a CBN (001) surface, A. projected density of states (PDOS) of CBN with 4-NPh adsorbed and DOS of prinstine CBN for comparison, B. PDOS of 4-NPh and DOS of gas phase 4-NPh for comparison.

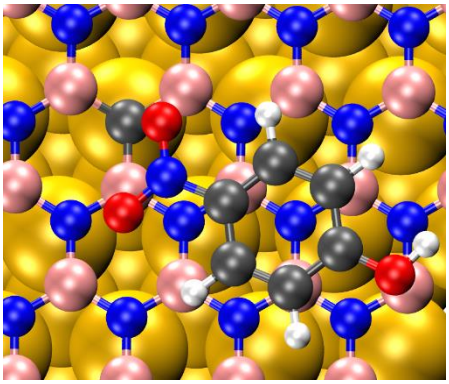

Figure D. 9 The optimized structure of 4-NPh adsorbed on a CBN (001)/Au (111) surface.

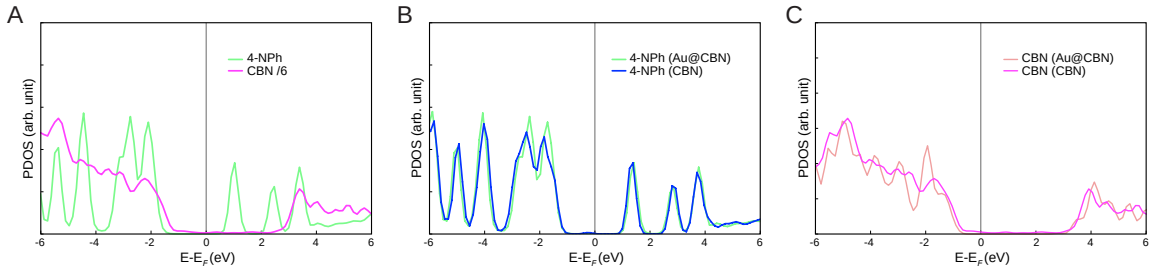

Figure D. 10 Electronic structures of 4-NPh adsorbed on CBN (001)/Au (111), A. projected density of states (PDOS) of CBN and 4-NPh, respectively. The DOS of CBN was reduced 6 times for better comparison. B. PDOS PF 4-NPh with and without Au slabs, C. PDOS of CBN with and without Au slabs.

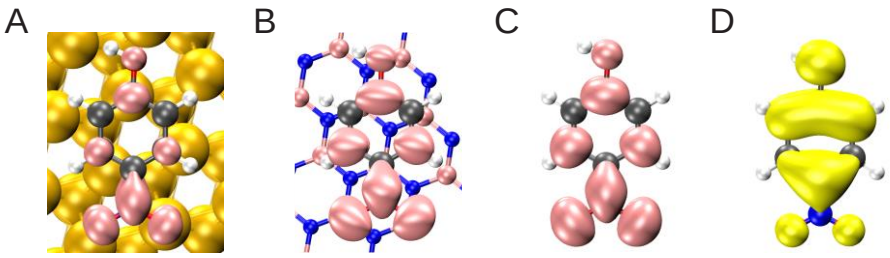

Figure D. 11 Calculated LUMO orbitals of adsorbed 4-NPh on A. Au (111), B. BN (001). Calculated C. LUMO and D. HOMO orbitals of 4-NPh molecule in the gas phase. Isosurface value of 0.01eV $Å^{-3}$ was applied.

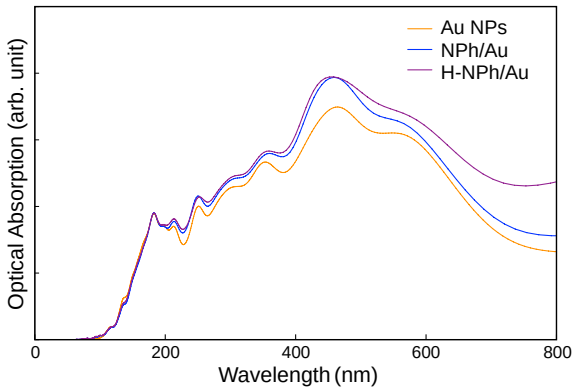

Figure D. 12 Imaginary part of the dielectric function for 4-NPh adsorbed on Au (111) (blue) and the co-adsorption of 4-NPh and H on Au (111) (purple) as compared with pristine Au (111) slab (yellow).

Table D. 1 Maximum rate analysis and the corresponding resistances of the first four elementary steps.

Elementary steps	Maximum rate	Resistance
1	1.0E+13	9.9E-14
2	1.0E+10	9.4E-11
3	2.7E-5	3.7E+4
4	1.9E-3	5.1E+2